

Extracting coronary blood flow from the intensity of contrast enhanced CCTA images

Citation for published version (APA):

Bakker, L. M. M. L. (2023). *Extracting coronary blood flow from the intensity of contrast enhanced CCTA images*. [Phd Thesis 1 (Research TU/e / Graduation TU/e), Biomedical Engineering]. Eindhoven University of Technology.

Document status and date:

Published: 14/04/2023

Document Version:

Publisher's PDF, also known as Version of Record (includes final page, issue and volume numbers)

Please check the document version of this publication:

- A submitted manuscript is the version of the article upon submission and before peer-review. There can be important differences between the submitted version and the official published version of record. People interested in the research are advised to contact the author for the final version of the publication, or visit the DOI to the publisher's website.
- The final author version and the galley proof are versions of the publication after peer review.
- The final published version features the final layout of the paper including the volume, issue and page numbers.

[Link to publication](#)

General rights

Copyright and moral rights for the publications made accessible in the public portal are retained by the authors and/or other copyright owners and it is a condition of accessing publications that users recognise and abide by the legal requirements associated with these rights.

- Users may download and print one copy of any publication from the public portal for the purpose of private study or research.
- You may not further distribute the material or use it for any profit-making activity or commercial gain
- You may freely distribute the URL identifying the publication in the public portal.

If the publication is distributed under the terms of Article 25fa of the Dutch Copyright Act, indicated by the "Taverne" license above, please follow below link for the End User Agreement:

www.tue.nl/taverne

Take down policy

If you believe that this document breaches copyright please contact us at:

openaccess@tue.nl

providing details and we will investigate your claim.

Extracting coronary blood flow from the intensity of contrast enhanced CCTA images

L.M.M.L. Bakker

April 2023

A catalogue record is available from the Eindhoven University of Technology Library

© Copyright 2023, Luc Bakker

All Rights Reserved. No part of this book may be reproduced, stored in a database or retrieval system, or published, in any form or in any way, electronically, mechanically, by print, photo print, microfilm or any other means without prior written permission of the author.

Cover design by: Gildeprint
Printed by: Gildeprint

The research described in this thesis was funded and supported by HeartFlow, Inc.

Extracting coronary blood flow from the intensity of contrast enhanced CCTA images

PROEFSCHRIFT

ter verkrijging van de graad van doctor aan de Technische Universiteit Eindhoven, op gezag van de rector magnificus prof.dr.ir. F.P.T. Baaijens, voor een commissie aangewezen door het College voor Promoties, in het openbaar te verdedigen op vrijdag 14 april 2023 om 16:00 uur

door

Luc Marcus Maria Ludovicus Bakker

geboren te Maastricht

Dit proefschrift is goedgekeurd door de promotoren en de samenstelling van de promotiecommissie is als volgt:

| | |
|-------------------------|--|
| voorzitter: | prof.dr. M. Merkk |
| Promotoren: | prof.dr.ir. F.N. van de Vosse prof.dr. C.A. Taylor |
| Copromotor: | dr.ir. M. Schaap. (HeartFlow) |
| Promotiecommissieleden: | prof.dr.ir. P.D. Anderson prof.dr. J.P.W. Pluim dr. I. Vignon-Clementel (INRIA, SIMBIOTX) prof.dr. N.H.J. Pijls |
| Adviseur: | dr.ir. A.A.F. van de Ven |

Het onderzoek of ontwerp dat in dit proefschrift wordt beschreven is uitgevoerd in overeenstemming met de TU/e Gedragscode Wetenschapsbeoefening.

Table of Contents

| | |
|--|-----------|
| Summary | 5 |
| 1 Introduction | 9 |
| 1.1 Coronary Artery Circulation | 9 |
| 1.2 Coronary artery disease | 11 |
| 1.3 Current clinical practice | 12 |
| 1.4 Contrast gradient found in CCTA | 13 |
| 1.5 Aim and thesis outline | 15 |
| 2 Spectral element solver | 19 |
| 2.1 Introduction | 19 |
| 2.2 Pseudo spectral approximation | 20 |
| 2.2.1 Legendre Polynomials | 21 |
| 2.2.2 Legendre-Gauss quadrature | 21 |
| 2.2.3 Lagrange interpolation polynomials | 22 |
| 2.2.4 Isoparametric Mapping | 24 |
| 2.2.5 Higher dimensions | 24 |
| 2.3 Spectral element formulation | 25 |
| 2.3.1 Advection diffusion equation | 25 |
| 2.3.2 Axi-symmetric advection diffusion | 26 |
| 2.3.3 Navier-Stokes equation | 27 |
| 2.3.4 Axi-symmetric Navier-Stokes equation | 28 |
| 2.3.5 Neumann Boundary condition | 29 |
| 2.4 Solver | 30 |

| | | |
|----------|---|-----------|
| 2.5 | Meshes | 30 |
| 2.5.1 | 2D axi-symmetric mesh | 30 |
| 2.5.2 | Tubular mesh | 31 |
| 2.5.3 | Arterial tree mesh | 32 |
| 2.6 | Software verification | 35 |
| 2.7 | SEM vs FEM | 35 |
| 2.8 | Conclusion | 37 |
| 3 | Image-based blood flow estimation using a semi-analytical solution to the advection diffusion equation in cylindrical domains | 41 |
| 3.1 | Introduction | 42 |
| 3.2 | Methods | 44 |
| 3.2.1 | Problem formulation | 44 |
| 3.2.2 | Galerkin method | 45 |
| 3.2.3 | Laplace transform | 47 |
| 3.2.4 | ADFE method | 48 |
| 3.2.5 | Spectral element solver | 48 |
| 3.3 | Results | 49 |
| 3.3.1 | Verification of the semi-analytical solution | 49 |
| 3.3.2 | ADFE results | 50 |
| 3.4 | Discussion | 53 |
| 3.5 | Conclusion | 54 |
| 4 | In-silico validation of the advection diffusion flow estimation method using computational patient specific coronary tree phantoms | 59 |
| 4.1 | Introduction | 60 |
| 4.2 | Methods | 63 |
| 4.2.1 | Patient Collective | 65 |
| 4.2.2 | AIF | 65 |
| 4.2.3 | Patient specific software phantoms | 66 |
| 4.2.4 | Spectral element solver | 66 |
| 4.2.5 | TAFE | 67 |
| 4.2.6 | ADFE for coronary trees | 68 |
| 4.3 | Results | 69 |
| 4.3.1 | AIF example | 70 |
| 4.3.2 | ADFE vs TAFE | 70 |
| 4.3.3 | Specific cases | 71 |
| 4.4 | Discussion | 76 |
| 4.5 | Conclusion | 78 |

| | | |
|----------|---|------------|
| 5 | Verification before clinical validation ADFE | 83 |
| 5.1 | Introduction | 84 |
| 5.2 | Methods | 85 |
| 5.2.1 | Virtual computed tomography | 85 |
| 5.2.2 | Computed tomography correction function | 86 |
| 5.3 | Results | 88 |
| 5.3.1 | CT correction straight vessel | 88 |
| 5.3.2 | CT correction vessel tree | 89 |
| 5.4 | Discussion | 92 |
| 5.5 | Conclusion | 93 |
| 6 | General Discussion | 95 |
| 6.1 | Current overview | 95 |
| 6.2 | Future work | 98 |
| | Samenvatting | 103 |
| | Curriculum Vitae | 106 |

Summary

Coronary computed tomography angiography (CCTA) is conducted by injecting an intravenous iodine based contrast material into the bloodstream to highlight the lumen of the coronary arteries. This allows anatomical assessment of the geometrical characteristics of obstructive atherosclerotic plaques, i.e. stenoses. This CCTA can be used to identify the severity of a stenosis and it helps to achieve decisions on clinical intervention. However, CCTA does not provide any information about hemodynamic characteristics such as flow or pressure drops across the stenosis that are better variables to base decisions on.

Over the past years, fractional flow reserve (FFR) has been used in clinical decision making when treating coronary artery disease. FFR is defined as the ratio between the pressure distal to the stenosis and the reference aortic pressure under conditions of maximal flow induced by a vasodilator. Measuring FFR requires fluoroscopic guided invasive catheterization and the insertion of a pressure wire to a location in the vessel distal to the lesion. However, the same metric can be obtained by using computational fluid dynamics (CFD) models. These non-invasive CFD models are created by segmenting a computational mesh of the coronary circulation from the CCTA together with boundary conditions based on scaling laws utilizing patient specific geometry. Although these CFD models have proven to provide a good diagnostic value an improvement could be achieved by inferring the hemodynamic and geometrical information embedded in the contrast intensity found in the CCTA image.

During CCTA at the entrance of the coronary circulation (aorta), a rise and decay of the intravenous contrast concentration over time can be indi-

rectly measured via dynamic image acquisition. This rise and fall describes the arterial input function (AIF). The contrast material is transported by the coronary blood flow (CBF) through the coronaries. The combination of AIF, CBF and coronary geometry results in a contrast agent distribution visible on the CCTA image. The information of this distribution can be described by the advection diffusion equation. By solving this equation a direct link between all the parameters is obtained. This enables to solve the inverse problem of extracting CBF based on the measured contrast intensity. Existing methods show mixed success caused by oversimplifying the advection diffusion equation and because the intensity measured on the CCTA image is not always well correlated with the real concentration of the contrast material. In this thesis, we propose an improved method for extracting CBF called advection diffusion flow estimation (ADFE) by improving the solution of the advection diffusion equation.

However, to verify this new method, we need data that does not contain imaging effects. Clinical CCTA data sets are not suitable for verification as the error caused by the solution used and errors induced by imaging effects are impossible to separate. In order to circumvent this, we created software phantom data consisting of geometries on which the transport of contrast was simulated. The computations and creation of these simulations was done by our spectral element method (SEM) solver described in Chapter 2. SEM uses higher order elements combined with optimal integration which enables the computation of situations without the use of stabilization methods of the traditional finite element method (FEM). In the result section we show the higher convergence rate of SEM compared to FEM and discuss the ability to compute difficult to simulate convection dominated situations. All mentioned software phantoms in this thesis were computed by this SEM solver.

In Chapter 3, we formulated and verified the improved version of the advection diffusion equation and we derived a semi-analytical solution of the 2D axi-symmetric advection diffusion equation. The verification was done on 2D axi-symmetric software phantoms by checking the agreement between our semi-analytical solution and simulated concentration. This solution forms the base for our new ADFE method. ADFE is also verified on the 2D axi-symmetric software phantom data set by comparing computed flow with inferred flow. Finally we compared ADFE against the current golden standard called transluminal attenuation flow encoding (TAFE) and show a significant improvement in predicted flow from ADFE compared to TAFE.

In Chapter 4, we extended ADFE to be able to compute CBF from patient specific coronary trees. Compared to simple axi-symmetric geometries, a sec-

ond optimization step in ADFE was necessary to ensure a robust and accurate computation of CBF. The verification was again performed on software phantoms extracted from clinical CCTA data sets and the results show excellent agreement between computed and inferred flow. In order to make sure that the improvement of ADFE compared to TAFE also holds for complex tree geometries, we again compared the two methods and showed that it is still evident.

Finally, in Chapter 5, a computed tomography (CT) correction function was derived to add the effects of blur to the semi-analytical solution embedded in ADFE. This enables ADFE to compute flow from blurred contrast intensity found in the CCTA image. In order to verify ADFE with this CT correction function, a simple virtual CT method was used to add blur and noise to the contrast data from the software phantoms of Chapter 4. Although the accuracy of ADFE on this virtual CT data set was reduced compared to the original data set used in Chapter 4, it is still a significant improvement compared to TAFE and usable for clinical applications. Overall ADFE shows great potential to become an accurate method to estimate CBF from CCTA images.

1.1 Coronary Artery Circulation

The main task of the cardiovascular system is to supply oxygen and nutrients to each organ system. This is achieved by the contraction of the myocardium (heart muscle), which causes blood flow through the arteries. These contractions are periodic and result in a pulsatile pressure and flow pattern, which is gradually damped due to the compliance and viscous loss of the arterial system. Consequently, most organs receive a more or less continuous supply of oxygen and nutrient enriched blood. In order to contract, the heart itself also needs a continuous supply of oxygen. There are two main arteries that branch alongside the myocardium to supply it with blood - the Left Coronary Artery (LCA) and Right Coronary Artery (RCA) (Figure 1.1). Furthermore, the LCA is split into two main arteries - the Left Anterior Descending coronary artery (LAD) and Left Circumflex coronary artery (LCX). Due to the relative short distance of the coronary arteries to the aortic outflow of the heart and the influence of the myocardial contraction, coronary blood flow (CBF) is highly pulsatile. The time averaged CBF therefore determines the final supply of oxygen to the myocardium and thus the ability of the heart to contract sufficiently.

Generally, the total amount of time averaged CBF depends on the demand of the myocardium. A scaling law governs the relationship between the total volume of the myocardium and total CBF (Choy & Kassab, 2008). However, the amount of CBF through each segment of the coronary arterial tree differs

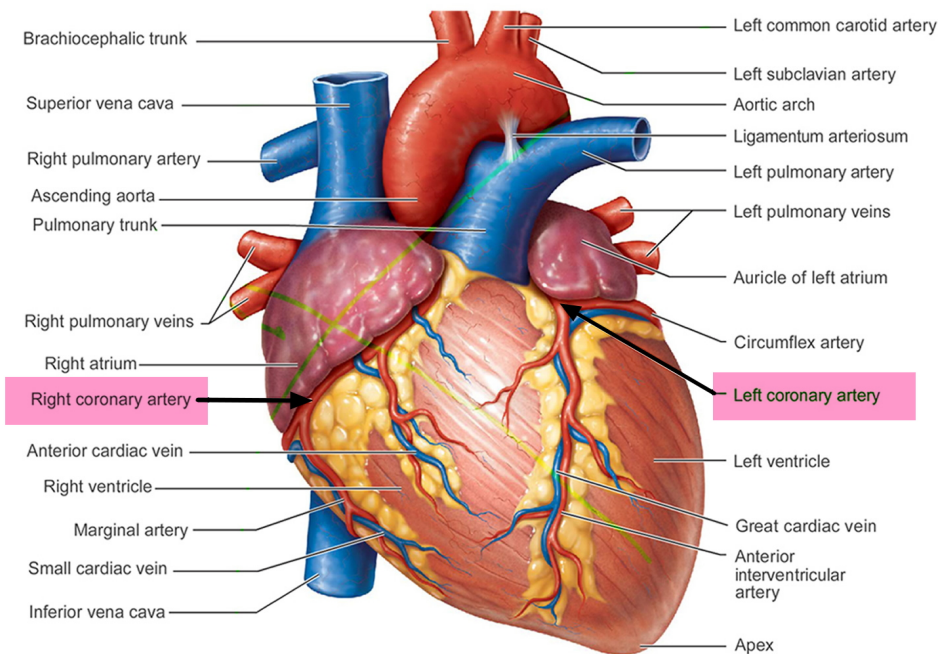


Figure 1.1: *Coronary circulation including the arteries and veins surrounding the heart. Figure adopted from <http://healthjade.com/what-is-heart-disease>.*

per individual due to varying demands for blood from different parts of the myocardium as well as differences in coronary anatomies. The right ventricle myocardium is responsible for the pulmonary circulation (lungs) and the left ventricle myocardium is responsible for the systemic circulation (the rest of the body). This means that the left ventricle needs to produce a higher blood pressure than the right ventricle because of the larger resistance in the part of the circulatory system it supports and consequently, needs more oxygen to support its function. Genetic differences between people can cause drastic differences in anatomy; however, one general classification in coronary anatomy is right vs. left dominant circulation. In right dominant circulations, the RCA encircles the right ventricle and even supplies parts of the left ventricle, which reduces the size and myocardial territory of the LCX. In left dominant circulations, it is the other way around. Though these are distinct classifications, each person is different in how right or left dominant they are. All of these differences eventually cause patient-level differences prescribing the CBF in the coronary arteries.

The periodic contraction of the myocardium causes time-dependent or pulsatile blood flow. During systole the myocardium contracts and the intramyocardial pressure increases squeezing the microcirculation inside the myocardium. This temporarily reduces the amount of CBF. During diastole the myocardium relaxes and the intramyocardial pressure decreases and thus, the amount of CBF increases. The amount of reduction depends on the intramyocardial pressure, which itself is a function of the blood pressure generated inside the ventricles. On the time-dependent scale, this constitutes yet another contributor to differences in arterial and patient level coronary blood flow.

1.2 Coronary artery disease

Coronary artery disease (CAD) characterized by a narrowing of the coronary arteries can impair this demand of CBF. The process of CAD causing the abnormal narrowing of arteries, i.e. stenosis, is known as atherosclerosis and occurs when fatty substances get deposited inside the arterial wall (Stary et al., 1995). This sudden change of diameter causes an additional pressure loss which would lower the CBF if left unaddressed. However, by relaxing the smooth muscles inside the wall of especially the arterioles and capillaries in the myocardial micro-circulation, less pressure difference is needed to move blood through these downstream regions or in other words the resistance of this region is decreased. This mechanism is typically used to regulate the

changing myocardial oxygen demands for instance during exercising. In controllable situations, the additional pressure loss by the stenosis will not exceed the positive pressure difference gained by lowering the resistance which increases the CBF back to a healthy level. When the coronary arterioles and capillaries are fully dilated, the maximal hyperemic CBF is reached. The stenosis can cause the demanded CBF to exceed the hyperemic CBF causing a deficit of oxygen inside the myocardium. The lack of oxygen to support the heart muscle (ischemia) is usually presented as chest pain or discomfort; however, when not treated properly can lead to myocardial infarction (MI/heart attack) or death (Stary et al., 1995). In the United States, CAD is the most common type of heart disease, and about 20.1 million adults age 20 and older have CAD (about 7.2%). This high number of patients contributes in 2 out of 10 deaths happen from CAD in adults less than 65 years old (Tsao et al., 2022). This makes CAD one of the leading causes of death in the Western world, despite years of research focus, and billions of dollars research and development investments.

1.3 Current clinical practice

In order to diagnose CAD, coronary computed tomography angiography (CCTA) is an important non-invasive imaging modality that has been adopted as the first choice in many clinical guidelines when a patient shows possible symptoms of CAD. This imaging is conducted by measuring 3D x-rays attenuation of a patient's heart while injecting an intravenous Iodine based contrast agent into a patient's circulatory system. This highlights the arterial lumen of the coronary arteries, with the correct timing of the contrast agent. This CCTA image is then used to visually identify the severity of the CAD and aids in making decisions on patient treatment, and if necessary, coronary intervention. However, this assessment does not provide any information about the functional severity of the stenosis, i.e. the hemodynamics (blood flow or pressure drops) within the coronary arteries, which have been shown as important indicators when assessing the severity of CAD (Pijls et al., 2010; Tonino et al., 2009).

An invasive metric that has become the golden standard for diagnosing the severity of CAD is fractional flow reserve (FFR), defined as the ratio between pressure distal to a stenosis and aortic pressure (Pijls & Sels, 2012). FFR has been shown to improve patient outcomes when used to decide whether or not percutaneous coronary intervention is performed (Pijls et al., 2010). Obtaining FFR requires a fluoroscopic guided invasive catheterization procedure where

a wire is inserted into either the brachial or femoral artery of a patient and guided all the way up to the patient's coronary arteries where the lesion is present to measure the pressure drop across the lesion.

Recently, computational advances have provided the ability to compute a non-invasive equivalent to FFR called FFR_{CT} (Taylor et al., 2013). In order to calculate FFR_{CT} , the coronary geometry is extracted from the CCTA image and computational fluid dynamics (CFD) is used to approximate solutions of the governing equations of fluid flow. The accuracy of this approximation depends not only on the spatial resolution and correct segmentation of the coronary arterial lumen but also on the boundary conditions that control the CBF through each vessel. While geometrical parameters such as coronary artery diameter and myocardial volume can be readily extracted from the CCTA image, boundary conditions are difficult to estimate due to complex, patient-specific physiological conditions. FFR_{CT} results, calculated using boundary conditions derived from anatomical information have demonstrated high diagnostic accuracy when compared to FFR (Taylor et al., 2013). However, these methods overlook the functional information that is implicitly embedded in the CCTA image itself. Recently, there has been growing interest in inferring coronary flows or assessing stenosis severity by analyzing the contrast intensity gradients along the coronary vessels (Bae et al., 2018; Choi et al., 2012; Fujimoto et al., 2018; Lardo et al., 2015; Park et al., 2016; Steigner et al., 2015; Stuijzand et al., 2014). These techniques have the potential to further improve the estimation of boundary conditions and the diagnostic accuracy of FFR_{CT} .

1.4 Contrast gradient found in CCTA

Within the aorta, a rise and decay of the concentration of intravenously-injected contrast can be indirectly measured via temporal image acquisition using CCTA. This rise and decay describes the arterial input function (AIF), being the concentration of the contrast at the level of the aorta over time. The contrast material is transported by the coronary blood flow (CBF) into the coronary vessels. When the CTA image is acquired before the peak of the AIF, a linear function can be fitted through the intensities along the paths of the arteries. The slope of this linear function is called the Transluminal Attenuation Gradient (TAG) and in the same artery it is higher at lower flow and lower at higher flow (Choi et al., 2012; Park et al., 2016; Steigner et al., 2015). Computation of TAG is facilitated by the advent of 256 and 320 row detector scanners such as the Toshiba Aquilion One, GE Revolution or Arineta Cardiographe that can image the full heart in a single cardiac cycle

ensuring that the error due to sampling over multiple cardiac cycles can be avoided. In recent work, TAG was computed in healthy subjects and patients with CAD (Bae et al., 2018; Choi et al., 2012; Fujimoto et al., 2018; Park et al., 2016; Steigner et al., 2015; Stuijzand et al., 2014) and was found to be not significantly different across cardiac phases in the LAD. However, these differences were significant in the LCX and RCA. Moreover, TAG was also found to be lower in the RCA -6.5 ± 4.1 HU/cm than in the LAD -13.7 ± 8.0 HU/cm or LCX -12.5 ± 7.8 HU/cm (Steigner et al., 2015). Park et al. used a phantom study to show that TAG may be affected by the secondary effect of vessel tapering which is lower in the RCA compared to the LAD and LCX (Park et al., 2016).

The relationship between TAG and CBF was derived by Eslami et al. by solving the 1D advection diffusion equation. They concluded that the effects of diffusion and Taylor dispersion could be neglected (Eslami et al., 2015). Eslami et al. also assumed that the vessel does not change much in cross-sectional area over the path length and that the AIF can be approximated by means of an analytical function. Using these assumptions, they derived a correlation between TAG and CBF called transluminal attenuation flow encoding (TAFE) and found a reasonably good correlation between TAFE and CBF measurements using micro spheres on 9 canine hearts (Lardo et al., 2015). TAFE's accuracy on clinical data was validated by Bae et al. (Bae et al., 2018), who also introduced the TAFE correlation coefficient k to compensate for the tendency of TAFE to underestimate flow, caused by imaging dependent effects on the contrast signal and simplification of the velocity field embedded inside TAFE (Eslami et al., 2022). In order to validate TAFE, with the correction coefficient k , Bae et al. used CCTA data with a range of lesion severities together with a perfusion data set for estimating k . For the patient group having no occlusions the correlation between TAFE and the measured flow is as high as in the perfusion study. However, the slope in the correlations in the diseased patient groups decreased with increasing stenosis severity (1.018 for 0 % diameter stenosis, 0.832 for 1 - 49 % diameter stenosis, 0.819 for 50 - 79 % diameter stenosis and 0.541 for 70 - 99 % diameter stenosis) (Bae et al., 2018).

The predictions of lower CBF in the rest state (TAG is computed in this state) from the TAG and TAFE studies contradict the measurements done by Gould et al. (Gould & Lipscomb, 1974), who measured flow and pressure in canine coronary arteries in both rest and hyperemic states. During rest no reduction in CBF was observed until the reduction of arterial diameter was greater than 85%. The required CBF at rest can be attained because myocar-

dial perfusion is regulated by dilating the coronary arterioles thereby lowering the microvascular resistance. We hypothesize that the higher negative TAG extracted from stenosed arteries can only be explained by a lower CBF when the reduction of arterial diameter is severe.

There are multiple possible explanations for the difference in TAG between healthy and stenosed arteries. Our first hypothesis is that the intensity measured on the CCTA image is not always well correlated with the real concentration of the contrast material. This may be due to low-pass filtering of the measured attenuation in the CT reconstruction and the partial volume effect. Another hypothesis is that there are dynamic effects caused by diffusion on the contrast concentration that cannot be explained by pure advection.

1.5 Aim and thesis outline

In this thesis, a new flow estimation method based on a CCTA image is proposed called advection diffusion flow estimation (ADFE) method. For verifying ADFE we use a spectral element solver which is developed to obtain numerical approximations of the velocity and concentration field with the required accuracy. This enables approximating the contrast distribution found in an actual CCTA image and a direct comparison of the obtained flow from ADFE with the one used as input to the solver. This one-to-one comparison makes it possible to quantify different sources of error compared to only validating on actual CCTA images. The methodology of this spectral element method solver is shown in Chapter 2 together with examples and verification problems to prove proper implementation. All other chapters utilized this solver for verification of ADFE and all these models are explained in detail in Chapter 2. For Chapter 3 a semi-analytical solution of the 2D axisymmetric advection diffusion equation was derived and implemented in the ADFE method. This was verified on numerical 2D axisymmetric software phantoms and finally compared to the best method currently available, i.e. TAFE, to demonstrate its improvement. In Chapter 4, ADFE was extended from simple axisymmetric vessels to 3D coronary trees. Similar to Chapter 3, this tree-based ADFE was verified using patient specific software phantoms and compared to TAFE. The imaging effects causing the non-linear mismatch between concentration contrast agent and measured intensity are explained in Chapter 5. By examining virtual CT images of the software phantoms used in Chapters 3 and 4, a correction term for this mismatch was derived and verified using ADFE.

References

- Bae, Y. G., Hwang, S. T., Han, H., Kim, S. M., Kim, H. Y., Park, I., Lee, J. M., Moon, Y. J., & Choi, J. H. (2018). Non-invasive coronary physiology based on computational analysis of intracoronary transluminal attenuation gradient. *Sci Rep.*, *8*(1), 4692. <https://doi.org/10.1038/s41598-018-23134-7>
- Choi, J. H., Koo, B. K., Yoon, Y. E., Min, J. K., Song, Y. B., Hahn, J. Y., Choi, S. H., Gwon, H. C., & Choe, Y. H. (2012). Diagnostic performance of intracoronary gradient-based methods by coronary computed tomography angiography for the evaluation of physiologically significant coronary artery stenoses: A validation study with fractional flow reserve. *Eur Heart J Cardiovasc Imaging*, *13*(12), 1001–1007. <https://doi.org/10.1093/ehjci/jes130>
- Choy, J. S., & Kassab, G. S. (2008). Scaling of myocardial mass to flow and morphometry of coronary arteries. *J Appl Physiol*, *104*(5). <https://doi.org/10.1152/jappphysiol.01261.2007>
- Eslami, P., Seo, J. H., Rahsepar, A. A., Richard, A. G., Lardo, A. C., & Mittal, R. (2015). Computational study of computed tomography contrast gradients in models of stenosed coronary arteries. *J Biomech Eng.*, *137*(9). <https://doi.org/10.1115/1.4030891>
- Eslami, P., Seo, J. H., Rahsepar, A. A., Shafique, A., Rollison, S. F., Lardo, A. C., Mittal, R., & Chen, M. Y. (2022). A noninvasive assessment of flow based on contrast dispersion in computed tomography angiography: A computational and experimental phantom study. *J Biomech Eng.*, *144*(9). <https://doi.org/10.1115/1.4053997>
- Fujimoto, S., Giannopoulos, A. A., Kumamaru, K. K., Matsumori, R., Tang, A., Kato, E., Kawaguchi, Y., Takamura, K., Miyauchi, K., Daida, H., Rybicki, F. J., & Mitsouras, D. (2018). The transluminal attenuation gradient in coronary ct angiography for the detection of hemodynamically significant disease: Can all arteries be treated equally? *Br J Radiol.*, *91*(1087). <https://doi.org/10.1259/bjr.20180043>
- Gould, K. L., & Lipscomb, K. (1974). Effects of coronary stenosis on coronary flow reserve and resistance. *Am J Cardiol.*, *34*(1), 48–55.
- Lardo, A. C., Rahsepar, A. A., Seo, J. H., Eslami, P., Korley, F., Kishi, S., Abd, T., Mittal, R., & George, R. T. (2015). Estimating coronary blood flow using ct transluminal attenuation flow encoding: Formulation, preclinical validation, and clinical feasibility. *J Cardiovasc Comput Tomogr.*, *9*(6), 559–566. <https://doi.org/10.1016/j.jcct.2015.03.018>
- Park, E. A., Lee, W., Park, S. J., Kim, Y. K., & Hwang, H. Y. (2016). Influence of coronary artery diameter on intracoronary transluminal attenuation gradient during ct angiography. *JACC Cardiovasc Imaging*, *9*(9), 1074–1083.

- Pijls, N. H., Fearon, W. F., Tonino, P. A., Siebert, U., Ikeno, F., Bornschein, B., van't Veer, M., Klauss, V., Manoharan, G., Engstrøm, T., Oldroyd, K. G., Ver Lee, P. N., MacCarthy, P. A., & De Bruyne, B. (2010). Fractional flow reserve versus angiography for guiding percutaneous coronary intervention in patients with multivessel coronary artery disease: 2-year follow-up of the fame (fractional flow reserve versus angiography for multivessel evaluation) study. *J Am Coll Cardiol.*, *56*(3), 177–184. <https://doi.org/10.1016/j.jacc.2010.04.012>
- Pijls, N. H., & Sels, J. W. (2012). Functional measurement of coronary stenosis. *J Am Coll Cardiol.*, *59*(12), 1045–1057. <https://doi.org/10.1016/j.jacc.2011.09.077>
- Stary, H. C., Chandler, A. B., Dinsmore, R. E., Fuster, V., Glagov, S., Insull, W. J., Rosenfeld, M. E., Schwartz, C. J., Wagner, W. D., & Wissler, R. W. (1995). A definition of advanced types of atherosclerotic lesions and a histological classification of atherosclerosis. a report from the committee on vascular lesions of the council on arteriosclerosis, american heart association. *Circulation*, *92*(5). <https://doi.org/10.1161/01.cir.92.5.1355>
- Steigner, M. L., Mitsouras, D., Whitmore, A. G., Otero, H. J., Wang, C., Buckley, O., Levit, N. A., Hussain, A. Z., Cai, T., Mather, R. T., Smedby, O., DiCarli, M. F., & Rybicki, F. J. (2015). Iodinated contrast opacification gradients in normal coronary arteries imaged with prospectively ecg-gated single heart beat 320-detector row computed tomography. *Circ Imaging*, *137*(9), 179–186. <https://doi.org/10.1161/CIRCIMAGING.109.854307>
- Stuijzfand, W. J., Danad, I., Raijmakers, P. G., Marcu, C. B., Heymans, M. W., van Kuijk, C. C., van Rossum, A. C., Nieman, K., Min, J. K., Leipsic, J., van Royen, N., & Knaapen, P. (2014). Additional value of transluminal attenuation gradient in ct angiography to predict hemodynamic significance of coronary artery stenosis. *JACC Cardiovasc Imaging*, *7*(4), 374–386. <https://doi.org/10.1016/j.jcmg.2013.12.013>
- Taylor, C. A., Fonte, T. A., & Min, J. K. (2013). Computational fluid dynamics applied to cardiac computed tomography for noninvasive quantification of fractional flow reserve: Scientific basis. *J Am Coll Cardiol.*, *61*(22), 2233–2241. <https://doi.org/10.1016/j.jacc.2012.11.083>
- Tonino, P. A., De Bruyne, B., Pijls, N. H., Siebert, U., Ikeno, F., van't Veer, M., Klauss, V., Manoharan, G., Engstrøm, T., Oldroyd, K. G., Ver Lee, P. N., MacCarthy, P. A., Fearon, W. F., & (2009), F. S. I. (2009). Fractional flow reserve versus angiography for guiding percutaneous coronary intervention. *The New England journal of medicine*, *360*(3), 213–224. <https://doi.org/10.1056/NEJMoa0807611>
- Tsao, C. W., Aday, A. W., Almarzooq, Z. I., Alonso, A., Beaton, A. Z., Bittencourt, M. S., Boehme, A. K., Buxton, A. E., Carson, A. P., Commodore-Mensah,

Y., Elkind, M., Evenson, K. R., Eze-Nliam, C., Ferguson, J. F., Generoso, G., Ho, J. E., Kalani, R., Khan, S. S., Kissela, B. M., ... Martin, S. S. (2022). Heart disease and stroke statistics-2022 update: A report from the american heart association. *Circulation*, *145*(8), e153–e639. <https://doi.org/10.1161/CIR.0000000000001052>

Abstract

In this chapter, we provide a derivation of our spectral element method (SEM) solver specialised for tubular shaped geometries. The necessary mathematical formulas for SEM and the spectral element formulation for the advection diffusion and Navier-Stokes equations in both axi-symmetric cylindrical and Cartesian coordinates are derived and verified. For meshing tubular geometries element structures are explained together with how to mesh bifurcations for tree geometries. Finally, in order to show the added benefit of SEM over a traditional finite element method we compare them in a benchmark problem.

2.1 Introduction

In recent years, numerical methods have become more and more relevant in the study of complex systems and are now consistently used to find approximated solutions of complex partial differential equations (PDEs) representing a physical system. PDEs allow us to investigate biological phenomena that are difficult to investigate experimentally. Additionally, PDEs can provide highly detailed information computationally that is sometimes impossible to get experimentally. This stimulates the research done in improving numerical methods for solving PDEs to be faster, more accurate and more robust.

A popular method, which subdivides the domain of interest into elements,

is the finite element method (FEM). In each domain, a discretization of the function space into piecewise polynomials defined per element is used to describe an approximate solution. By connecting the elements, a large system of equations is constructed that can be solved by appropriate direct or iterative methods. The ability of the discretized function space to describe the real solution partially determines the accuracy of the approximation. The spectral element method (SEM) increases accuracy and convergence of the solution by using higher-order polynomial functions combined with optimal numerical integration methods. The spectral convergence rate by increasing the order of the polynomials (p-convergence) is higher than the convergence rate achieved by adding the same amount of points by subdividing the elements (h-convergence). However, some geometries need a certain amount of elements to be represented geometrically. This leads to a trade off between the order of the polynomial functions and the geometric representation of the domain.

In this chapter, a SEM solver specific for our purpose is described in detail. It is used for calculating fluid flow and solute transport. This solver is specialised for applications in tubular shaped domains. Furthermore, it computes stable solutions for problems having a high Peclet number, i.e. which are characterized by strong advection and as a result high gradients in the solute concentration field. In general, for high Peclet numbers, FEM requires stabilisation methods to cope with the high gradients impeding the accuracy. By utilising higher-order elements in the SEM, we avoid the need for stabilisation methods. To illustrate this, a comparison between linear FEM and SEM is made in Section 2.7.

2.2 Pseudo spectral approximation

For finding an approximated solution u_h of solution u the L_2 -error $\|u - u_h\|$ can be described by Céa's lemma. It states that this error does not depend on the problem itself, but only on the way u is close to the function space of u_h , or i.e. on how well u can be interpolated on this function space. This means that improvements in accuracy and convergence can be expected when utilizing higher order polynomials to describe u_h . the spectral element method uses higher order orthogonal polynomials together with optimal interpolation and integration to maximize convergence rate of $\|u - u_h\|$ or i.e. reach spectral convergence. In this study, we use a pseudo-spectral approximation based on Legendre polynomials. The pseudo approximation refers to the usage of Lagrange polynomials instead of Legendre polynomials. The spectral conver-

gence is preserved when a Legendre-Gauss quadrature is used and the interpolation points correspond with the quadrature points. For proofs and more details, we refer to the book of Canuto et al. (1988), Sections. 2.2 and 2.3. This results in a linear set of equations with spectral convergence of $\|u - u_h\|$ by increasing the order N of the Legendre polynomials P_N . In this section, we give a brief description of P_N and forms of the Legendre-Gauss quadrature types used in this study. Finally, we derive the basis function based on Lagrange polynomials for each Legendre-Gauss quadrature for a reference element and show how to map these to a local element.

2.2.1 Legendre Polynomials

The Legendre polynomial of degree N $P_N(x)$ is defined as the solution of the differential equation

$$(1 - x^2)P_N''(x) - 2xP_N'(x) + N(N - 1)P_N(x) = 0. \quad (2.2.1)$$

P_N can also be calculated more easily by Bonnet's recursion formula

$$P_N(x) = \frac{2N - 1}{N}xP_{N-1}(x) - \frac{N - 1}{N}P_{N-2}(x), \quad N = 2, 3, \dots \quad (2.2.2)$$

with $P_0(x) = 1$ and $P_1(x) = x$. Note that for calculating derivatives of P_N this formula can also be used.

2.2.2 Legendre-Gauss quadrature

The Legendre-Gauss quadrature is a fast and accurate method for numerical integration of a definite integral by the following formula

$$\int_{-1}^1 f(x)dx \approx \sum_{i=1}^N w_i f(\xi_i), \quad (2.2.3)$$

with $f(x)$ a function, w_i and ξ_i the respectively i -th weight and Gauss quadrature point. Depending on the choice on having points at the boundaries $x = \pm 1$, there are three types of Legendre-Gauss quadratures, namely Legendre-Gauss (no boundary points), Legendre-Gauss-Radau (one boundary point) and Legendre-Gauss-Lobatto (two boundary points). Note that N involves both the order of the Legendre polynomial and the total number of Gauss quadrature points.

Legendre-Gauss

The Legendre-Gauss quadrature has no quadrature points at the boundary. Its quadrature points are equal to the roots of $P_N(x)$ and the weights can be calculated by

$$w_i = \frac{2}{(1 - \xi_i^2)P'_N(\xi_i)^2} \quad \text{for } i = 1, \dots, N. \quad (2.2.4)$$

Legendre-Gauss-Radau

If only one point is needed at the boundaries, specifically at $x = -1$, then the Legendre-Gauss-Radau is used. The quadrature points are equal to the roots of $P_{N-1}(x) + P_N(x)$ and the weights are equal to

$$w_i = \frac{1 - \xi_i}{N^2 P_{N-1}(\xi_i)^2} \quad \text{for } i = 1, \dots, N. \quad (2.2.5)$$

Legendre-Gauss-Lobatto

Finally, the Legendre-Gauss-Lobatto quadrature contains both boundary points and all quadrature points are equal to the roots of $(1 - x^2)P'_{N-1}(x)$, for $N \geq 2$. The weights are equal to

$$w_i = \frac{2}{N(N-1)P_{N-1}(\xi_i)} \quad \text{for } i = 1, \dots, N \text{ and } N \geq 2. \quad (2.2.6)$$

2.2.3 Lagrange interpolation polynomials

The basis functions ϕ used in our SEM are based on a Lagrange interpolation polynomial. In order to still achieve spectral convergence using Lagrange polynomial, ϕ has to be defined at one of the three Legendre-Gauss quadrature points described above. Matching the interpolation and integration points also adds the benefit that the i -th computed Lagrange coefficient u_i^h is equal to the solution at this point

$$u_i^h = u^h(\xi_i) \quad \text{for } i = 1, \dots, N. \quad (2.2.7)$$

In general for Lagrange polynomials it can be derived that when the interpolation points are equal to the roots of a function $f(x)$ that a general formula for ϕ can be derived as

$$\phi_i(x) = \begin{cases} \frac{f(x)}{f'(\xi_i)(x - \xi_i)} & \text{if } x \neq \xi_i \\ 1 & \text{if } x = \xi_i \end{cases} \quad \text{for } i = 1, \dots, N. \quad (2.2.8)$$

For SEM a first order derivative of ϕ is also required which can be calculated by

$$\frac{d\phi_i}{dx} = \begin{cases} \frac{f'(x)(x-\xi_i)-f(x)}{f'(\xi_i)(x-\xi_i)^2} & \text{if } x \neq \xi_i \\ \frac{f''(\xi_i)}{2f'(\xi_i)} & \text{if } x = \xi_i \end{cases} \quad \text{for } i = 1, \dots, N. \quad (2.2.9)$$

Legendre-Gauss-Lagrange

Substituting $f(x) = P_N(x)$ for the Legendre-Gauss-Lagrange results into

$$\phi_i(\xi_j) = \begin{cases} 0 & \text{if } i \neq j \\ 1 & \text{if } i = j \end{cases} \quad \text{for } i = 1, \dots, N \quad (2.2.10)$$

and

$$\left. \frac{d\phi_i}{dx} \right|_{x=\xi_j} = \begin{cases} \frac{P'_N(\xi_j)}{P'_N(\xi_i)(\xi_j-\xi_i)} & \text{if } i \neq j \\ \frac{P''_N(\xi_i)}{2P'_N(\xi_i)} & \text{if } i = j \end{cases} \quad \text{for } i = 1, \dots, N. \quad (2.2.11)$$

Legendre-Gauss-Radau-Lagrange

Substituting $P_{N-1}(x) + P_N(x)$ for the Legendre-Gauss-Radau-Lagrange results into

$$\phi_i(\xi_j) = \begin{cases} 0 & \text{if } i \neq j \\ 1 & \text{if } i = j \end{cases} \quad \text{for } i = 1, \dots, N \quad (2.2.12)$$

and

$$\left. \frac{d\phi_i}{dx} \right|_{x=\xi_j} = \begin{cases} \frac{P'_{N-1}(\xi_j)+P'_N(\xi_j)}{(P'_{N-1}(\xi_i)+P'_N(\xi_i))(\xi_j-\xi_i)} & \text{if } i \neq j \\ \frac{P''_{N-1}(\xi_j)+P''_N(\xi_j)}{2(P'_{N-1}(\xi_i)+P'_N(\xi_i))} & \text{if } i = j \end{cases} \quad \text{for } i = 1, \dots, N. \quad (2.2.13)$$

Legendre-Gauss-Lobatto-Lagrange

Substituting $f(x) = (1-x^2)P'_{N-1}(x)$ for the Legendre-Gauss-Lobatto-Lagrange results into

$$\phi_i(\xi_j) = \begin{cases} 0 & \text{if } i \neq j \\ 1 & \text{if } i = j \end{cases} \quad \text{for } i = 1, \dots, N \quad (2.2.14)$$

and

$$\frac{d\phi_i}{dx} \Big|_{x=\xi_j} = \begin{cases} \frac{P_{N-1}(\xi_j)}{(\xi_j - \xi_i)P_{N-1}'(\xi_i)} & \text{if } i \neq j \\ \frac{P_{N-1}'(\xi_i)}{2P_{N-1}'(\xi_i)} & \text{if } i = j \end{cases} \quad \text{for } i = 1, \dots, N. \quad (2.2.15)$$

2.2.4 Isoparametric Mapping

For utilising the Gauss quadratures and basis functions described above, a mapping needs to be done from the local coordinates x with element points at x_i to the reference coordinates x_0 with element points at ξ_i . The following relationship is used to map the integration $dx = \frac{dx}{dx_0} dx_0$. As for derivative the chain rule is used $\frac{d}{dx} = \left(\frac{dx}{dx_0}\right)^{-1} \frac{d}{dx_0}$. For computing the deformation term we utilise the same basis function for x

$$x = \sum_{i=1}^N x_i \phi_i \quad (2.2.16)$$

and derive

$$\frac{dx}{dx_0} = \sum_{i=1}^N x_i \frac{d\phi_i}{dx_0}. \quad (2.2.17)$$

2.2.5 Higher dimensions

The extension of Section 2.2.4 to two or three dimensional problem is easily achieved as the integration points, weights and basis functions can be written as a tensor product which for three dimensional problems results into

$$\begin{aligned} w_i &= w_x w_y w_z, \\ \xi_i &= (\xi_x, \xi_y, \xi_z), \\ \phi_i &= \phi_x \phi_y \phi_z. \end{aligned} \quad (2.2.18)$$

For the isoparametric mapping the deformation matrix between the reference and local element, which is called the Jacobian matrix J , needs to be computed. In three dimension for mapping at (x_i, y_i, z_i) , J_i is equal to

$$J_i = \sum_{j=1}^N \begin{pmatrix} \frac{\partial \phi_i}{\partial x_0} \Big|_{x=\xi_j} x_j & \frac{\partial \phi_i}{\partial x_0} \Big|_{x=\xi_j} y_j & \frac{\partial \phi_i}{\partial x_0} \Big|_{x=\xi_j} z_j \\ \frac{\partial \phi_i}{\partial y_0} \Big|_{x=\xi_j} x_j & \frac{\partial \phi_i}{\partial y_0} \Big|_{x=\xi_j} y_j & \frac{\partial \phi_i}{\partial y_0} \Big|_{x=\xi_j} z_j \\ \frac{\partial \phi_i}{\partial z_0} \Big|_{x=\xi_j} x_j & \frac{\partial \phi_i}{\partial z_0} \Big|_{x=\xi_j} y_j & \frac{\partial \phi_i}{\partial z_0} \Big|_{x=\xi_j} z_j \end{pmatrix}. \quad (2.2.19)$$

The mapping of the integral and first order derivative can then be written as follow

$$\begin{aligned} dx dy dz &= \det(J) dx_0 dy_0 dz_0, \\ \nabla &= J^{-1} \nabla_0. \end{aligned} \quad (2.2.20)$$

For two dimensional problems the same equations can be used where all terms involving the z component are removed.

2.3 Spectral element formulation

In this section we formulate the linear set of equations, which are used in either FEM or SEM, for the advection diffusion equation and Navier-Stokes equation for both the Cartesian and axi-symmetric basis. Note that for implementing these equations in the SEM solver, we take advantage of the fact that ϕ is equal to the unity matrix which will reduce the number of summations in the final equations where present.

2.3.1 Advection diffusion equation

The passive advection diffusion equation with no source or reaction term is written as

$$\frac{\partial C}{\partial t} + \vec{v} \cdot \nabla C = D \nabla^2 C. \quad (2.3.1)$$

with C the concentration, t the time, \vec{v} the velocity and D the diffusion coefficient. In order to solve this equation we first apply the Galerkin weighted residual method to write the strong form of this equation

$$\sum_{i=1}^N \sum_{j=1}^N \int_{\Omega} \phi_i \phi_j \frac{dC_j}{dt} + \phi_i \vec{v} \cdot \nabla \phi_j C_j - D \phi_i \nabla^2 \phi_j C_j d\Omega = 0, \quad (2.3.2)$$

with C_j the j -th expansion coefficient. Integration by parts is then used on the second order term to derive the weak form and Neumann boundary condition of the equation

$$\begin{aligned} \sum_{i=1}^N \sum_{j=1}^N \int_{\Omega} \phi_i \phi_j \frac{dC_j}{dt} + \phi_i \vec{v} \cdot \nabla \phi_j C_j + \\ D \nabla \phi_i \cdot \nabla \phi_j C_j d\Omega = D \int_{\Gamma} \psi_i \nabla C \cdot \vec{n}, \end{aligned} \quad (2.3.3)$$

with \vec{n} and ψ the normal and basis functions on surface Γ . The added $\nabla C \cdot \vec{n}$ term represents the amount of flux through Γ . We then divide the domain into K elements and on each element apply the pseudo spectral methods described in Section 2.2. Substituting this into Equation 2.3.3, we derive the following linear set of equations

$$\mathcal{M} \frac{d\tilde{C}}{dt} + \mathcal{K}\tilde{C} = h_\Gamma, \quad (2.3.4)$$

with \tilde{C} a vector containing C on every mesh node, h_Γ a vector containing the Neumann boundary conditions and the following element matrices calculated as

$$\begin{aligned} \mathcal{M}_{ij}^e &= \sum_{k=1}^N \phi_i(\xi_k) \phi_j(\xi_k) w_k \det(J_k), \\ \mathcal{K}_{ij}^e &= \sum_{k=1}^N (\phi_i(\xi_k) \vec{v}_k \cdot \nabla \phi_j(\xi_k) + \\ &\quad D \nabla \phi_i(\xi_k) \cdot \nabla \phi_j(\xi_k)) w_k \det(J_k), \end{aligned} \quad (2.3.5)$$

where ∇ is mapped by Equation 2.2.20. For computing the full set of linear equations, the element matrices are added up based on the connectivity of the entire mesh.

2.3.2 Axi-symmetric advection diffusion

If we assume an axi-symmetric velocity and concentration field we can write the advection diffusion equation in the cylindrical setting as

$$\frac{\partial C}{\partial t} + v_z \frac{\partial C}{\partial z} + v_r \frac{\partial C}{\partial r} = D \left(\frac{\partial^2 C}{\partial z^2} + \frac{1}{r} \frac{\partial}{\partial r} \left(r \frac{\partial C}{\partial r} \right) \right), \quad (2.3.6)$$

with r the radial direction and z the axial direction. Similar to Cartesian advection diffusion equation we can derive the weak form of Equation 2.3.6 as

$$\begin{aligned} \sum_{i=1}^N \sum_{j=1}^N \int_{\Omega} \phi_i \phi_j \frac{dC_j}{dt} + (\phi_i v_z \frac{\partial \phi_j}{\partial z} + \phi_i v_r \frac{\partial \phi_j}{\partial r}) C_j + \\ D \left(\frac{\partial \phi_i}{\partial z} \frac{\partial \phi_j}{\partial z} - \frac{1}{r} \phi_i \frac{\partial \phi_j}{\partial r} + \frac{\partial \phi_i}{\partial r} \frac{\partial \phi_j}{\partial r} \right) C_j d\Omega = \\ D \int_{\Gamma} \psi_i \left(\frac{\partial C}{\partial z} n_z + \frac{\partial C}{\partial r} n_r \right) d\Gamma \end{aligned} \quad (2.3.7)$$

and also we substitute the pseudo spectral element from Section 2.2 to derive

$$\mathcal{M} \frac{d\tilde{C}}{dt} + \mathcal{K}\tilde{C} = h_{\Gamma}, \quad (2.3.8)$$

but now the element matrices are equal to

$$\begin{aligned} \mathcal{M}_{ij}^e &= \sum_{k=1}^N \phi_i(\xi_k) \phi_j(\xi_k) w_k \det(J_k), \\ \mathcal{K}_{ij}^e &= \sum_{k=1}^N \left(\phi_i v_z \frac{\partial \phi_j}{\partial z} + \phi_i v_r \frac{\partial \phi_j}{\partial r} + \right. \\ &\quad \left. D \left(\frac{\partial \phi_i}{\partial z} \frac{\partial \phi_j}{\partial z} - \frac{1}{r} \phi_i \frac{\partial \phi_j}{\partial r} + \frac{\partial \phi_i}{\partial r} \frac{\partial \phi_j}{\partial r} \right) \right) w_k \det(J_k), \end{aligned} \quad (2.3.9)$$

with the mapping of all derivative computed by Equation 2.2.20.

2.3.3 Navier-Stokes equation

The Navier-Stokes equation for an incompressible Newtonian material is written as

$$\begin{aligned} \rho \left(\frac{\partial \vec{v}}{\partial t} + \vec{v} \cdot \nabla \vec{v} \right) &= -\nabla p + \mu \nabla \cdot \mathcal{D}, \\ \nabla \cdot \vec{v} &= 0, \end{aligned} \quad (2.3.10)$$

with ρ the fluid density, \vec{v} the velocity field, p the pressure, μ the fluid viscosity and $\mathcal{D} = \nabla \vec{v} + (\nabla \vec{v})^T$ the viscous stress tensor for a Newtonian fluid. Similar to the advection diffusion equation we discretize both \vec{v} and p by respectively ϕ and χ

$$\begin{aligned} \vec{v} &= \sum_{i=1}^{N_v} \phi_i \vec{v}_i, \\ p &= \sum_{i=1}^{N_p} \chi_i p_i, \end{aligned} \quad (2.3.11)$$

to derive the weak form

$$\begin{aligned}
& \sum_{i=1}^{N_v} \sum_{j=1}^{N_v} \int_{\Omega} \rho(\phi_i \phi_j \frac{d\vec{v}_j}{dt} + \phi_i \vec{v}_j \cdot \nabla \phi_j \vec{v}_j) + \mu(\nabla \phi_i \cdot \nabla \phi_j \mathcal{I} + \nabla \phi_j \nabla \phi_i) \cdot \vec{v}_j d\Omega - \\
& \sum_{i=1}^{N_v} \sum_{j=1}^{N_p} \int_{\Omega} \nabla \phi_i \chi_j p_j d\Omega = \int_{\Gamma} \psi_i (-p \mathcal{I} + \mu \mathcal{D}) \cdot \vec{n} d\Gamma, \\
& \sum_{i=1}^{N_p} \sum_{j=1}^{N_v} \int_{\Omega} \chi_i \nabla \phi_j d\Omega = 0,
\end{aligned} \tag{2.3.12}$$

with \mathcal{I} the unity matrix. Finally the pseudo spectral approximation from Section 2.2 is substituted to derive in matrix notation the following set of equations

$$\begin{pmatrix} \mathcal{M} & 0 \\ 0 & 0 \end{pmatrix} \begin{pmatrix} \frac{d\tilde{v}}{dt} \\ \tilde{o} \end{pmatrix} + \begin{pmatrix} \mathcal{K} & \mathcal{B}^T \\ \mathcal{B} & 0 \end{pmatrix} \begin{pmatrix} \tilde{v} \\ \tilde{p} \end{pmatrix} = \begin{pmatrix} h_{\Gamma} \\ 0 \end{pmatrix} \tag{2.3.13}$$

with the element matrices calculated by

$$\begin{aligned}
\mathcal{M}_{ij}^e &= \rho \sum_{k=1}^N \phi_i(\xi_k) \phi_j(\xi_k) w_k \det(J_k) \mathcal{I}, \\
\mathcal{K}_{ij}^e &= \sum_{k=1}^N (\rho \phi_i(\xi_k) \vec{v}_k \cdot \nabla \phi_j(\xi_k) \mathcal{I} + \\
& \quad \mu (\nabla \phi_i(\xi_k) \cdot \nabla \phi_j(\xi_k) \mathcal{I} + \nabla \phi_j(\xi_k) \nabla \phi_i(\xi_k))) w_k \det(J_k), \\
\mathcal{B}_{ij}^e &= \sum_{k=1}^N \nabla \phi_i(\xi_k) \chi_j(\xi_k) w_k \det(J_k),
\end{aligned} \tag{2.3.14}$$

and the mapping of all derivative computed by Equation 2.2.20.

2.3.4 Axi-symmetric Navier-Stokes equation

If we assume an axi-symmetric velocity and pressure field we can write Equation 2.3.10 as

$$\begin{aligned}
\rho \left(\frac{\partial \vec{v}}{\partial t} + \vec{v} \cdot \nabla \vec{v} \right) &= -\nabla p + \mu \left(\nabla \cdot \mathcal{D} + \left(\frac{1}{r} \frac{\partial v_r}{\partial r} - \frac{v_r}{r^2} \right)_r + \left(\frac{1}{r} \frac{\partial v_z}{\partial r} \right)_z \right), \\
\nabla \cdot \vec{v} + \frac{v_r}{r} &= 0,
\end{aligned} \tag{2.3.15}$$

with $\vec{v} = [v_r, v_z]$, $\nabla = [\frac{\partial}{\partial r}, \frac{\partial}{\partial z}]$ and the subscript indicating the component of \vec{v} or equations for the terms between parentheses. We can utilise the resemblance of these equations to the 2D form of Equation 2.3.13 to derive a similar linear set of equations. The differences are derived by substituting $\int_{\Omega} dx dy dz = 2\pi \int_{\Omega} r dr dz$, which result in scaling the weights with r $w_k^* = r_k w_k$ and adjusting the following matrices

$$\begin{aligned}\mathcal{K}_{ij}^{e*} &= \mathcal{K}_{ij;w_k^*}^e + \sum_{k=1}^N \frac{\mu}{r_k} \phi_i(\xi_k) \phi_j(\xi_k) w_k \det(J_k), \\ \mathcal{B}_{ij}^{e*} &= \mathcal{B}_{ij;w_k^*}^e + \sum_{k=1}^N \phi_i(\xi_k) \chi_j(\xi_k) w_k \det(J_k).\end{aligned}\quad (2.3.16)$$

2.3.5 Neumann Boundary condition

Both advection diffusion and Navier-Stokes equations contain Neumann boundary terms for respectively setting the amount of flux $\vec{f} = \nabla C$ or stress tension $\sigma = -p\mathcal{I} + \mu\mathcal{D}$ at a given surface. For calculating the normal vector \vec{n} we can use a surface basis function $\psi(s_1, s_2)$, with surface coordinates s_1 and s_2 , to calculate two vectors tangent to the surface as

$$\begin{aligned}\vec{t}_{1,i} &= \sum_{j=1}^N \frac{\partial \psi_i}{\partial s_1} \Big|_{s=\xi_j} x_j, \\ \vec{t}_{1,2} &= \sum_{j=1}^N \frac{\partial \psi_i}{\partial s_2} \Big|_{s=\xi_j} x_j\end{aligned}\quad (2.3.17)$$

and compute $\vec{n} = \frac{\vec{t}_1 \times \vec{t}_2}{\|\vec{t}_1 \times \vec{t}_2\|}$. Mapping the surface integral to the reference surface element is also related to \vec{t}_1 and \vec{t}_2

$$d\Gamma = \|\vec{t}_1 \times \vec{t}_2\| d\Gamma_0. \quad (2.3.18)$$

This results in both Neumann boundary conditions at the i -th point to be equal to

$$\begin{aligned}h_{\Gamma,i} &= \sum_{j=1}^N w_j \psi_i(\xi_j) \vec{f}_j \cdot (\vec{t}_{1,j} \times \vec{t}_{2,j}), \\ h_{\Gamma,i} &= \sum_{j=1}^N w_j \psi_i(\xi_j) \sigma_j \cdot (\vec{t}_{1,j} \times \vec{t}_{2,j}).\end{aligned}\quad (2.3.19)$$

Similar derivation can also be performed for the 2D Cartesian or axis-symmetric Neumann boundary conditions.

2.4 Solver

For solving the final set of equations we use the Generalised-alpha method for the time integration (Jansen et al., 2000). For the Navier-Stokes equation the Simplec method is used as a fast iterative solver (Cyr et al., 2012). For deriving the Newton iteration the velocity inside of \mathcal{K} is assumed to be constant and at each new iteration equal to the previous iteration. Furthermore, to guarantee the Ladyzhenskaya–Babuška–Brezzi condition we restrict the polynomial order of the velocity N_v to be higher than the polynomial order of the pressure N_p . For solving the linear set of equations we either perform a LU factorization, if we can reuse the inverse matrix, or the BiCGSTAB method if the solved matrix changes after each iteration.

2.5 Mesher

The use of higher order hexahedron elements requires a structured mesher compared to tetrahedral elements which can be meshed using an unstructured mesher. This means a predefined orientation of elements or i.e. an element structure that is repeated and deformed to fit the meshed object. For the unstructured mesher a tessellation method is used to fill a surface mesh with elements while ensuring proper shaped elements. This is done by iteratively adding or removing elements to meet a certain requirement on the general shape of the elements. Comparing the two methods it can already be concluded that the structured mesher is much faster and more robust compared to unstructured however a new element structure will need to be defined for each new general shape, which can be time consuming. In this thesis beside the straightforward cube or square shape meshes we define three different kinds of meshes, namely the 2D axis-symmetric mesh, 3D tubular mesh and an arterial tree mesh.

2.5.1 2D axis-symmetric mesh

For solving differential equations in axis-symmetric coordinates special care needs to be taken for the singularity at $r = 0$ caused by the $1/r$ term inside the differential equation. This means that using a simple square mesh with

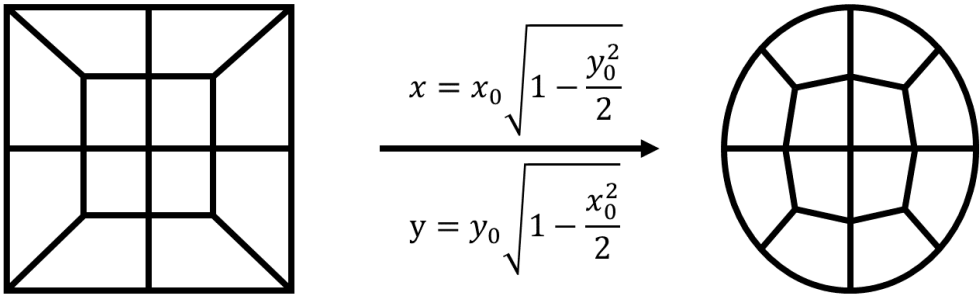


Figure 2.1: Schematics of the cylindrical structure before and after transforming the square into a circular shape. In this schematic two elements are chosen in radial direction and four in circumferential direction.

Gauss-Lobatto elements will end up with points at this singularity. Gauss-Radau integration in the radial direction with the boundary point at the wall and Gauss-Lobatto in the axial direction circumvents this singularity and for retaining connectivity only one element is therefore present in the radial direction. Using this element structure an accurate solution is still achieved by using a high order polynomial in the radial direction.

2.5.2 Tubular mesh

For a tubular mesh a circular structure needs to be defined that is repeated in the axial direction. If we define a square between -1 and 1 in x and y direction we can transform this square into a circle using

$$\begin{aligned} x &= x_0 \sqrt{1 - \frac{y_0^2}{2}} \\ y &= y_0 \sqrt{1 - \frac{x_0^2}{2}}. \end{aligned} \quad (2.5.1)$$

When examining the inverted Jacobian of this transformation it can be concluded that this will go to infinity at $(x_0 = \pm 1, y_0 = \pm 1)$ or in other words the four corners of the original square. To prevent this from happening in the computation of the linear set of equations we place the element boundaries at these four corners ending up with the schematic structure shown in Figure 2.1. The number of elements in the radial and circumferential directions can be added, however increasing N in the polynomial order is more beneficial in the convergence of the solution.

2.5.3 Arterial tree mesh

An arterial tree mesh consists of several vessel segments merged together with bifurcations. Our arterial tree mesh input data consists of centerline point coordinates combined with normal direction, radius and distance to the previous point for each vessel segment. By adding to each segment which two daughter vessels are connected to its outlet, if present, we achieve the full connectivity and geometry of the arterial tree mesh. Firstly, the individual segments are meshed using the tubular mesher, described above, with the same amount of elements as centerline points. These meshes can then be deformed to match the input data. This is performed by first translating each circle to match its center with the centerline point. Next each circle is rotated around this center to match the respective normal and stretched or compressed to match the input radius. If the order of the polynomial in the axial direction is higher than one or optionally more elements are required between centerline points, a cubic Hermite spline is used to interpolate between two centerline points. The cubic Hermite spline uses the position and normal of two consecutive points as input and smoothly transits between them, which ensures a smooth mesh.

For the bifurcation element structure the cross-sectional structure of each vessel segment needs to be split in half in order to connect the parent vessel to two daughter vessels. The inspiration for defining the bifurcation element structure was taken from De Santis (2011). From Figure 2.1 it can be concluded that the two lines (at $x = 0$ and $y = 0$) are perfectly splitting the structure in half thus resulting into four different splitting configurations. Each segment is therefore rotated in circumferential direction to line up a possible configuration with the least amount of rotation required to prevent highly deformed elements. On the bifurcation plane, which is defined by the centers of each cross-section connected to the bifurcation, three functions indicating the wall are defined which connect the three vessel segments. This wall function is defined again using cubic Hermite splines. A visualisation of these functions and element configurations are shown in Figure 2.2a. Next a predefined number of elements are connected to the parent vessel on which each half of the cross-sectional element structure runs perpendicular to its respective wall function, which is shown in Figure 2.2b. This is repeated for the second and third step of connecting each daughter vessel, which is shown in Figures 2.2c and 2.2d. Finally, we can set the resolution of the bifurcation higher using a higher order polynomial in the radial or axial direction or add more elements in each of the three steps resulting in a smoother mesh shown in Figure 2.2e. A zoomed out representation of the entire mesh of each step is shown in Figure 2.3.

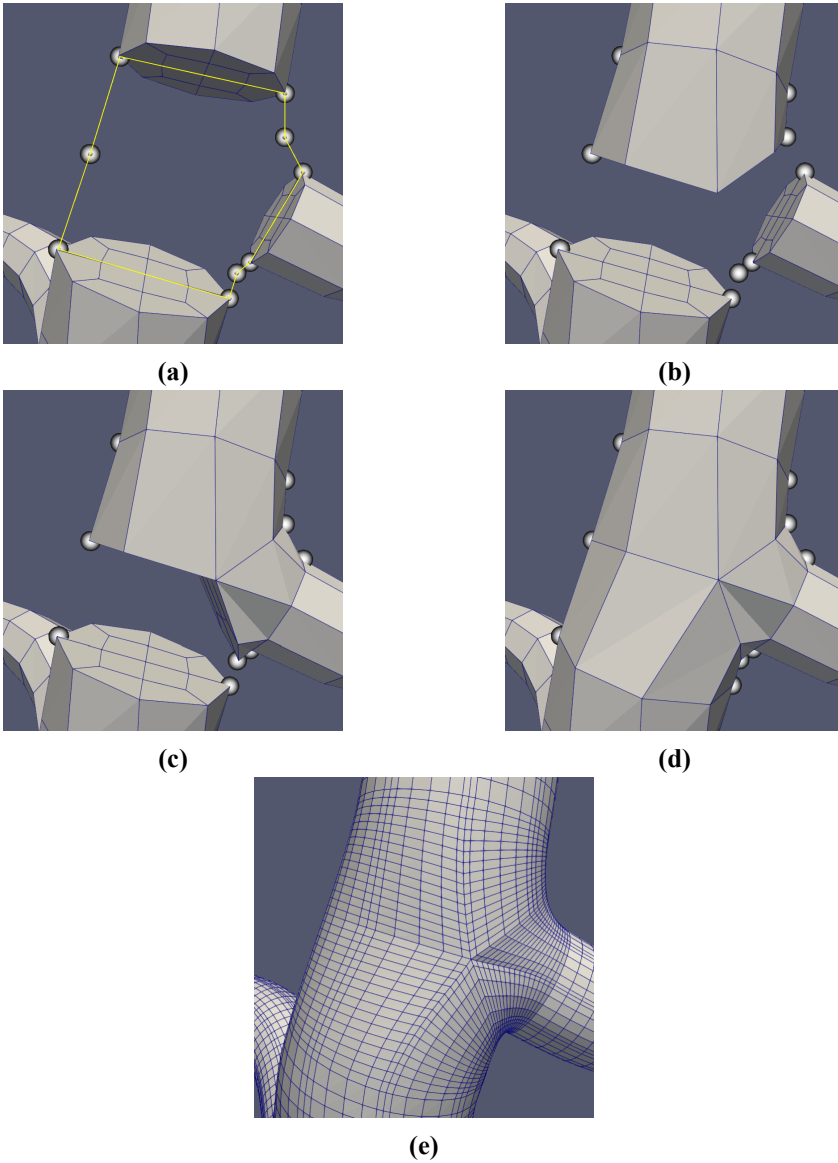


Figure 2.2: Figures show a visualisation of the meshing a bifurcation inside a LAD tree mesh. Starting with Figure a showing the cylindrical meshes of each vessel segment and the bifurcation plane points used to define the interpolation of the bifurcation wall. Next Figure b shows the mother vessel being split into two vessels and Figures c and d connects the mother vessel to each daughter vessel. Finally Figure e shows the same mesh but with a higher resolution, namely a fifth order in radial direction and second order in axial direction together with three axial elements between each centerline point inside the bifurcation 3×8 total elements. Note that in order to visualize this mesh each element was subdivided into linear elements resulting in the non-equidistantly spacing between points.

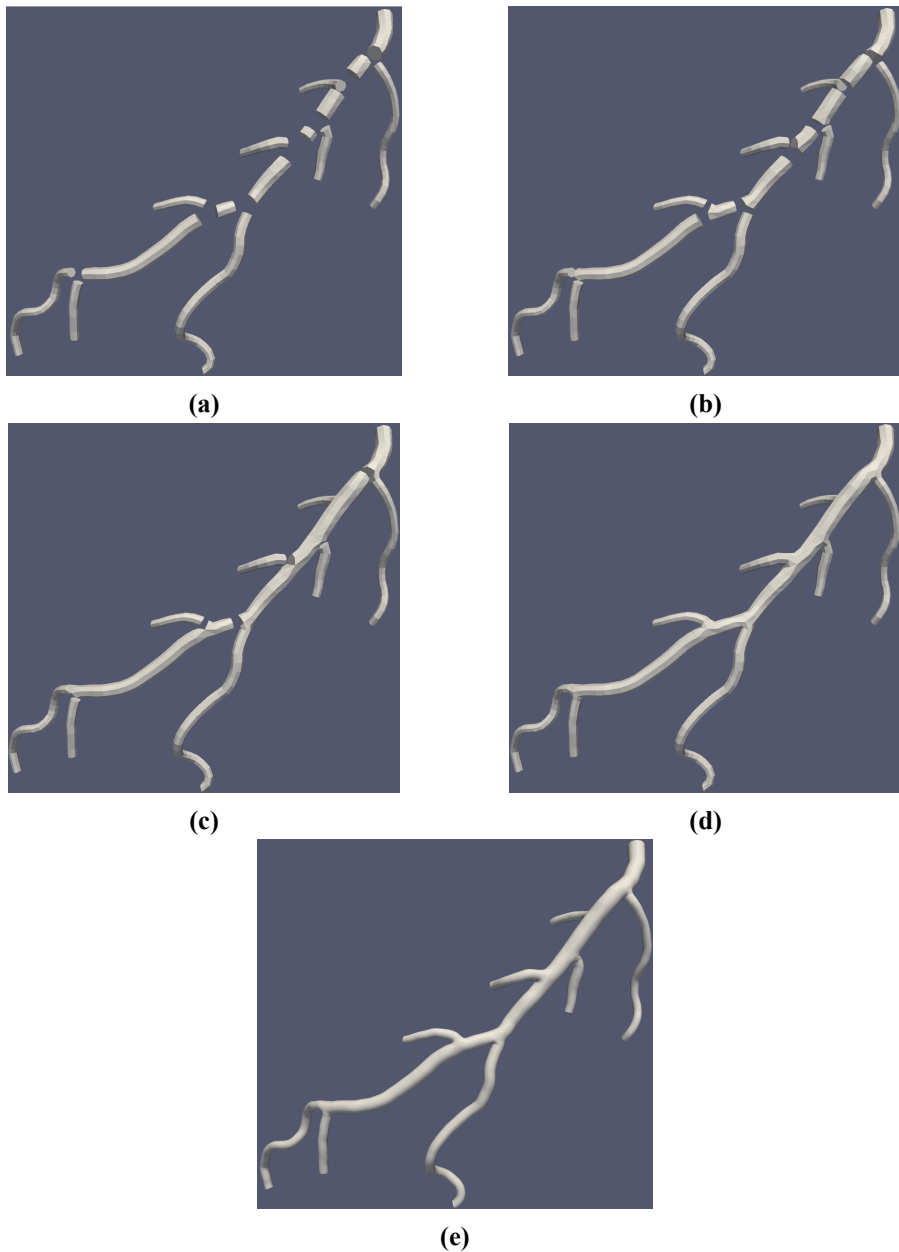


Figure 2.3: Figures show a visualisation of the meshing of all the bifurcation inside a LAD tree mesh. Starting with Figure a showing the cylindrical meshes of each vessel segment. Next Figure b shows the mother vessel being split into two vessels and Figures c and d connects the mother vessel to each daughter vessel. Finally Figure e shows the same mesh but with a higher resolution, namely a fifth order in radial direction and second order in axial direction together with three elements between each centerline points and inside the bifurcation 3x8 total elements.

2.6 Software verification

We verified our spectral element solver to ensure correctness of it and its implementation. A fabricated solution of the Navier-Stokes is used to test all terms at once. This was done by assuming an infinite differentiable velocity field with a pressure field. By filling this function into the Navier-Stokes equation a force vector \vec{f} was derived and substituted to ensure that the equation still holds. For the Cartesian Navier-Stokes a 2D mesh of 2x2 elements with a length of 4 was used to solve the fabricated solution. The following divergence free fabricated solution was used

$$\begin{aligned}v_x(t, x, y) &= -t \cos x \sin y \\v_y(t, x, y) &= t \sin x \cos y \\p(x, y) &= xy\end{aligned}\tag{2.6.1}$$

To verify the axi-symmetric Navier-Stokes, a 2D axi-symmetric mesh of 4 elements in the axial direction with a radius of 0.5 and length of 20 was used. The following divergence free axi-symmetric fabricated solution was used

$$\begin{aligned}v_r(t, r, z) &= tr^4 \cos z \\v_z(t, r, z) &= -5tr^3 \sin z \\p(t, r, z) &= tr^3 z\end{aligned}\tag{2.6.2}$$

In both computations a time step of 0.01 was used and both simulations ran for 1000 steps. The L_2 norms for the Cartesian Navier-Stokes are shown in Figure 2.4 And for the Cylindrical Navier-Stokes are shown in Figure 2.5. From these plots it can be shown that our implemented spectral element solver performs adequately.

2.7 SEM vs FEM

For illustrating the advantages of the spectral convergence and usage of a structured mesh we want to compare our SEM solver with a standard FEM solver using linear tetrahedral elements. For a direct comparison we used the solution of the advection diffusion equation described in Chapter 3 which we calculated on a cylindrical mesh, with a length of 20 mm and a radius of 1 mm, created based on Chapter 2.5.2. A parabolic velocity field was prescribed with an average velocity of 10 mm/s and D was set to 0.05 mm²/s. For the spectral element mesh the cross-sectional structure was the same as Figure 2.2.20 and

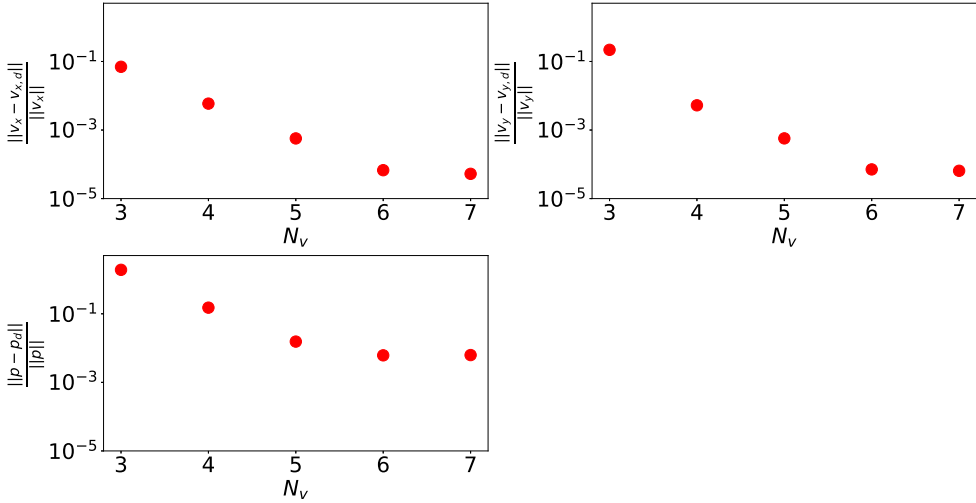


Figure 2.4: Verification results for the Cartesian Navier-Stokes using the fabricated solution from Equation 2.6.1. At each plot a normalized L_2 norm between the computed and actual solution is plotted against N_v .

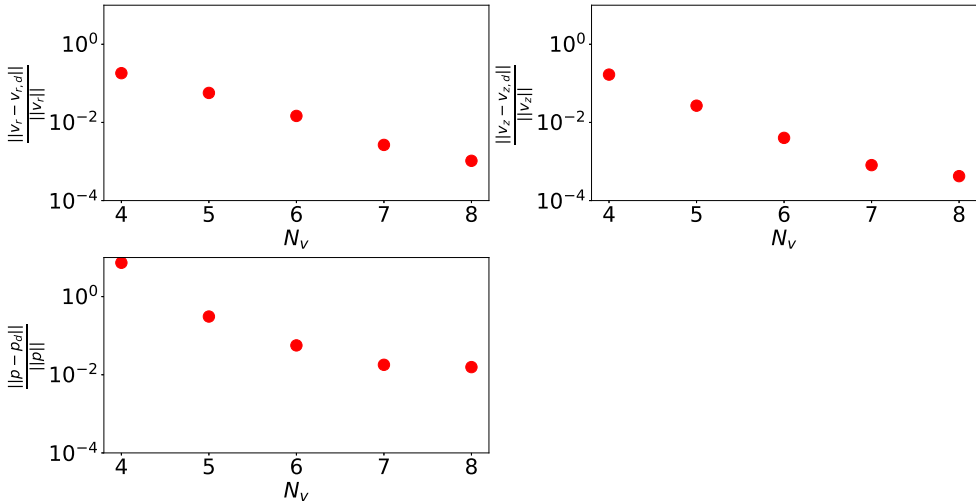


Figure 2.5: Verification results for the Cylindrical Navier-Stokes using the fabricated solution from Equation 2.6.2. At each plot a normalized L_2 norm between the computed and actual solution is plotted against N_v .

the number of axial element was set to 12. For the order of the polynomial this was varied from 1 to 5 in all directions. As for the FEM mesh the SEM surface mesh with a fifth order polynomial was used for creating a volume mesh. This was done by using Tetgen which uses Voronoi tessellation and restricted the volume of each element to be roughly 0.005, 0.002, 0.0007 and 0.0001 mm³. For computing the integration of FEM the Gauss quadrature was used from Section 2.2.3. The boundary condition at the inlet was set to $f(t) = t$ and the other boundaries consist of a no-flux boundary conditions. The entire solution started at zero and was simulated for 10,000 steps using a time step of 0.001 s. The normalized L_2 -norms between the analytical derived concentration C_a and SEM or FEM computed concentration C_d are shown in Figure 2.6 as function of the number of points inside the mesh N_n and the time the entire computation takes t_s . From these two plots it can be shown that for simulating contrast transport benefits from the usage of SEM compared to FEM. Additionally, the improvement in accuracy did not lead to an increase of computationally cost resulting in no reason to use FEM for these kind of problems. Furthermore, D was attempted to set lower than 0.05 mm²/s for a more advection dominated problem but the FEM solver was unable to converge even with the smallest element volume used, which was not the case for our SEM solver.

2.8 Conclusion

In this chapter, we successfully derived our SEM solver and verified it. In our comparison with the FEM solver we showed a large improvement in accuracy with the added ability to simulate complex advection dominated problems, which were previously not possible without stabilization methods. This provides many possibilities for utilising these detailed solutions for research. However, as SEM requires a structured description of your mesh many complex geometries will still need to rely on the standard FEM method.

References

- Canuto, C., Hussaini, M. Y., Quarteroni, A. M., & Zang, T. A. (1988). *Spectral methods in fluid dynamics* (1st). Springer-Verlag Berlin Heidelberg.
- Cyr, E. C., Shadid, J. N., & Tuminaro, R. S. (2012). Stabilization and scalable block preconditioning for the navier-stokes equations. *J. Comput. Physics*, 231, 345–363. <https://doi.org/10.1016/j.jcp.2011.09.001>

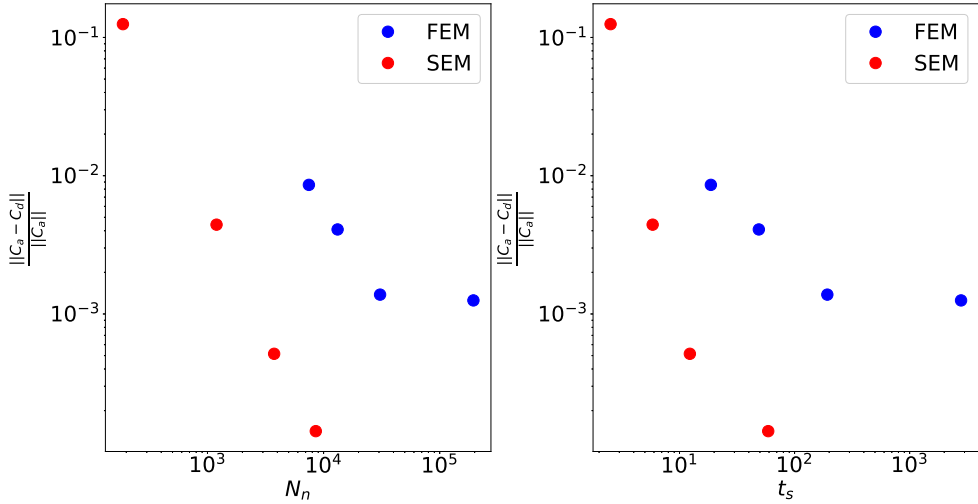


Figure 2.6: Figures show a comparison between SEM and FEM for a contrast transport problem in a cylindrical mesh, with a length of 20 mm and a radius of 1 mm, created based on Chapter 2.5.2. A parabolic velocity field was prescribed with a average velocity of 10 mm/s and D was set to $0.05 \text{ mm}^2/\text{s}$. For the spectral element mesh the cross-sectional structure is the same as Figure 2.2.20 and the number of axial element was set to 12. The order of the polynomial was varied from 1 to 5 in all directions. As for the FEM mesh the SEM surface mesh with a fifth order polynomial was used for creating a volume mesh. This was done by using Tetgen which uses Voronoi tessellation and restricted the volume of each element to be roughly 0.005, 0.002, 0.0007 and 0.0001 mm^3 . For computing the integration of FEM the Gauss quadrature was used from Section 2.2.3. The boundary condition at the inlet was set to $f(t) = t$ and the other boundaries consist of a no-flux boundary conditions. The entire solution started at zero and was simulated for 10000 steps using a time step of 0.001 s. A normalized L_2 -norm was then calculated between the semi-analytical solution C_a from chapter 3 and the simulated concentration C_d using both SEM (red dots) and FEM (blue dots). On the x-axis the number of points inside the mesh N_n and the time the entire computation takes t_s are set on respectively the left and right figure.

- De Santis, G. (2011). *Novel mesh generation method for accurate image-based computational modelling of blood vessels* (Doctoral dissertation). Ghent University.
- Jansen, K. E., Whiting, C. H., & Hulbert, G. M. (2000). A generalized-[alpha] method for integrating the filtered navier–stokes equations with a stabilized finite element method. *Methods Appl. Mech. Engrg.*, *190*(3-4), 305–319.

Image-based blood flow estimation using a semi-analytical solution to the advection diffusion equation in cylindrical domains

Abstract¹

We propose a semi-analytical solution for the advection diffusion equation in cylindrical domains, with an aim towards extracting blood flow rates from contrast variations in a coronary computed tomography angiography (CCTA) image. The solution proposed in this work, in contrast with existing methods, which only consider advection, incorporates both radial velocity variation and diffusion. By means of a Galerkin approach using Bessel functions a solution for a 3D concentration field at a single time point is obtained after a Laplace transformation. This semi-analytical solution forms the basis for a novel Advection Diffusion Flow Estimation (ADFE) method. ADFE is derived, validated through numerical spectral element method computations, and shown to exhibit improved accuracy against the state-of-the-art method for image-based blood flow extraction.

¹This chapter is based on: Bakker, L. M. M. L., Xiao, N., van de Ven, A. A. F., Schaap, M., van de Vosse, F. N., & Taylor, C. A. (2021). Image-based blood flow estimation using a semi-analytical solution to the advection-diffusion equation in cylindrical domains. *Journal of Fluid Mechanics*, 924, A18. <https://doi.org/10.1017/jfm.2021.596>

3.1 Introduction

A variety of transport phenomena can be characterized by solving the Advection Diffusion Equation (ADE) using numerical methods such as the finite element method, but these methods are computationally costly and do not necessarily provide insight into the underlying physics. To model transport in a particular problem domain, often there is a need for analytic forms that can be calculated rapidly and that can help elucidate the relationship between the advection and diffusion processes and associated parameters, see e.g. Gelderblom et al. (2011). Prior work in this area concerned with deriving general solutions to the ADE include the work of Kim (2020) and Pérez Guerrero et al. (2009). For a cylindrical shaped domain it is beneficial to consider the ADE in cylindrical coordinates and this specific problem requires special treatment in order to derive an analytical solution. Previous studies concerning the axisymmetric cylindrical domain include the work of Chen et al. (2011), in which constant velocities are assumed and a method for treating radial diffusion by using the Hankel transform is proposed. However, this method cannot be applied when a radially-varying velocity field is considered. Aris (1956) considers the 1D advection diffusion equation with added Taylor dispersion, assuming that enough time has elapsed such that radial diffusion can be neglected. The Taylor dispersion is included in the form of additional axial diffusion in the 1D advection diffusion equation for which an analytical solution can be obtained. This treatment of radial diffusion will likely be invalid when a time varying input concentration is present at the inlet. Namely, radial equilibrium in the concentration will not be reached when the change in concentration over time is significant.

In this paper we address the problem of characterizing the dynamics of contrast agent transport in contrast-enhanced medical imaging, specifically, coronary computed tomography angiography (CCTA), which is a diagnostic procedure for imaging the coronary arteries that provide the blood supply to the muscle of the heart. Advances in CCTA imaging technology have enabled the acquisition of high resolution images of the coronary arteries that can be used to quantitatively assess the severity of coronary artery disease - the primary manifestation of heart disease and the leading cause of death worldwide. CCTA is performed in conjunction with an intravenously-injected contrast agent, and the observed intensities in the CCTA image scale linearly with concentration of the contrast agent. Previous clinical studies have explored the utility of quantifying intensity gradients along the vessel path as a potentially useful indicator of physiological function that may be used to help

diagnose disease severity (Choi et al., 2012; Fujimoto et al., 2018; Steigner et al., 2015; Stuijzand et al., 2014). A recently-proposed method for indirectly quantifying coronary blood flow from the observed contrast variations along vessels in a CCTA image is known as Translumininal Attenuation Flow Encoding (TAFE) (Lardo et al., 2015). TAFE is based on the solution of the 1D advection equation, where neglecting radial diffusion was justified by the observation that the radial variation in contrast appears minimal (Eslami et al., 2015). This however is a flawed observation since the spatial resolution of a CCTA image is not sufficient to adequately reveal variations in concentration near the vessel wall. A clinical validation of TAFE was later performed by Bae et al. (2018), where perfusion CT was used to provide ground-truth per-vessel flow values. In that study, the authors proposed a modification to the original TAFE method by introducing an empirically-calibrated correction constant k for scaling the TAFE flow estimation. This correction constant was necessary to improve the correlation of the estimated flow with perfusion CT-based flow, which suggests that the original TAFE method does not always accurately estimate per-vessel flow. In order to obtain more accurate estimates, a higher-fidelity forward model is needed. Indeed, it is possible to use three-dimensional finite element methods to estimate the per-vessel flow by properly adjusting relevant parameters to match the observed contrast gradients. For simulating the contrast agent transport in the coronary circulation a highly refined mesh and multiple finite element solutions are needed for the blood flow estimation resulting in a computationally expensive method. Examples of these finite element-based estimation methods can be found in (Funke et al., 2019; Lassila et al., 2013). More recently, neural network methods such as physics-informed neural nets (Raissi et al., 2020), which produce estimates of solution fields that are constrained to follow physical relationships, have been proposed to study fluid and transport phenomena. These methods perform best when provided with highly resolved temporal and spatial data. However, CCTA data typically only contains a few high-spatial-resolution snapshot in time and this spatial data can contain significant levels of noise and artifacts. There is a need for a general solution to the ADE that can be obtained efficiently and that allows for the exploration of the advection and diffusion processes governing the dynamics of the contrast agent and their relationships to the underlying coronary blood flow.

In this paper, we propose an accurate semi-analytical solution to the advection diffusion equation for straight cylindrical vessels and axi-symmetric radially-varying velocities and concentration profiles. We use this approach to specifically highlight the potential deficiencies arising from certain simpli-

fying assumptions used by the TAFE method, namely neglecting the impact of radial velocity and diffusion, which we capture in our solution to varying degrees of fidelity. We verify the semi-analytical solution against a numerical solution obtained using a spectral element method. Finally, based on the semi-analytical solution, a new method for flow estimation from contrast gradients, Advection Diffusion Flow Estimation (ADFE), is derived and compared with the current TAFE methodology.

3.2 Methods

3.2.1 Problem formulation

The transport of a solute can be modeled using the ADE, and for the contrast material used in CCTA we assume that transport is passive. This is justified when the volume fraction of the solute, or concentration, is low enough. Passive implies that the solute does not impact the material properties of the carrying fluid (here, blood), that the velocities of the solute and the carrier are equal and that no mixing of the two fluids occur.

The concentration of the solute $C = C(\mathbf{x}, t)$ is described by

$$\frac{\partial C}{\partial t} + \mathbf{v} \cdot \nabla C = D \nabla^2 C, \quad (3.2.1)$$

where \mathbf{v} is the velocity and D the diffusion constant. We introduce cylindrical coordinates (r, ϕ, z) with r the radial, ϕ the circumferential and z the axial coordinate and further assume that both the velocity and concentration fields are axi-symmetric. The ADE (3.2.1) can then be written as

$$\frac{\partial C}{\partial t} + v_z \frac{\partial C}{\partial z} + v_r \frac{\partial C}{\partial r} = D \left(\frac{\partial^2 C}{\partial z^2} + \frac{1}{r} \frac{\partial C}{\partial r} + \frac{\partial^2 C}{\partial r^2} \right), \quad (3.2.2)$$

with the subscript indicating the corresponding component of \mathbf{v} . Finally, we assume a steady developed velocity field where $v_r = 0$ and $v_z(z, r, t) = v(r)$. This results in the following equation:

$$\frac{\partial C}{\partial t} + v(r) \frac{\partial C}{\partial z} = D \left(\frac{\partial^2 C}{\partial z^2} + \frac{1}{r} \frac{\partial C}{\partial r} + \frac{\partial^2 C}{\partial r^2} \right). \quad (3.2.3)$$

To make the formulation dimensionless we apply a scaling analysis using

$$t = T\hat{t}, \quad r = a\hat{r}, \quad z = L\hat{z}, \quad v(r) = V\hat{v}(\hat{r}), \quad C(t, z, r) = C_0\hat{C}(\hat{t}, \hat{z}, \hat{r}), \quad (3.2.4)$$

where T is the time delay between arrival contrast and reaching maximum concentration, V is the cross-sectional averaged velocity, a is the radius, L is a characteristic length in the axial direction and C_0 is a characteristic concentration. With the hat to indicate a dimensionless parameter, we derive:

$$St \frac{\partial \hat{C}}{\partial \hat{t}} + \hat{v}(\hat{r}) \frac{\partial \hat{C}}{\partial \hat{z}} = \frac{1}{Pe} \left(\frac{1}{\hat{r}} \frac{\partial \hat{C}}{\partial \hat{r}} + \frac{\partial^2 \hat{C}}{\partial \hat{r}^2} + \left(\frac{a}{L} \right)^2 \frac{\partial^2 \hat{C}}{\partial \hat{z}^2} \right), \quad (3.2.5)$$

where St is the Strouhal number $St = L/VT$ and Pe the radial Péclet number $Pe = Va^2/DL$. For completeness, an estimate for each of the characteristic physiological values during CCTA is shown in table 3.1. For slender cylindrical domains, such as the coronary arteries we consider here, $a \ll L$, and thus we can neglect the axial diffusion in (3.2.5), yielding

$$St \frac{\partial \hat{C}}{\partial \hat{t}} + \hat{v}(\hat{r}) \frac{\partial \hat{C}}{\partial \hat{z}} = \frac{1}{Pe} \left(\frac{1}{\hat{r}} \frac{\partial \hat{C}}{\partial \hat{r}} + \frac{\partial^2 \hat{C}}{\partial \hat{r}^2} \right). \quad (3.2.6)$$

To complete the problem formulation for $\hat{C}(\hat{r}, \hat{z}, \hat{t})$, the equation must be supplemented by the initial and boundary conditions. Initially, i.e. for $t \leq 0$, no solute is present in the fluid. At the inlet, $z = 0$, input solute concentration is prescribed by the product of a time-varying function $f(t)$ and a radial variation $g(r)$. At the wall, the radial flux of C is zero. This leads to the conditions

$$\hat{C}(\hat{r}, \hat{z}, 0) = 0, \quad \hat{C}(\hat{r}, 0, \hat{t}) = f(\hat{t})g(\hat{r}), \quad \frac{\partial \hat{C}}{\partial \hat{r}}(1, \hat{z}, \hat{t}) = 0. \quad (3.2.7)$$

The axial velocity is assumed to be fully-developed, implying that $v(r)$ has a parabolic profile. Choosing $V = Q/\pi a^2$, the averaged velocity, with Q the total flow rate, we obtain for the dimensionless velocity

$$\hat{v}(\hat{r}) = 2(1 - \hat{r}^2). \quad (3.2.8)$$

Unless otherwise noted, from here on we will always refer to the dimensionless formulation while omitting the hats.

3.2.2 Galerkin method

We first decompose $C(r; z; t)$ as a series of Bessel functions according to

$$C(r, z, t) = \sum_{m=1}^{\infty} C_m(z, t) J_0(\xi_m r), \quad \text{with } J_1(\xi_m) = 0, \quad (3.2.9)$$

| | | |
|-------|-------|--------------------|
| a | 1 | mm |
| V | 100 | mm/s |
| D | 0.001 | mm ² /s |
| T | 10 | s |
| L | 100 | mm |
| C_0 | 500 | HU |
| St | 0.1 | |
| Pe | 1000 | |

Table 3.1: Order estimates of the characteristic physiological values found in CCTA data.

where J_0 and J_1 are the zeroth and first-order Bessel function of the first kind with a parameter ξ_m to enforce the no-flux boundary condition. Substituting this equation into (3.2.6), we obtain

$$St \frac{\partial C_m}{\partial t} J_0(\xi_m r) + v(r) \frac{\partial C_m}{\partial z} J_0(\xi_m r) + \frac{\xi_m^2}{Pe} C_m J_0(\xi_m r) = 0, \quad (3.2.10)$$

and for the boundary conditions

$$C_m(z, 0) = 0, \quad C_m(0, t) = f(t)g_m, \quad (3.2.11)$$

with g_m resulting from separating $g(r)$ in the same way as C . We employ the Galerkin method by multiplying (3.2.10) with $J_0(\xi_n r)r$ and integrating the result with respect to r from $r = 0$ to 1. For practical calculations we truncate the infinite sum (3.2.9) at a finite number N , letting m run from 1 to N . Thus, we derive

$$St \frac{\partial C_n}{\partial t} + \sum_{m=1}^N Z_{nm} \frac{\partial C_m}{\partial z} + \frac{\xi_n^2}{Pe} C_n = 0, \quad 1 \leq n \leq N, \quad (3.2.12)$$

with

$$Z_{nm} = \frac{2}{J_0(\xi_n)^2} \int_0^1 v(r) J_0(\xi_m r) J_0(\xi_n r) r dr. \quad (3.2.13)$$

Substitution of $v(r) = 2(1 - r^2)$ results for Z_{nm} in

$$Z_{nm} = \begin{cases} 1 & \text{for } n = m = 1, \\ \frac{4}{3} & \text{for } n = m \neq 1, \\ -8 \frac{(\xi_m^2 + \xi_n^2) J_0(\xi_m)}{(\xi_m^2 - \xi_n^2)^2 J_0(\xi_n)} & \text{for } n \neq m. \end{cases} \quad (3.2.14)$$

3.2.3 Laplace transform

We proceed by using the Laplace transform $\mathcal{L}\{C_m(z, t); t, s\} = C_{mL}(z; s)$ in time to simplify (3.2.12) to

$$\sum_{m=1}^N Z_{nm} \frac{\partial C_{mL}}{\partial z} + \left(\frac{\xi_n^2}{Pe} + St s \right) C_{nL} = 0, \quad C_{nL}(0; s) = g_n f_L(s), \quad n \in (1, N), \quad (3.2.15)$$

with $f_L(s)$ the Laplace transform of $f(t)$. Introducing the N -vectors $\mathbf{C}_L = \{C_{nL}\}$ and $\mathbf{g} = \{g_n\}$, and the $N \times N$ -matrices $Z = \{Z_{nm}\}$ and $S = \text{Diag}\{\xi_n^2/Pe + St s\}$, a diagonal matrix, we can write (3.2.15) in matrix notation as

$$Z \frac{\partial \mathbf{C}_L}{\partial z} + S \mathbf{C}_L = 0. \quad (3.2.16)$$

The solution of the first-order ODE (3.2.16) is constructed with the eigenvectors and eigenvalues of $Z^{-1}S$, resulting in

$$\mathbf{C}_L(z, s) = \sum_{k=1}^N f_L(s) c_k \mathbf{A}_k(s) e^{-B_k(s)z}, \quad (3.2.17)$$

where \mathbf{A}_k is the k th eigenvector and B_k is the k th eigenvalue of $Z^{-1}S$. Moreover, the coefficients c_k are constants that can be determined by the boundary conditions

$$\mathbf{c} = A^{-1} \mathbf{g}, \quad (3.2.18)$$

where A is the $N \times N$ -matrix with columns \mathbf{A}_k , i.e. the eigensystem representation of $Z^{-1}S$. Following Abate and Whitt (2006), for the inverse Laplace transform we approximate \mathbf{C} by the finite linear combination of the transform values:

$$\mathbf{C}(z, t) \approx \sum_{k=1}^K \frac{\omega_k}{t} \mathbf{C}_L(z, \frac{\alpha_k}{t}), \quad (3.2.19)$$

with K the number of Laplace evaluations, while ω and α are defined by the fixed Euler summation method for non-negative real values from Abate and Whitt (2006). This approach speeds up the inversion compared to calculating the integral with a trapezoidal rule since fewer computations of \mathbf{C}_L are needed. Note that as stated by Abate et al. a high numerical precision is needed for the inverse Laplace transform.

3.2.4 ADFE method

For the ADFE method we utilise the solution described in sections 3.2.1-3.2.3 to solve the inverse problem of recovering the flow rate Q given an observed concentration field C_d at time of observation t_d . For this, ADFE only requires cross-sectional averaged concentration data $\bar{C}_d(z, t_d)$ along the vessel. Time-dependent concentration data at the inlet of the vessel needs to be available to construct $f(t)$. A schematic example of such data is shown in figure 3.1. The motivation for using the cross-sectional averaged concentration is due to the spatial resolution of CCTA; it is typically inadequate to measure the radial concentration distributions especially near the coronary artery walls. For straight vessels, we can calculate the semi-analytical \bar{C}_a as

$$\bar{C}_a(z, t) = 2 \int_0^1 C(r, z, t) r dr = C_1(z, t). \quad (3.2.20)$$

using the computed $f(t)$ and $t = t_d$. We define the least-squares error E_m between \bar{C}_d and \bar{C}_a as follows:

$$E_m = \|\bar{C}_d(z, t_d) - \bar{C}_a(z, t_d)\|_2, \quad (3.2.21)$$

and compute Q that minimizes E_m via an iterative minimization method. In this work the limited memory Broyden–Fletcher–Goldfarb–Shanno Bounded algorithm available in the SciPy ‘minimize’ function is used for the minimization of E_m (Jones et al., n.d.).

3.2.5 Spectral element solver

The reference solutions C_d used in this work are computed using 2D meshes on which (3.2.5) with the boundary conditions from (3.2.7) and velocity field from (3.2.8) is solved numerically by the spectral element method with high-order Legendre polynomials as the shape functions. The integration and interpolation points are chosen to be the same and are the Gauss Lobatto Legendre points in the z -direction and Gauss Radau Legendre points in the r -direction in order to avoid singularities at $r = 0$ (Bernardi et al., 1999; Shen et al., 2011). Only one high-order element is used in the radial direction to ensure connectivity. For time integration the generalized- α method is used from Jansen et al. (2000). The implementation is tested through benchmark problems to ensure proper computation of solutions.

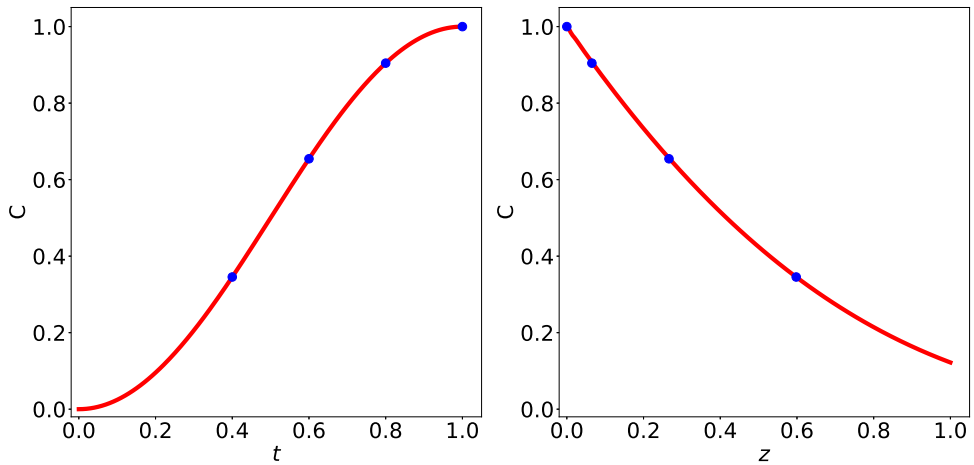


Figure 3.1: Schematic example of the input concentration function $f(t)$ (left) and snapshot of the cross-sectional averaged concentration at $t = 1$, i.e. $\bar{C}_a(z, 1)$, (right). The blue dots indicate specific concentration values evenly spaced over time and serve to show the non linear relationship between $f(t)$ and $\bar{C}_a(z, 1)$.

3.3 Results

To compare the semi-analytical solution with the reference solution computed with the spectral element solver described in Section 3.2.5, we create a data set of 48 simulations with Pe ranging from 1.67 to 1.6×10^5 and St values of $[0.025, 0.0375, 0.075, 0.15]$. These ranges are deliberately large in order to verify the solution over a large parameter space. For the boundary conditions we used a flat concentration profile $g(r) = 1$ and input function profile $f(t) = 0.5(1 - \cos(\pi t))$, which is the input function used in the original TAFE study by Lardo et al. (2015). For the computational results a time step of 0.0001 is used and the mesh consists of 200 elements with a radial polynomial order of 30 and axial order of 2. A mesh independence test was performed to confirm that these parameters were adequate for computing C_d .

3.3.1 Verification of the semi-analytical solution

We calculated the numerically-simulated concentration C_d and the semi-analytical concentration C_a on the same grid points of the spectral element mesh for the TAFE data set. To obtain C_a we used $M = 8$ for the computation of the inverse Laplace transform. An example solution is shown in figure 3.2, where it can be seen that near the wall a high concentration gradient appears that changes with t and z . The relative error is defined as

$E = \|C_d - C_a\|_2 / \|C_d\|_2$. figure 3.3 shows E as function of Pe for selected values of N and St . Here it is seen that for increasing Pe , more terms, N , in the Bessel series are needed to maintain an acceptable value of E , and in general as N increased, E decreased. The effect of St turns out to be rather small.

3.3.2 ADFE results

To benchmark the ADFE method described in section 3.2.4, we computed the velocity V_a by both the TAFE and ADFE method and compared them against the ground-truth velocity V_d used in the spectral element simulations. The velocity V_a computed by ADFE and TAFE as function of Pe is shown in figure 3.4. From this figure we conclude that ADFE more accurately predicts the velocity V_d compared to TAFE, and the accuracy of the prediction increases with increasing N . On the other hand, TAFE can greatly underestimate V_d . Since the lack of radial diffusion has a larger impact on the concentration field C for increasing Pe , TAFE's accuracy declines for increasing Pe .

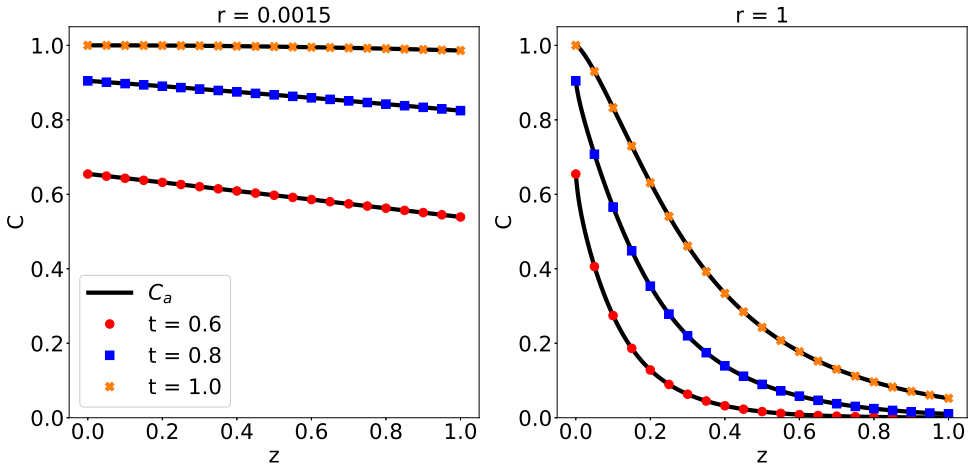
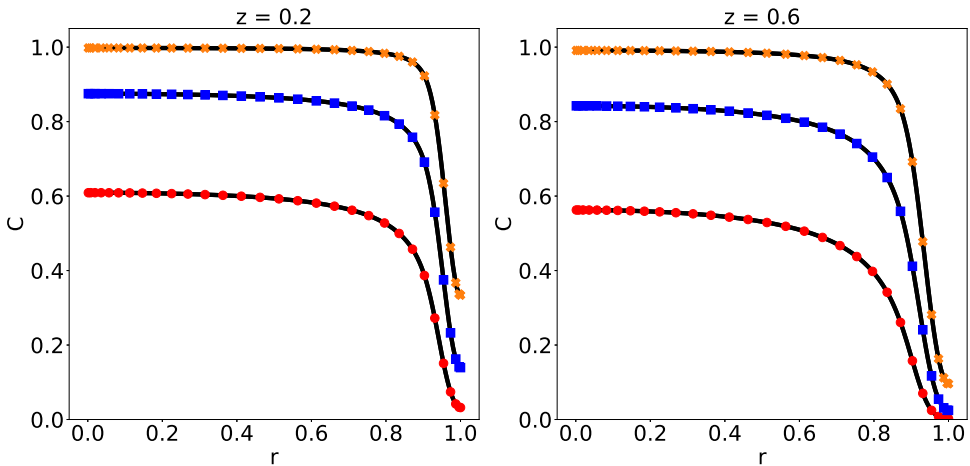
(a) Axial C for $r = 0.0015$ (left) and $r = 1$ (right)(b) radial C for $z = 0.2$ (left) and $z = 0.6$ (right)

Figure 3.2: Comparisons between the numerical solution C_d (markers) and the semi-analytical solution C_a (lines) for the concentration field with $Pe = 2667$ and $St = 0.15$ at three time points, $t = 0.6$ (orange crosses), $t = 0.8$ (blue squares) and $t = 1.0$ (red circles), using the concentration input function from the original TAFE study. Part (3.2a) shows concentration profiles for the numerical solution and the semi-analytical solution as functions of axial position at radii $r = 0.0015$ (left) and $r = 1$ (right), and part (3.2b) shows the radial concentration profiles at $z = 0.2$ (left) and $z = 0.6$ (right).

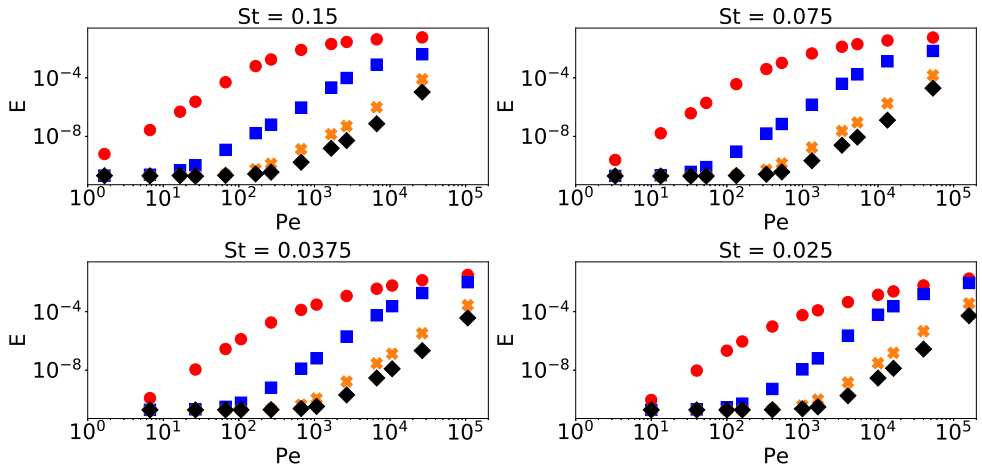


Figure 3.3: *log log* plots of the relative error $E = \|C_d - C_a\|_2 / \|C_d\|_2$ at $t = 1$ as a function of Pe with $N = 5$ (red circles), $N = 20$ (blue squares), $N = 50$ (orange crosses), $N = 70$ (black diamonds), $g(r) = 1$ and $f(t) = 0.5(1 - \cos(\pi t))$. Relative errors corresponding to four different St values are shown in the individual subplots.

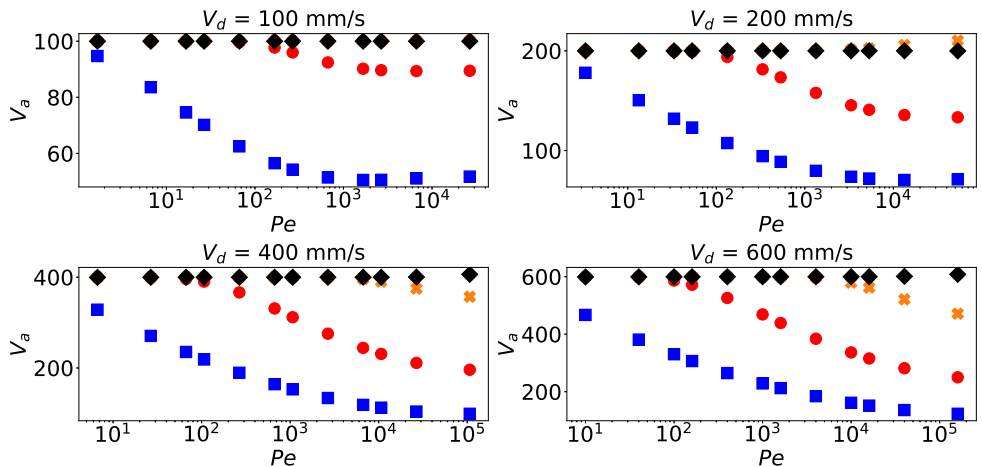


Figure 3.4: V_a computed by ADFE with $N = 5$ (red circles), $N = 20$ (orange crosses) and $N = 50$ (black diamonds) and TAFE (blue squares) as a function of Pe .

3.4 Discussion

We derived and verified a semi-analytical solution for the axi-symmetric advection diffusion equation. This solution was compared against numerical solutions from a spectral element method. The evaluation data set consisted of a wide range of values for Pe and St . We conclude that, provided that N , the number of terms in the series expansion, is sufficiently large, the semi-analytical solution accurately matches the numerical solutions. We showed that with increasing Pe , a larger N is needed to maintain a low error against the numerical solution, which suggests that resolving the radial variation in C becomes more important when Pe is large. The change in the error against the numerical solution when holding N constant was less when varying St compared to varying Pe . This suggests that for a coronary tree where the flow is divided after each bifurcation, an adequate value of N could be estimated based only on the geometry and on the properties of the contrast agent.

The semi-analytical solution forms the basis of the ADFE method, which allows for the estimation of the underlying flow rate, Q , based on the observed concentration field, \bar{C}_d at a fixed time t_d . The estimated Q from ADFE was compared with that from the TAFE method, where the latter does not consider any form of diffusion. This comparison showed that ADFE estimates Q more accurately than TAFE for a wide range of Pe , highlighting the importance of representing the effects of radial variations in the concentration and radial diffusion.

In order to apply this solution in a setting with real CCTA images, we note that the current method does not account for some important phenomena. In reality, the velocity field \mathbf{v} is pulsatile and is developing near the entrance of the coronary circulation. The current method can be modified for different steady or pulsatile developed \mathbf{v} by updating Z . However for a non-developed flow, v_r would not be zero and both v_r and v_z would depend on z and t . Thus it would be necessary to quantify the error due to assuming a developed \mathbf{v} in the semi-analytical solution. Furthermore, the coronary vessels are typically not perfectly straight cylindrical vessels and are often slightly tapered, curved, and with non-circular cross-sections. Additionally, the vessels have distensible walls and deform and translate due to the beating myocardium. While it is difficult to account for the combined impact of these effects, it is possible to estimate the impact of radius variations in the vessel on the prediction accuracy of ADFE compared with the straight cylinder setting: it can be derived that perturbation to the ADFE prediction from radius variation scales with ξ_n , having a larger impact on C_n for increasing n . From the structure of

Z it can be deduced that the dependency of C_1 on C_n decreases for increasing n , indicating that with large Pe , the contribution of the ξ_n^2/Pe term to C_1 is limited. This implies that even without precise knowledge of Pe and the variations in the vessel radius, we may still accurately predict \bar{C}_d by estimating St . Moreover, real coronary arteries contain bifurcations and stenoses, which may introduce sudden changes in the concentration field either by suddenly splitting the concentration field beyond a bifurcation or by radially increasing or decreasing the concentrations when passing a stenosis. Instead of applying the semi-analytical solution over the entire vessel, one can use the solution in segments between bifurcations or stenoses. However, at the start of each segment a significant jump in concentration or change in axial gradient compared to that in the proximal vessel can occur. This effect should be incorporated in the radial variation $g(r)$ prescribed at the inlet to ensure an accurate ADFE method. Future work should investigate how this can be performed correctly. All the segments should be combined such that conservation of mass of both the flow and concentration field is ensured.

Future work aims at quantifying the impact of the described limitations on the performance of the ADFE method. It needs to be ensured that the extracted cross-sectional averaged CCTA intensities correlate well with the contrast agent concentration. Here, a linear relationship between the intensity and concentration of the contrast agent is used. However, the CCTA image modality causes blurring, noise and additionally artifact which can lead to non-linearities. Bae et al. (2018) stated that the underestimation of TAFE was due to these imaging artifacts. However, the amount of underestimation is in the same order of what was found in our results. We therefore expect that the additional accuracy of ADFE will still be seen in clinical CCTA data when compared to TAFE.

3.5 Conclusion

In this paper a semi-analytical solution describing the transport of solute through a cylindrical shaped domain was successfully derived and validated. Based on this solution, a novel method ADFE, was developed. It presents an inverse solution for the flow rate based on snapshots of the concentration field in a cylindrical domain. A nearly perfect correspondence between this semi-analytic solution and a numerical spectral element method solution was found. Moreover, the ADFE solution was benchmarked against the existing TAFE method. The comparison demonstrated that ADFE has improved accuracy compared with the TAFE method for extracting flow rates from

contrast gradients.

Declaration of Interests

The authors report no conflict of interest.

References

- Abate, J., & Whitt, W. (2006). A unified framework for numerically inverting laplace transforms. *INFORMS Journal on Computing*, 18(4), 408–421.
- Aris, R. (1956). On the dispersion of a solute in a fluid flowing through a tube. *Proc. R. Soc. Lond. A*, 235(1200), 65–77.
- Bae, Y. G., Hwang, S. T., Han, H., Kim, S. M., Kim, H. Y., Park, I., Lee, J. M., Moon, Y. J., & Choi, J. H. (2018). Non-invasive coronary physiology based on computational analysis of intracoronary transluminal attenuation gradient. *Sci Rep.*, 8(1), 4692. <https://doi.org/10.1038/s41598-018-23134-7>
- Bakker, L. M. M. L., Xiao, N., van de Ven, A. A. F., Schaap, M., van de Vosse, F. N., & Taylor, C. A. (2021). Image-based blood flow estimation using a semi-analytical solution to the advection-diffusion equation in cylindrical domains. *Journal of Fluid Mechanics*, 924, A18. <https://doi.org/10.1017/jfm.2021.596>
- Bernardi, C., Dauge, M., Maday, Y., & Azaiez, M. (1999). *Spectral methods for axisymmetric domains*. Elsevier.
- Chen, J. S., Chen, J. T., Liu, C. W., Liang, C. P., & Lin, C. W. (2011). Exact analytical solutions for two-dimensional advection–dispersion equation in cylindrical coordinates subject to third-type inlet boundary condition. *Advances in Water Resources*, 34(3), 365–374.
- Choi, J. H., Koo, B. K., Yoon, Y. E., Min, J. K., Song, Y. B., Hahn, J. Y., Choi, S. H., Gwon, H. C., & Choe, Y. H. (2012). Diagnostic performance of intracoronary gradient-based methods by coronary computed tomography angiography for the evaluation of physiologically significant coronary artery stenoses: A validation study with fractional flow reserve. *Eur Heart J Cardiovasc Imaging*, 13(12), 1001–1007. <https://doi.org/10.1093/ehjci/jes130>
- Eslami, P., Seo, J. H., Rahsepar, A. A., Richard, A. G., Lardo, A. C., & Mittal, R. (2015). Computational study of computed tomography contrast gradients in models of stenosed coronary arteries. *J Biomech Eng.*, 137(9). <https://doi.org/10.1115/1.4030891>
- Fujimoto, S., Giannopoulos, A. A., Kumamaru, K. K., Matsumori, R., Tang, A., Kato, E., Kawaguchi, Y., Takamura, K., Miyauchi, K., Daida, H., Rybicki, F. J., & Mitsouras, D. (2018). The transluminal attenuation gradient in coronary ct

- angiography for the detection of hemodynamically significant disease: Can all arteries be treated equally? *Br J Radiol.*, 91(1087). <https://doi.org/10.1259/bjr.20180043>
- Funke, S. W., Nordaas, M., Evju, Ø., Alnæs, M. S., & Mardal, K. A. (2019). Variational data assimilation for transient blood flow simulations: Cerebral aneurysms as an illustrative example. *International Journal for Numerical Methods in Biomedical Engineering*, 35(1), e3152.
- Gelderblom, H., van der Horst, A., Haartsen, J. R., Rutten, M. C. M., van de Ven, A. A. F., & van de Vosse, F. N. (2011). Analytical and experimental characterization of a miniature calorimetric sensor in a pulsatile flow. *Journal of Fluid Mechanics*, 666, 428–444. <https://doi.org/10.1017/S0022112010004234>
- Jansen, K. E., Whiting, C. H., & Hulbert, G. M. (2000). A generalized-[alpha] method for integrating the filtered navier–stokes equations with a stabilized finite element method. *Methods Appl. Mech. Engrg.*, 190(3-4), 305–319.
- Jones, E., Travis, O., Peterson, P., et al. (n.d.). SciPy: Open source scientific tools for Python. <http://www.scipy.org/>
- Kim, A. S. (2020). Complete analytic solutions for convection-diffusion-reaction-source equations without using an inverse laplace transform. [PMID: 32415163]. *Scientific Reports*, 10(1), 8040. <https://doi.org/10.1038/s41598-020-63982-w>
- Lardo, A. C., Rahsepar, A. A., Seo, J. H., Eslami, P., Korley, F., Kishi, S., Abd, T., Mittal, R., & George, R. T. (2015). Estimating coronary blood flow using ct transluminal attenuation flow encoding: Formulation, preclinical validation, and clinical feasibility. *J Cardiovasc Comput Tomogr.*, 9(6), 559–566. <https://doi.org/10.1016/j.jcct.2015.03.018>
- Lassila, T., Manzoni, A., Quarteroni, A., & Rozza, G. (2013). A reduced computational and geometrical framework for inverse problems in hemodynamics. *International journal for numerical methods in biomedical engineering*, 29(7), 741–76.
- Pérez Guerrero, J. S., Pimentel, L. C. G., Skaggs, T. H., & van Genuchten, M. Th. (2009). Analytical solution of the advection–diffusion transport equation using a change-of-variable and integral transform technique. *International Journal of Heat and Mass Transfer*, 52(13), 3297–3304. <https://doi.org/https://doi.org/10.1016/j.ijheatmasstransfer.2009.02.002>
- Raissi, M., Yazdani, A., & Karniadakis, G. E. (2020). Hidden fluid mechanics: Learning velocity and pressure fields from flow visualizations. *Science*, 367(6481), 1026–1030.
- Shen, J., Tang, T., & Wang, L. L. (2011). *Spectral methods: Algorithms, analysis and applications* (1st). Springer Publishing Company, Incorporated.

- Steigner, M. L., Mitsouras, D., Whitmore, A. G., Otero, H. J., Wang, C., Buckley, O., Levit, N. A., Hussain, A. Z., Cai, T., Mather, R. T., Smedby, O., DiCarli, M. F., & Rybicki, F. J. (2015). Iodinated contrast opacification gradients in normal coronary arteries imaged with prospectively ecg-gated single heart beat 320-detector row computed tomographys. *Circ Imaging*, *137*(9), 179–186. <https://doi.org/10.1161/CIRCIMAGING.109.854307>
- Stuijzand, W. J., Danad, I., Raijmakers, P. G., Marcu, C. B., Heymans, M. W., van Kuijk, C. C., van Rossum, A. C., Nieman, K., Min, J. K., Leipsic, J., van Royen, N., & Knaapen, P. (2014). Additional value of transluminal attenuation gradient in ct angiography to predict hemodynamic significance of coronary artery stenosis. *JACC Cardiovasc Imaging*, *7*(4), 374–386. <https://doi.org/10.1016/j.jcmg.2013.12.013>

In-silico validation of the advection diffusion flow estimation method using computational patient specific coronary tree phantoms

Abstract¹

Coronary computed tomography angiography (CCTA) does not allow the quantification of reduced blood flow due to coronary artery disease (CAD). In response, numerical methods based on the CCTA image have been developed to compute coronary blood flow and assess the impact of disease. However to compute blood flow in the coronary arteries, numerical methods require specification of boundary conditions that are difficult to estimate accurately in a patient-specific manner. We describe herein a new non-invasive flow estimation method, called Advection Diffusion Flow Estimation (ADFE), to compute coronary artery flow from CCTA to use as boundary conditions for numerical models of coronary blood flow. ADFE uses image contrast variation along the tree-like structure to estimate flow in each vessel. For validating this method we used patient specific software phantoms on which the transport of contrast was simulated. This controlled validation setting enables a direct comparison between estimated flow and actual flow and a

¹This chapter is based on: Bakker, L. M. M. L., Xiao, N., Lynch, S., van de Ven, A. A. F., Updegrove, A., Schaap, M., Buls, N., de Mey, J., van de Vosse, F. N., & Taylor, C. A. (2022). Preclinical validation of the advection diffusion flow estimation method using computational patient specific coronary tree phantoms [Under review]. *International Journal for Numerical Methods in Biomedical Engineering*

detailed investigation of factors affecting accuracy. A total of 10 CCTA image data sets were processed to extract all necessary information for simulating contrast transport. A spectral element method solver was used for computing the ground truth simulations with high accuracy. On this data set, the ADFE method showed a high correlation coefficient of 0.998 between estimated flow and the ground truth flow together with an average relative error of only 1%. Comparing the ADFE method with the best method currently available (TAFE) for image-based blood flow estimation, which showed a correlation coefficient of 0.752 and average error of 20%, it can be concluded that the ADFE method has the potential to significantly improve the quantification of coronary artery blood flow derived from contrast gradients in CCTA images.

4.1 Introduction

Coronary computed tomography angiography (CCTA) is conducted by injecting an intravenous iodine based contrast material into the bloodstream to highlight the boundary of the coronary arteries and can be used to anatomically assess the severity of obstructive atherosclerotic plaques, i.e. stenoses. CCTA was recently given a Class 1 recommendation with level of evidence of A for patients with stable and acute chest pain in the 2021 American College of Cardiology / American Heart Association guidelines (Gulati et al., 2021). However, CCTA does not directly provide information about hemodynamics such as flow or pressure loss across the stenosis, which are important functional indicators of Coronary Artery Disease (CAD). An invasive metric that has become the gold standard for evaluating the severity of CAD is Fractional Flow Reserve (FFR), which is calculated as the ratio between the pressure distal to the stenosis and the reference aortic pressure (Pijls & Sels, 2012). FFR has been shown to improve patient outcomes, when used to decide whether or not surgical intervention is performed (Pijls et al., 2010). FFR requires fluoroscopy guided invasive catheterization and the insertion of a pressure wire to a location in the vessel distal to the lesion.

Computational fluid models based on CCTA images are now used in routine clinical practice to non-invasively approximate FFR. The non-invasive analogue of FFR derived from computational fluid dynamics and CCTA images is called FFR_{CT} (Taylor et al., 2013). In order to calculate FFR_{CT} , the coronary geometry is extracted from the CCTA image and a finite element method is used to solve the equations of fluid flow. The accuracy of this solution depends not only on the spatial resolution and correct segmentation of the coronary vessel lumen but also on the boundary conditions that control the

hemodynamic flow rates through each vessel. While geometrical parameters such as coronary artery diameter and myocardial volume can be readily extracted from the CCTA image, boundary conditions are difficult to estimate due to complex, patient-specific physiological conditions. While FFR_{CT} calculated using boundary conditions derived from anatomical information has demonstrated high diagnostic accuracy when compared to FFR (Taylor et al., 2013), these methods do not leverage the functional information that is implicitly embedded in the CCTA image itself. Recently, there has been growing interest in inferring coronary flows or assessing stenosis severity by analyzing the contrast intensity gradients along the coronary vessels (Bae et al., 2018; Choi et al., 2012; Eslami et al., 2022; Fujimoto et al., 2018; Lardo et al., 2015; Park et al., 2016; Steigner et al., 2015; Stuijzand et al., 2014; Wong et al., 2013). These techniques have the potential to further improve the estimation of boundary conditions and thereby increase the diagnostic accuracy of FFR_{CT} .

Within the aorta, a rise and decay of the concentration of intravenously-injected contrast can be indirectly measured via multiple CT acquisitions over time. This rise and fall describes the arterial input function (AIF), which is the concentration of the contrast at the level of the aorta over time. The contrast material is transported by the coronary blood flow (CBF) into the coronary vessels. When the CCTA image is acquired before the peak of the AIF, a linear function can be fitted to the intensities along the paths of the arteries. The slope of this linear function is called the Transluminal Attenuation Gradient (TAG) and is inversely correlated to the CBF within the same artery: a higher slope relates to a lower flow and vice versa. (Choi et al., 2012; Park et al., 2016; Steigner et al., 2015). Computation of TAG is facilitated by the advent of 256 and 320 row detector CT scanners, such as the Toshiba Aquilion One or GE Revolution, scanners that can image the full heart in a single cardiac cycle ensuring that the error due to sampling over multiple cardiac cycles can be avoided. In recent work, TAG was computed in healthy subjects and patients with CAD (Bae et al., 2018; Choi et al., 2012; Fujimoto et al., 2018; Park et al., 2016; Steigner et al., 2015; Stuijzand et al., 2014) and was found to be relatively constant across cardiac phases in the left anterior descending (LAD). However, these differences in TAG were significant in the left circumflex (LCx) and right coronary artery (RCA). Moreover, TAG was found to be lower in the RCA -6.5 ± 4.1 HU/cm than in the LAD -13.7 ± 8.0 HU/cm or LCx -12.5 ± 7.8 HU/cm (Steigner et al., 2015). Park et al. (2016) used a phantom study to show that TAG may be affected by vessel tapering which is lower in the RCA compared to the LAD and LCx.

The relationship between TAG and CBF was derived by Eslami et al. (2015) by solving the advection diffusion equation. In this work, the effects of diffusion and Taylor dispersion were neglected. Eslami et al. (2015) also assumed that the vessel does not change much in cross-sectional area over the path length and that the AIF can be approximated by means of an analytical cosine function. Using these assumptions, they derived a correlation between TAG and CBF called Tomography Transluminal Attenuation Flow Encoding (TAFE) and found a reasonably good correlation between TAFE and CBF measurements using micro spheres on 9 canine hearts (Lardo et al., 2015). TAFE's accuracy on clinical data was validated by Bae et al. (2018), who also introduced the TAFE correlation coefficient k , derived using perfusion CT data, to compensate for the tendency of TAFE to underestimate flow. For the patient group having no occlusions TAFE showed good performance. However, the slope in the correlation lines between TAFE and measured flow in the diseased patient groups decreased with increasing stenosis severity (1.018 for 0% diameter stenosis, 0.832 for 1 - 49% diameter stenosis, 0.819 for 50 - 79% diameter stenosis and 0.541 for 70 - 99% diameter stenosis) (Bae et al., 2018).

There are multiple possible explanations for the difference in TAG between healthy and stenosed arteries. Our first hypothesis is that the intensity measured on the CCTA image is not always well correlated with the real concentration of the contrast material. This may be due to low-pass filtering of the measured attenuation in the CCTA reconstruction resulting in contrast blurring outside of the vessel and the partial volume effect. Another hypothesis is that there are dynamic effects caused by diffusion on the contrast concentration that cannot be explained by pure advection.

In previous work, we introduced the Advection Diffusion Flow Estimation (ADFE) method which is an improvement to TAFE in straight axi-symmetric vessels (Bakker et al., 2021). This improvement is the result of including radial diffusion compared to only advection in the TAFE method. In this paper we extend and validate the ADFE method for complex patient-specific coronary trees. This is done in a controlled setting, since the intensity measured on the CCTA image is not always well correlated with the real concentration of the contrast material. Under this controlled setting, we again illustrate the critical importance of fundamental diffusion phenomena captured by ADFE that is not directly accounted for in the TAFE methodology.

4.2 Methods

In order for ADFE to compute flow from a CCTA image, several steps are necessary. A schematic of the workflow is shown in Figure 4.1. This workflow starts from two image data sets obtained during CCTA; the so-called bolus tracking series and the CCTA image itself. The bolus tracking series is acquired before triggering the scanner to image the full 3D CCTA image and consists of single slice images containing the ascending and descending aorta. Its main purpose is tracking the contrast agent over time in order to correctly time the CCTA acquisition when the highest intensity in the coronary vessels is expected. This data set is not used for diagnostic purposes, but can be used for reconstructing the AIF. From the CCTA image, the coronary arteries are segmented and the cross-sectional average intensity from the coronary ostia to the visible outlets are computed. This cross-sectional averaged intensity over the path length representing the spatial data and the AIF representing the temporal data are then input to the ADFE method to estimate the CBF through each vessel.

The controlled workflow used in this paper is shown in the bottom half of Figure 4.1 with each component described below. Compared to the CCTA workflow, we replaced the CCTA image with patient-specific software phantoms to simulate the transport of the contrast agent. This removes the scanner specific effects on the measured contrast intensity and allows us to directly compare the estimated flow from ADFE with the flow prescribed in the simulation.

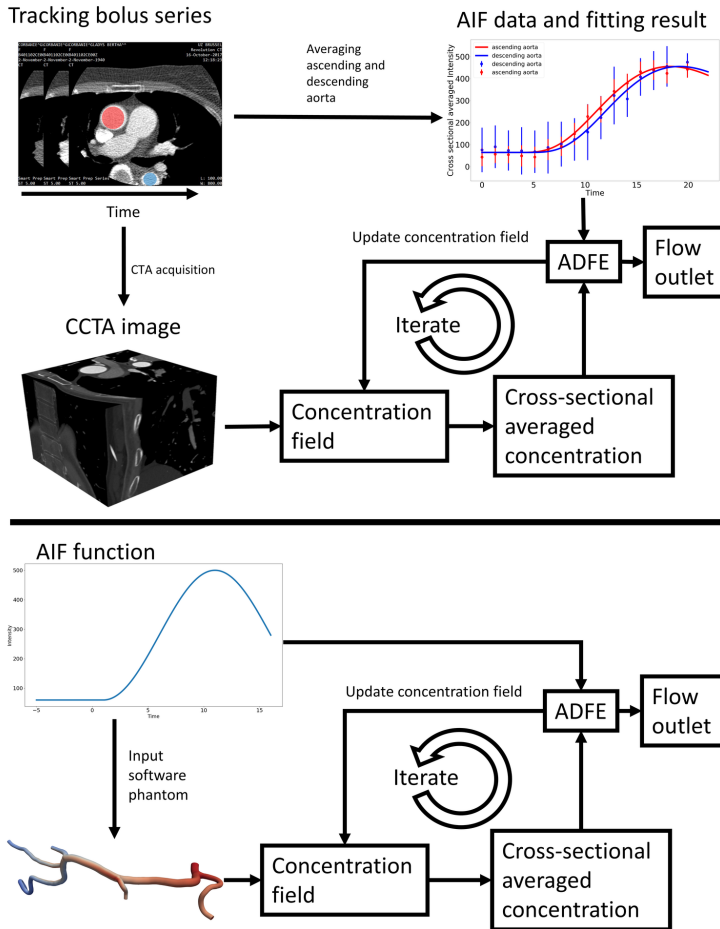


Figure 4.1: (top) Workflow of ADFE for CCTA images. The bolus tracking series is acquired before triggering the scanner to image the full 3D CCTA image. In each bolus tracking image, the ascending (red) and descending (blue) aorta are then segmented and the cross-sectional averaged intensity over time is computed and shown on the plot as dots with error bars indicating the mean and standard deviation of the intensities respectively. Using this sparse data, a continuous parametrized description of the AIF is fitted. This AIF function is then used as input for the ADFE method. Using the 3D CCTA image the coronary arteries are segmented to obtain the concentration field. The cross-sectional averaged intensity over the path length representing the spatial data and the AIF function representing the temporal data are then linked using the ADFE method which does so by estimating the CBF through each vessel. (bottom) Workflow of ADFE for the patient-specific software phantoms, which is used as a proof of concept for the ADFE method. We prescribe a synthetic AIF which serves as input to both the ADFE method and the software phantom. In the software phantom, contrast transport is simulated using this AIF and a three-dimensional velocity field.

4.2.1 Patient Collective

Patient data used in this study consists of anonymized CT data from 10 patients with suspected coronary artery disease (CAD) who received routine CCTA scans at the Universitair Ziekenhuis Brussel. The scans were retrospectively obtained from a previous study with approval from the local research ethics committee (BUN 143201524614) (Van Gompel et al., 2022). All scans were performed on a 256-slice CT scanner (Revolution CT, GE Healthcare).

4.2.2 AIF

In clinical practice, there are two commonly-used methods of timing the CCTA acquisition. The first method is using a test bolus, which is executed by injecting a small volume (mL) of contrast agent with similar injection parameters compared to the actual CCTA scan. The average intensity at the aorta after injection is then tracked and plotted over time. The time until the test bolus reaches maximum intensity has a strong correlation with the time the main bolus reaches a threshold of around 50, 100, 150 or 200 HU (Platt et al., 1999; van Hoe et al., 1995). This time to peak intensity can therefore be used to estimate the acquisition time of the CCTA. The second method is using a bolus tracking mentioned above; in this method, only the main bolus is injected and therefore does not require two scans. Again the average intensity at the aorta is tracked over time but this is done until a threshold value is reached (around 200 HU) and the scanner will then switch modes to acquire the CCTA.

We obtained bolus tracking data, from the patient data set described in Section 4.2.1. This data consists of images acquired at multiple time points at the same anatomical position so that both the ascending and descending aorta are shown on the images. Time stamps record when the images are acquired. The first time stamp after the start of the injection is set at the zero time point. An image is taken before the injection of the contrast agent is started and a region of interest (ROI) is placed on this image at the ascending aorta. Within this region the average intensity of the bolus is computed. At the start of the injection, a monitoring delay occurs before the bolus, after which a sequence of single image slices is acquired until the average intensity of the ROI reaches a threshold or a manual start is performed by the operator. The time between each image slice is called the monitor interscan delay. After either reaching the threshold intensity or a manual command to start the scan, the scanner switches modes and pauses until the designated time between the last slice and the actual CCTA scan, called the diagnostic delay, elapses.

To sample the intensities in the ascending and descending aorta, we first segment the aorta on the CCTA and AIF series by placing a seed on the aorta to start a threshold-based region growing algorithm. In certain situations we may also manually segment the aorta. The intensities within the aorta lumen are then extracted and averaged. We then fit an AIF on the combined averaged intensity over time of the ascending and descending aorta. The AIF is parameterized as

$$C(t_n) = C_{max}t_n^\alpha e^{\alpha(1-t_n)} + C_0, \text{ with } t_n = \frac{t - t_0}{t_m - t_0} \quad (4.2.1)$$

where C is the average intensity in HU, C_{max} is the maximal intensity, t is time, t_0 is the time the contrast enters the aorta, t_m is the time the maximal intensity is reached, t_n is the normalized time, $C_0 = C(t_0)$ and α is a parameter that determines the shape of the AIF. This formula is a simplified version of the gamma variate function (Madsen, 1992). In this form, the parameters have no dependencies on each other, thus improving the quality and robustness of the fit, which we performed using least-squares.

4.2.3 Patient specific software phantoms

Each patient case is processed by an automated program which segments and labels the myocardium, aorta, and visible coronary arteries from the CCTA image. The centerlines of the segmented aorta and coronary arteries are extracted from the image which includes at each centerline position the tangent-normal vector and the average radius of the corresponding cross-section. Each case includes the 3 major vessel trees namely the right coronary artery (RCA), left circumflex coronary artery (LCx), and left anterior descending coronary artery (LAD).

4.2.4 Spectral element solver

We used a spectral element solver to compute the contrast concentration fields for the software phantoms. This solver was validated and benchmarked in our previous study using 2D axisymmetric meshes (Bakker et al., 2021). For the volumetric meshes, structured cylindrical segments consisting of 12 elements are created at each centerline point. These 12 elements are placed in such a way that the singularity in the Jacobian caused by mapping a square to a circle is avoided. Additional elements and/or points for higher order elements in the axial direction can then be placed between centerline points. A cubic Hermite

spline is used to ensure a smooth transition between two centerline points and their respective tangents.

The Navier-Stokes equations are then solved, treating blood as an incompressible, isotropic, Newtonian fluid. The Neumann resistance boundary conditions at all outlets are based on the coronary geometry and a parabolic velocity profile is prescribed at the inlet of the vessel. The total input flow is scaled on the myocardial mass based on the concept of myocardial supply and demand (Taylor et al., 2013). Finally, a no-slip boundary condition is prescribed at the lumen wall. The time-stepping iterations are continued until the velocity field converges. After convergence, the velocity field is substituted into the advection diffusion equation. Using the AIF shown in Equation 4.2.1, which is used as the boundary condition on the vessel inlet and zero flux boundary conditions on all other surfaces, we then calculate the final solution of the concentration field. For post processing, the cross-sectional average value of the concentration field can be computed via numerical integration on the structured mesh.

4.2.5 TAFE

For the derivation of the TAFE method, a scaling analysis was used to justify the use of the 1D advection equation Eslami et al., 2015

$$\frac{\partial C}{\partial t} + \frac{Q}{A} \frac{\partial C}{\partial z} = 0, \quad (4.2.2)$$

with Q the flow, A the cross-sectional area and z the axial coordinate. Normalized TAG $G_{TA}^* = \frac{1}{C_{max}} G_{TA}$ is introduced by using the following simplification:

$$G_{TA}^* \approx \frac{1}{C_{max}} \frac{\partial C}{\partial z}. \quad (4.2.3)$$

G_{TA}^* is substituted into the 1D advection equation together with the 1D advection solution for the remaining $\frac{\partial C}{\partial t}$ term. Many derivations of Q exist in the TAFE literature each with a slightly different formula for Q based on the assumptions used. In this paper the clinically tested formulation was used Bae et al., 2018; Lardo et al., 2015:

$$Q = \frac{\hat{A}\pi}{t_m} \sqrt{\frac{L}{-4G_{TA}^*}}, \quad (4.2.4)$$

with \hat{A} the average area of the vessel and L the vessel length. This single vessel formula was used to compute flow through each outlet by computing

G_{TA}^* starting from the inlet of the coronary tree to each outlet. Computing flow through each vessel segment was done by combining these outlet TAFE flows by enforcing conservation of mass.

4.2.6 ADFE for coronary trees

The ADFE method was developed for straight axi-symmetric vessels and provides an accurate estimation of the ground truth flow. In the ADFE method a semi-analytical solution of the axi-symmetric advection diffusion is fitted on concentration data by adjusting the amount of flow through the vessel. This semi-analytical solution assumes a parabolic shaped velocity field together with a constant radius of the vessel segment Bakker et al., 2021. However, a coronary tree consists of multiple connected vessel segments and on each segment the radius can vary over the vessel path. 3D geometric features, such as curvature, are not explicitly accounted for in the ADFE methodology, and some vessel segments can be too short to reliably fit all parameters independently. This is evident when examining the least square error landscape as the parameters are related and a relative flat minimum exists; this phenomenon is less pronounced with increasing vessel segment length. These errors on individual segments can be largely avoided by linking the vessel segments via the conservation of mass. However, not all segments should have an equal contribution to the total minimization error as this may result in outliers for certain segments in the estimated flow. We use the following two step optimization methodology: First, starting with the semi-analytical solution for the 2D-axisymmetric advection solution described in Bakker et al. (2021), we describe the cross-sectional averaged concentration \bar{C} as function of the non-dimensional Peclet number $Pe = Qa^2/DV$ and Strouhal number $St = V/Qt_m$, with Q the flow, a the average radius, D the diffusion coefficient of the solute and V the accumulated volume in the axial direction, in both time t and axial coordinate z . Note that in this work we use the flow notation instead of cross-sectional averaged velocity as the latter is not constant over a radially varying vessel. All parameters can be measured from the geometry or AIF data except for D and Q . By estimating D we can use the ADFE method to estimate Q . This is done by iteratively minimizing the least-squares error E between the semi-analytical solution and the data by adjusting Q . Setting the boundary conditions in the semi-analytical solution is less trivial compared to the straight single vessels used in our previous work. With the exception of the input vessel, the time-shift t_s in the AIF and concentration input profile g at $z = 0$ is not known for the other vessel segments. Currently we address this by using the concentration profile at the end of the upstream vessel segment

and fitting t_s together with Q . Thus starting at the inlet and working downstream, the first step is applying the ADFE method for each vessel segment separately.

In the second and final optimization step we enforce the conservation of mass by setting the total flow of a vessel segment to be equal to the sum of the downstream vessel segments. This implies that we only need the flow at the outlet vessel segments to calculate the flow on all vessel segments. However, because of the axi-symmetric assumptions underlying the current ADFE method, an outlier in the flow estimation may occur at an outlet vessel segment. We address this issue by defining weights for each segment: for each i^{th} segment $w_i = (\log E_i)^2$ with E_i the error from the first step of the i^{th} segment. The total error is then the sum of all N segments in each tree:

$$E = \sum_{i=1}^N w_i E_i. \quad (4.2.5)$$

Note that we do not average E_i over the segments to ensure that larger segments contribute more to the total error. Furthermore, w_i is chosen such that the contribution of any single segment does not dominate the total error E , as shorter segments tend to have relatively smaller E_i . Similar to the first step we iteratively minimize E by adjusting each Q at the outlets and t_s at each segment, starting from the optimized values from step one. All minimizations of E are performed using the limited memory Broyden–Fletcher–Goldfarb–Shanno Bounded algorithm available in the SciPy ‘minimize’ function (Jones et al., n.d.).

4.3 Results

In order to validate the ADFE method for tree-like structures we used the anonymized data described in Section 4.2.1. The data for each patient included the images used to compute the AIF, as described in Section 4.2.2. The 3D CCTA image data was segmented and processed to extract the centerline data for creating the volumetric meshes (Section 4.2.3). The final data set was created by simulating the contrast transport and performing the post processing at a time point where a flattening in the gradient of the AIF occurred, or in other words, the moment the start of the plateau of maximum intensity is reached (Section 4.2.4). Our tree-based ADFE method and the TAFE method (Eslami et al., 2015) are applied to this set for validation and benchmarking. In total this data set consist of 366 vessel segments on which

the ADFE and TAFE flows could be compared to the ground truth flow. For reference the measured TAG was on average in the RCA -10.4 ± 5.0 HU/cm, LAD -8.8 ± 5.4 HU/cm and LCX -9.9 ± 7.2 HU/cm which is the same order as reported in literature Steigner et al., 2015.

4.3.1 AIF example

Two AIF examples from case 1 and 10 are both shown in Figure 4.2. The AIF from case 1 is a typical example containing a set of data points before arrival of the bolus and a few data points, usually two or three, when the bolus has arrived at the aorta. The last AIF data point was sampled from the actual CCTA image, which was acquired 8 seconds after the last tracking bolus image, at roughly the same location where the bolus tracking images were acquired

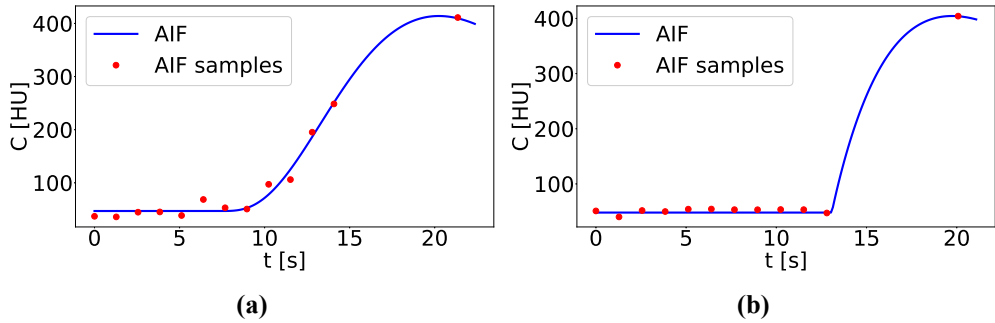


Figure 4.2: AIF examples from case 1 (left) and 10 (right). The red dots are sampled from the corresponding bolus tracking data set at the ascending aorta and the blue line is the corresponding fit of the AIF using Equation 4.2.1. The correspondence between this set and the AIF one is excellent.

4.3.2 ADFE vs TAFE

We compare ADFE and TAFE by examining the correlation and relative error between Q_m , the flow computed by either ADFE or TAFE, and Q_d , the input flow used to simulate C (Figures 4.3 and 4.4). ADFE has an average error of 1% and a high correlation coefficient $R = 0.998$. The benefit of using the two optimization steps in the tree-based ADFE method is that the relative error changes from -0.015 ± 0.154 after the first step to 0.014 ± 0.084 after the second step. The large improvement in the standard deviation of the relative error is caused by combining information from all vessel segments to mitigate the impact of segments where the single-segment ADFE method results in high error. These are typically segments that conform the least to the axi-symmetric

assumptions underlying ADFE or that are too short. TAFE produced a correlation coefficient of 0.752, with a relative error of -0.204 ± 0.662 . Q_m computed with ADFE is more accurate compared to TAFE even after the first ADFE optimization step which only uses the single-vessel ADFE method on each segment.

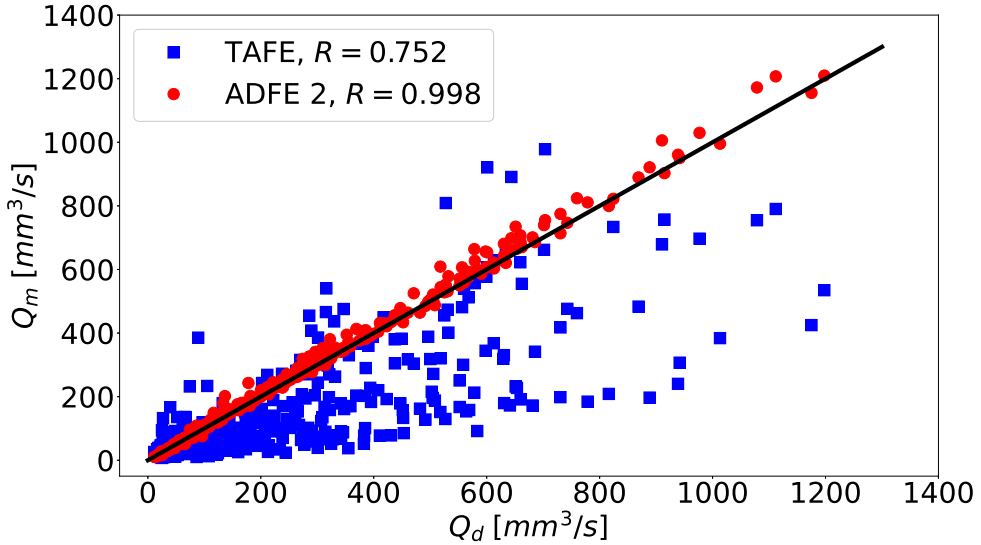


Figure 4.3: Correlation plot between Q_d and Q_m for ADFE (red dots) and TAFE (blue dots) of 366 vessel segments. The correlation coefficient R for each method is shown.

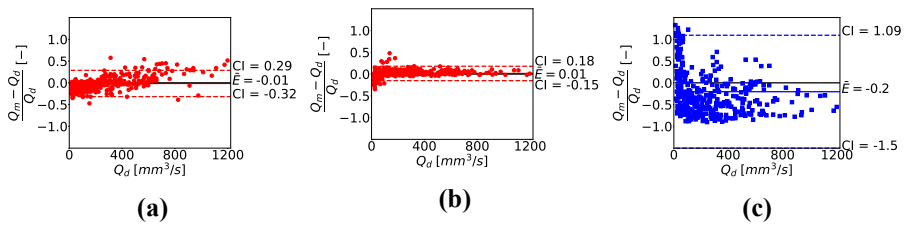


Figure 4.4: Relative difference plots for ADFE first optimization step (a), ADFE second optimization step (b) and the TAFE method (c) of 366 vessel segments. The difference is calculated as $\frac{Q_d - Q_m}{Q_d}$ and for each figure the mean difference (black line) and 95% confidence interval (dotted line) are shown.

4.3.3 Specific cases

Figure 4.5 shows the ADFE results from the LAD of case 2. A combination of low curvature and straight segments results in a velocity field which aligns

well with the assumptions underlying the ADFE method, contributing to high accuracy in the estimated flow. Figure 4.4b illustrates outliers, i.e. data points outside the confidence interval, where the accuracy of ADFE decreases. Two categories of segments exhibited a high relative error. The first category is short and relatively low-flow segments that have high curvature. An example of this is the LAD of case 5 shown in Figure 4.6. In Figure 4.6c four of these segments are labeled with a different severity of curvature. Specifically, segments 1 and 2 have the largest curvatures with a relative error in the flow estimation of -0.28 and -0.35 respectively. Segments 3 and 4 are straighter vessels comparatively and have lower relative flow errors of -0.11 for both segments. The second category consists of segments with relatively large flows together with large axial variations in radius and curvature. An example of this is the LCx of case 4 shown in Figure 4.7. From Figure 4.7a a good fit between the ADFE concentration solution and the intensity data can be seen. However, the estimated flow still resulted in an overestimation. The cause of the overestimation in this case is due to a non-parabolic velocity field especially in the proximal segments. Due to the high velocity and axially-varying geometry, the velocity field becomes more flat and the contrast transport is faster. An overestimation of the ADFE flow is expected due to the parabolic velocity profile assumption of the ADFE method.

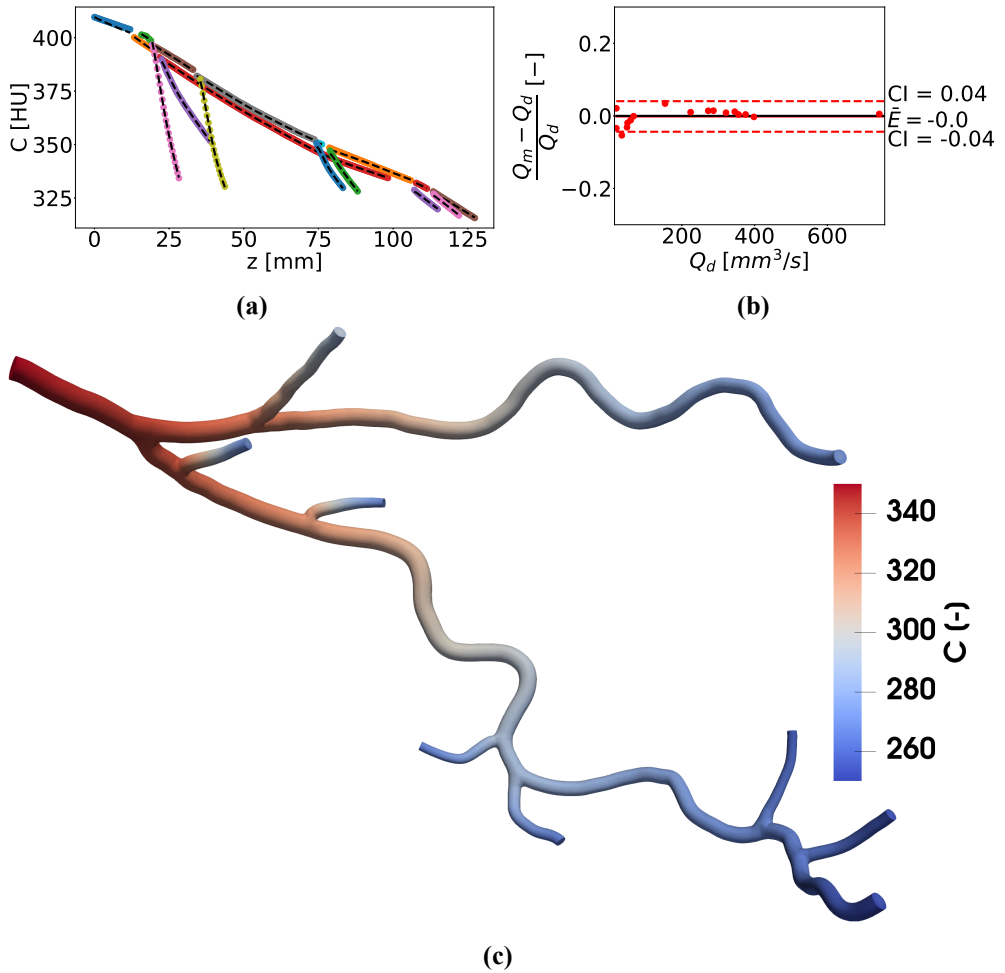


Figure 4.5: ADFE results for the LAD of case 2 with (a) the fit of the semi-analytical solution after the final optimization step for the LAD tree (black dashed lines) and cross-sectional averaged concentration (dotted lines with each color representing a different segment), (b) the relative difference plot for this case and (c) the concentration data present at the surface of the LAD mesh.

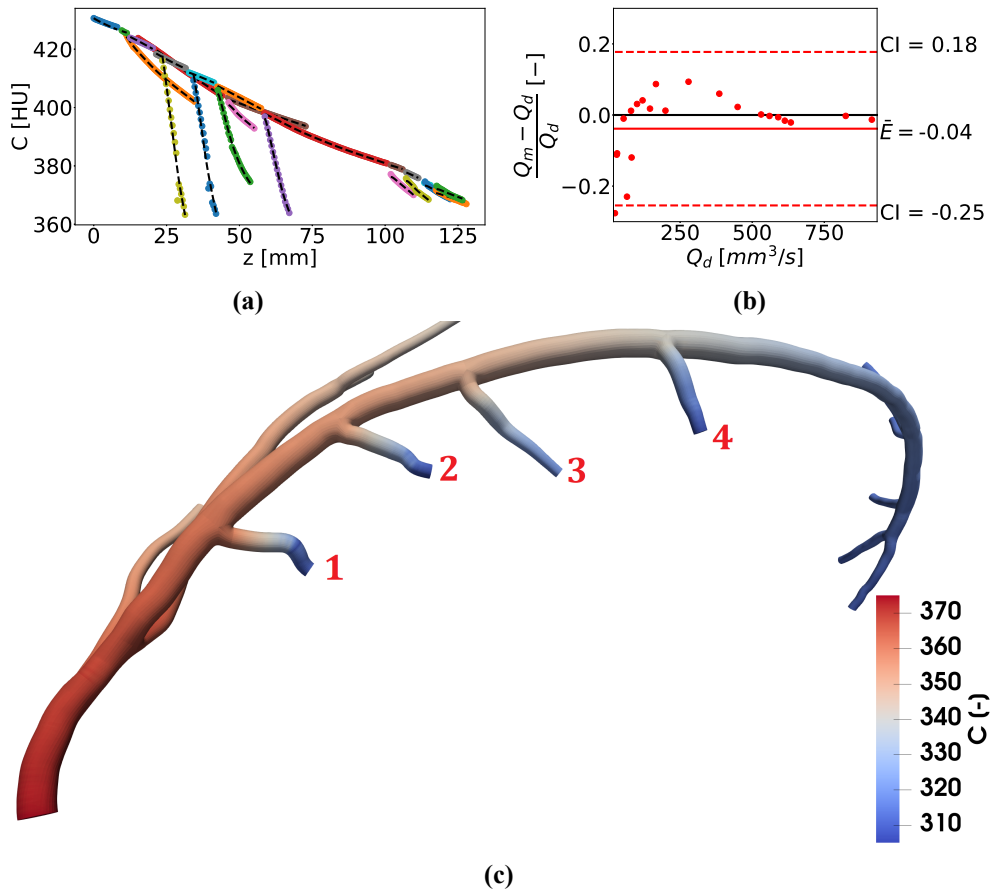


Figure 4.6: ADFE results for the LAD of case 5 with (a) the fit of the semi-analytical solution after the final optimization step for the LAD tree (black dashed lines) and cross-sectional averaged concentration (dotted lines with each color representing a different segment), (b) the relative difference plot for this case and (c) the concentration data present at the surface of the LAD mesh. Additionally four segments are labeled to illustrate the impact of vessel curvature.

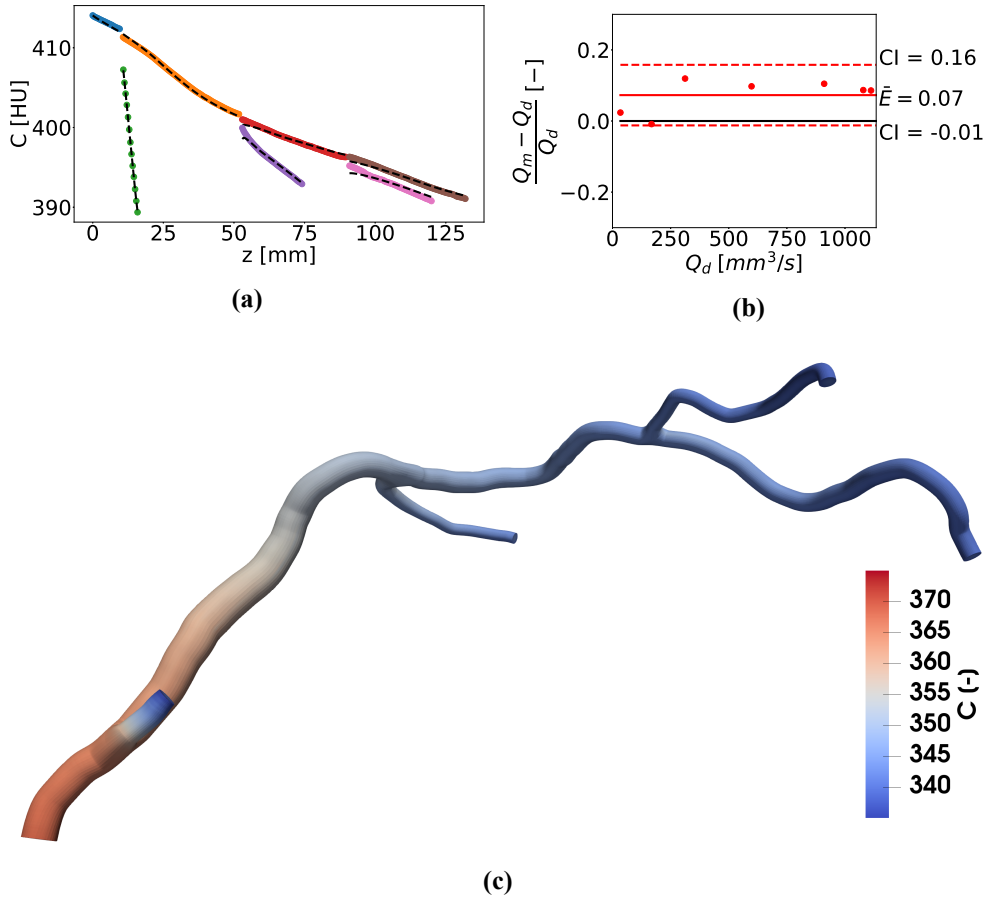


Figure 4.7: ADFE results for the LCx of case 4 with (a) the fit of the semi-analytical solution after the final step for the LAD tree (black dashed lines) and cross-sectional averaged concentration (dotted lines with each color representing a different segment), (b) the relative difference plot for this case and (c) the concentration data present at the surface of the LCx mesh.

4.4 Discussion

In this study, we successfully extended the ADFE method from simple axisymmetric vessels (Bakker et al., 2021) to coronary trees. We used patient-specific software phantoms which ensures a fully controlled setting compared to actual CCTA images. The flows estimated by ADFE resulted in a 1% average error compared to the ground-truth flows used in the contrast transport simulations. Central to the ADFE method is the fitting of a semi-analytical solution of the advection diffusion equation to the contrast intensity data, and the tree-based ADFE method relies on a sequence of two optimization steps described in Section 4.2.6 that leverages information from all of the vessel segments in the coronary tree. Overall, a small standard deviation (8%) in relative error was found in the 10 cases we investigated, which highlights the robustness of the ADFE method. The ADFE method is also fast and computationally inexpensive; the total computation time per case is 1-10 minutes on a single processing core depending on tree size and convergence criteria.

We have previously compared ADFE with TAFE in axi-symmetric vessels (Bakker et al., 2021), where we showed significant improvements in accuracy. In this study involving patient-specific coronary vessel trees, the 1% flow estimation error of ADFE was found to be a significant improvement compared to the 20% average error of TAFE. The major difference between ADFE and TAFE is the inclusion of radial transport phenomenon, i.e. the velocity profile and radial diffusion that is considered in the ADFE method. In a recent study involving TAFE, a correction for the radial velocity profile has been proposed in the form of a constant correction term (Eslami et al., 2022). The experimental CCTA setup in this study involved scanning a 3D printed vessel in which a contrast solution was pumped through using different flow rates. Similar to our results, underestimation of the TAFE flow estimate compared to the true flow was found. The correction term resulted in an accurate TAFE flow estimation but the correction is specific to the tested vessel geometry. Choosing a constant correction term would be insufficient for a more general data set as there is a non-linear relationship between the radial transport and the flow rate. Additionally, TAFE requires the CCTA acquisition to be before the AIF plateau to ensure a negative TAG can be measured. In the ADFE method a semi-analytical solution is fitted on the concentration which can be performed at every point in time. Although the greater concentration gradient when acquiring the CCTA before the plateau would improve the robustness of the ADFE fit, it can still be performed when the CCTA timing is off. Overall we showed that ADFE accurately estimates flow from simulated contrast data

extracted from multiple different patient specific coronary vessel trees.

We have identified two distinct situations for which the accuracy of ADFE may decrease. ADFE underestimates flow in small segments with high curvature bifurcating from a relative larger parent vessel. It is possible that this could be the result of numerical artifacts from using a zero flux boundary condition at the outlets. However, for these small segments, the absolute flow error in the individual segments is low compared to the total flow of the tree (less than 1%). The second category of outlier segments is where the velocity field significantly differs from the assumed parabolic profile. This is caused by a combination of significant axial variations in radius and a relatively high flow resulting in a flat velocity profile. In these cases, a significant overestimation of the flow may occur. It should also be noted that the coronary trees used in this research are without CAD, which are extreme situations, where this can occur. Special care should be taken when computing ADFE on vessels with CAD, with even excluding the diseased section from the ADFE fit

Before utilizing ADFE with real CCTA images, additional considerations are necessary. Ideally, fitting the AIF would require more complete temporally-resolved image data than is currently available in the investigated cases. Currently the timing images are only used for tracking the arrival of the bolus and timing the actual 3D CT scan. There is a large gap in timing data between the bolus tracking data set and the time of the CCTA scan, and this may result in non uniqueness of the AIF fit. By reducing the diagnostic delay and extending the bolus tracking, more points could be added on the AIF curve, thus increasing the reliability of the fitted AIF.

Compared to the axi-symmetric vessels in our previous study, realistic AIF data and patient specific geometries were used in the present study to validate the ADFE method for extracting flow from contrast gradients in CCTA images. However, compared to using intensity data from actual CCTA images, we still do not account for important phenomena related to the imaging process and the underlying physiology. The most important consideration with real CCTA images is determining an accurate correlation between the measured image intensity samples from the CCTA images and the actual contrast concentrations. The CCTA imaging process involves blurring, partial volume effects and the presence of imaging artifacts which affect the measured image intensity (HU). Blurring results in a lower measured cross-sectional averaged intensity. The partial volume effect also contributes to lower measured intensities as the intensities of voxels at the lumen boundary which are both inside and outside of the vessel will be averaged out. Correcting these effects is a necessary preprocessing step in utilizing ADFE or TAFE. In their CCTA phantom

study the authors of the TAFE method also investigated a correction function based on the area of each cross-section (Eslami et al., 2022). This was done by scanning a tapered vessel with a constant contrast concentration. Despite the constant concentration, a decreasing intensity along the vessel path was found due to imaging effects correlating with the cross-sectional area. A correction function was then fitted on the ratio between the true constant intensity and measured cross-sectional averaged intensity as a function of the area of each cross-section.

Additionally, the pulsatility in the contrast transport caused by the beating heart is not explicitly accounted for. As the contrast is injected intravenously the contrast is mixed inside the heart chambers and pumped into the aorta, producing oscillations in the AIF. The velocity field is also pulsatile and still developing at the entrance of the coronary circulation. Both phenomena could be accounted for by adjusting the semi-analytical solution that the ADFE method relies on; more details about this procedure can be found in Bakker et al. (2021).

4.5 Conclusion

We have demonstrated that a tree-based ADFE method can be used to estimate flows on a set of software phantoms based on patient specific geometries with realistic AIF data. This work represents a significant step toward a general and robust method for estimating blood flow from actual CCTA images.

Acknowledgement

The authors would like to acknowledge HeartFlow, Inc. for providing research funding and Prof. Rajat Mittal for providing insights into the implementation of the TAFE method.

Declaration of Interests

N. Xiao, S. Lynch, A. UpdePac, M. Schaap and C.A. Taylor are employees of HeartFlow, Inc.

References

- Bae, Y. G., Hwang, S. T., Han, H., Kim, S. M., Kim, H. Y., Park, I., Lee, J. M., Moon, Y. J., & Choi, J. H. (2018). Non-invasive coronary physiology based on computational analysis of intracoronary transluminal attenuation gradient. *Sci Rep.*, *8*(1), 4692. <https://doi.org/10.1038/s41598-018-23134-7>
- Bakker, L. M. M. L., Xiao, N., Lynch, S., van de Ven, A. A. F., Updegrove, A., Schaap, M., Buls, N., de Mey, J., van de Vosse, F. N., & Taylor, C. A. (2022). Pre-clinical validation of the advection diffusion flow estimation method using computational patient specific coronary tree phantoms [Under review]. *International Journal for Numerical Methods in Biomedical Engineering*.
- Bakker, L. M. M. L., Xiao, N., van de Ven, A. A. F., Schaap, M., van de Vosse, F. N., & Taylor, C. A. (2021). Image-based blood flow estimation using a semi-analytical solution to the advection-diffusion equation in cylindrical domains. *Journal of Fluid Mechanics*, *924*, A18. <https://doi.org/10.1017/jfm.2021.596>
- Choi, J. H., Koo, B. K., Yoon, Y. E., Min, J. K., Song, Y. B., Hahn, J. Y., Choi, S. H., Gwon, H. C., & Choe, Y. H. (2012). Diagnostic performance of intracoronary gradient-based methods by coronary computed tomography angiography for the evaluation of physiologically significant coronary artery stenoses: A validation study with fractional flow reserve. *Eur Heart J Cardiovasc Imaging*, *13*(12), 1001–1007. <https://doi.org/10.1093/ehjci/jes130>
- Eslami, P., Seo, J. H., Rahsepar, A. A., Richard, A. G., Lardo, A. C., & Mittal, R. (2015). Computational study of computed tomography contrast gradients in models of stenosed coronary arteries. *J Biomech Eng.*, *137*(9). <https://doi.org/10.1115/1.4030891>
- Eslami, P., Seo, J. H., Rahsepar, A. A., Shafique, A., Rollison, S. F., Lardo, A. C., Mittal, R., & Chen, M. Y. (2022). A noninvasive assessment of flow based on contrast dispersion in computed tomography angiography: A computational and experimental phantom study. *J Biomech Eng.*, *144*(9). <https://doi.org/10.1115/1.4053997>
- Fujimoto, S., Giannopoulos, A. A., Kumamaru, K. K., Matsumori, R., Tang, A., Kato, E., Kawaguchi, Y., Takamura, K., Miyauchi, K., Daida, H., Rybicki, F. J., & Mitsouras, D. (2018). The transluminal attenuation gradient in coronary ct angiography for the detection of hemodynamically significant disease: Can all arteries be treated equally? *Br J Radiol.*, *91*(1087). <https://doi.org/10.1259/bjr.20180043>
- Gulati, M., Levy, P. D., Mukherjee, D., Amsterdam, E., Bhatt, D. L., Birtcher, K. K., Blankstein, R., Boyd, J., Bullock-Palmer, R. P., Conejo, T., Diercks, D. B., Gentile, F., Greenwood, J. P., Hess, E. P., Hollenberg, S. M., Jaber, W. A., Jneid, H., Joglar, J. A., Morrow, D. A., ... Shaw, L. J. (2021). 2021 guideline for the evaluation and diagnosis of chest pain. *Journal of the American Col-*

- lege of Cardiology*, 78(22), e187–e285. <https://doi.org/10.1016/j.jacc.2021.07.053>
- Jones, E., Travis, O., Peterson, P., et al. (n.d.). SciPy: Open source scientific tools for Python. <http://www.scipy.org/>
- Lardo, A. C., Rahsepar, A. A., Seo, J. H., Eslami, P., Korley, F., Kishi, S., Abd, T., Mittal, R., & George, R. T. (2015). Estimating coronary blood flow using ct transluminal attenuation flow encoding: Formulation, preclinical validation, and clinical feasibility. *J Cardiovasc Comput Tomogr*, 9(6), 559–566. <https://doi.org/10.1016/j.jcct.2015.03.018>
- Madsen, M. T. (1992). A simplified formulation of the gamma variate function. *Phys. Med. Biol.*, 37(7), 1597–1600. <https://doi.org/10.1088/0031-9155/37/7/010>
- Park, E. A., Lee, W., Park, S. J., Kim, Y. K., & Hwang, H. Y. (2016). Influence of coronary artery diameter on intracoronary transluminal attenuation gradient during ct angiography. *JACC Cardiovasc Imaging*, 9(9), 1074–1083.
- Pijls, N. H., Fearon, W. F., Tonino, P. A., Siebert, U., Ikeno, F., Bornschein, B., van't Veer, M., Klauss, V., Manoharan, G., Engstrøm, T., Oldroyd, K. G., Ver Lee, P. N., MacCarthy, P. A., & De Bruyne, B. (2010). Fractional flow reserve versus angiography for guiding percutaneous coronary intervention in patients with multivessel coronary artery disease: 2-year follow-up of the fame (fractional flow reserve versus angiography for multivessel evaluation) study. *J Am Coll Cardiol.*, 56(3), 177–184. <https://doi.org/10.1016/j.jacc.2010.04.012>
- Pijls, N. H., & Sels, J. W. (2012). Functional measurement of coronary stenosis. *J Am Coll Cardiol.*, 59(12), 1045–1057. <https://doi.org/10.1016/j.jacc.2011.09.077>
- Platt, J., Reige, K., & Ellis, J. (1999). Aortic enhancement during abdominal ct angiography: Correlation with test injections, flow rates, and patient demographics. *AJR. American journal of roentgenology*, 172(1), 53–56. <https://doi.org/10.2214/ajr.172.1.9888738>
- Steigner, M. L., Mitsouras, D., Whitmore, A. G., Otero, H. J., Wang, C., Buckley, O., Levit, N. A., Hussain, A. Z., Cai, T., Mather, R. T., Smedby, O., DiCarli, M. F., & Rybicki, F. J. (2015). Iodinated contrast opacification gradients in normal coronary arteries imaged with prospectively ecg-gated single heart beat 320-detector row computed tomographys. *Circ Imaging*, 137(9), 179–186. <https://doi.org/10.1161/CIRCIMAGING.109.854307>
- Stuijzand, W. J., Danad, I., Raijmakers, P. G., Marcu, C. B., Heymans, M. W., van Kuijk, C. C., van Rossum, A. C., Nieman, K., Min, J. K., Leipsic, J., van Royen, N., & Knaapen, P. (2014). Additional value of transluminal attenuation gradient in ct angiography to predict hemodynamic significance of coronary artery stenosis. *JACC Cardiovasc Imaging*, 7(4), 374–386. <https://doi.org/10.1016/j.jcmg.2013.12.013>

- Taylor, C. A., Fonte, T. A., & Min, J. K. (2013). Computational fluid dynamics applied to cardiac computed tomography for noninvasive quantification of fractional flow reserve: Scientific basis. *J Am Coll Cardiol.*, *61*(22), 2233–2241. <https://doi.org/10.1016/j.jacc.2012.11.083>
- Van Gompel, G., Delombaerde, L., Zanca, F., Tanaka, K., Belsack, D., de Mey, J., & Buls, N. (2022). A patient- and acquisition-tailored injection approach for improving consistency of ct enhancement towards a target ct value in coronary ct angiography. *Journal of Applied Clinical Medical Physics*, e13867. <https://doi.org/https://doi.org/10.1002/acm2.13867>
- van Hoe, L., Marchal, G., Baert, A. L., Gryspeerdt, S., & Mertens, L. (1995). Determination of scan delay time in spiral ct-angiography: Utility of a test bolus injection. *Journal of computer assisted tomography*, *19*(2), 216–220. <https://doi.org/10.1097/00004728-199503000-00009>
- Wong, D. T., Ko, B. S., Cameron, J. D., Nerlekar, N., Leung, M. C., Malaiapan, Y., Crossett, M., Leong, D. P., Worthley, S. G., Troupis, J., Meredith, I. T., & Seneviratne, S. K. (2013). Transluminal attenuation gradient in coronary computed tomography angiography is a novel noninvasive approach to the identification of functionally significant coronary artery stenosis: A comparison with fractional flow reserve. *J Am Coll Cardiol.*, *61*(12), 1271–1279. <https://doi.org/10.1016/j.jacc.2012.12.029>

Verification before clinical validation ADFE

Abstract

The contrast intensity measured on coronary computed tomography angiography (CCTA) images contain imaging effects which results in a non-linear relationship between the measured and actual contrast concentration. This impairs the advection diffusion flow estimation (ADFE) workflow, described in Chapter 4, in accurately estimating coronary blood flow. In this study, we therefore propose a computed tomography (CT) correction function to be added to the ADFE method in order to improve accuracy in estimating coronary blood flow from clinical CCTA images. To verify this CT correction function, we used a controlled setting where we mimic CCTA-like effects on the patient specific software phantoms from Chapter 4 with a simple virtual CT (vCT) method. On this vCT data set, we compute flow using both ADFE and the best method currently available, called transluminal attenuation flow encoding (TAFE). These results show that adding the imaging effects caused an underestimation of the computed ADFE flow with a relative error between it and the ground truth flow decreasing from 1% to -16%. Although the accuracy decreased more for ADFE compared to TAFE, ADFE can still be considered an improvement over TAFE as it produces more consisted and accurate results. Furthermore, the verification made it possible to identify sections within ADFE to improve in order to reverse the reduced accuracy of ADFE due to imaging effects. By improving these sections, ADFE has the potential to provide an accurate estimation of coronary blood flow based on the CCTA image.

5.1 Introduction

Coronary computed tomography angiography (CCTA) is currently the first choice method for diagnosing coronary artery disease. Afterwards if a stenosis is visible on the CCTA image, fractional flow reserve (FFR) is then used for deciding if intervention is necessary. However, measuring FFR does already involve a minimal invasive procedure to place a pressure wire at the location of the stenosis. FFR_{CT} computed from CCTA images has therefore been developed to reduce the number of unnecessary invasive procedures by non-invasively calculating FFR using numerical methods (Taylor et al., 2013). These numerical methods require an accurate segmentation of the mesh from the CCTA image and flow boundary conditions in order to be accurate. Improvements to the segmentation of the coronary arteries or flow boundary conditions will, for that reason, possibly improve the accuracy of FFR_{CT} .

The current flow boundary conditions are derived using population-based flow estimations which require geometrical measurements, such as myocardial mass or coronary vessel diameters, as input. Although these flow boundary condition have proven to provide high diagnostic value (Taylor et al., 2013), an improvement could be achieved by utilizing advection diffusion flow estimation (ADFE) to estimate patient specific coronary blood flow based on the contrast gradient found in CCTA images (Bakker et al., 2022; Bakker et al., 2021). The accuracy of the ADFE concept was proven in Chapter 4, however the data set used did not included imaging effects which affect the measured contrast intensity. These effects are mostly caused from blurring the image which blooms the contrast intensity outside of the vessel causing a decrease in measured contrast intensity. This will subsequently cause a significant decrease in performance for ADFE if not corrected.

In this Chapter, a first attempt of correcting ADFE for imaging effects observed on the CCTA image is proposed. This image correction function for ADFE will be derived and verified on synthetic data. As actual virtual computed tomography (vCT) is quite complex and our current goal is not quantifying every CT effect, we have chosen a simplified workflow for mimicking CCTA intensities from our patient specific spectral element method (SEM) results shown in Chapter 4. On this data set transluminal attenuation flow encoding (TAFE) flow was also computed and compared with ADFE to examine if the improvement in accuracy of ADFE over TAFE, showed in Chapters 3 and 4, is still present on this vCT data set.

5.2 Methods

In this section, we propose a vCT method for increasing the agreement between the concentration extracted from our software phantom data and the actual CCTA image. For our vCT method described below we propose a simple method that only mimics the total measurable effects caused by the imaging modality on the measured contrast intensity. Secondly, a CT correction function is proposed, which will be added to ADFE to ensure that the semi-analytical solution embedded in it can properly describe the blurred concentration data.

5.2.1 Virtual computed tomography

vCT methods create CT images based on numerical data. This enables the optimization of scanning protocols but can also be used for verifying image based methods such as ADFE. When creating vCT images, projections of the X-ray attenuation are computed by tracking the rays through the numerical mesh and mimic physics-based phenomenon affecting the measured attenuation (Abadi et al., 2018). For reducing complexity of this method, we will only model the two most significant imaging effects related to ADFE, namely blur and noise. Blur can be modeled by convolving your original image with the scanner specific point spread function (PSF). The PSF of CT has a complex shape that differs in all three directions and even changes shape based on image location (Schwarzband & Kiryati, 2005). Experimental measurements of CT PSF have shown that the PSF could be modeled with a Gaussian shape (Wang et al., 1998). Schwarzband and Kiryati (2005) opted against this claim stating that the apparent Gaussian PSF was caused by either an averaging effect on large structures or pure coincidence as PSF is location dependent. We still have chosen to model blur using a Gaussian PSF as there is an apparent resemblance between the actual and measured PSF.

CT noise measurements done on phantoms have shown a complex noise distribution, however this distribution converges to a Gaussian one for high intensities (Vegas-Sánchez-Ferrero et al., 2017). Since the typical contrast intensities are in that high range we also use a Gaussian distribution for modeling noise.

For setting the standard deviation σ for both noise and blur we utilized local CCTA image measurements. For the noise σ , we use the contrast intensities found in the aorta as the cross-sectional averaged value should be roughly constant. this resulted in an average σ of around 35 HU. For the PSF σ , we can use the sharp boundary found on the edge of the lung. This sharp

transition from high to low attenuation is smoothed out because of the blur and the length going from air (lung) to tissue is roughly 6σ . Measuring at multiple location resulted in an average σ of approximately 0.6 mm. Computing the blurred values can be done by discrete convolution of the concentration field with a Gaussian kernel. In this research, we found a $11 \times 11 \times 11$ kernel with equidistant placed points ranging from -3σ to 3σ to be sufficient enough to reach convergence of the blurred concentration. The interpolation of the concentration on each corresponding kernel point is done by using the interpolation functionality of the SEM solver and setting the value to zero if the point resides outside the mesh. For simulating noise random generated values based on the Gaussian noise distribution is added to each mesh point.

5.2.2 Computed tomography correction function

The cross-sectional averaged image intensity measured is not linearly correlated to the actual cross-sectional averaged contrast concentration \bar{C} due to the imaging effects described above. A correction is therefore needed in order for ADFE to compute flow from this blurred data. This correction function β should specifically add the effects of blur to compute a blurred $\bar{C}_b = \beta \bar{C}$. For β , the assumption is made that compared to the width of the PSF the contrast concentration is constant in the axial direction z . This means that β can be calculated on each plane perpendicular to the centerline. We can then define β as

$$\beta(z) = \frac{\int_{A(z)} C(z) * G(\sigma) dA}{\int_{A(z)} C(z) dA}. \quad (5.2.1)$$

with A the area inside the vessel perpendicular to the centerline, C the concentration, G the 2D Gaussian kernel with a standard deviation of σ , $*$ the convolution operator. The convolution integral on this 2D plane is by definition not axi-symmetric and therefore can only be calculated with numerical convolution. However, an approximation can be derived for a constant concentration over the cross-section. An axi-symmetric simplification in describing the convolution in only local radial coordinate r can be made as follow:

$$C(z) * G(\sigma) \approx \int_0^{a(z)} \frac{1}{\sqrt{2\pi}\sigma} e^{-\frac{(r-y)^2}{2\sigma^2}} dy = \frac{\operatorname{erf}\left(\frac{a(z)}{\sqrt{2}\sigma}\right) - \operatorname{erf}\left(\frac{r-a(z)}{\sqrt{2}\sigma}\right)}{2}. \quad (5.2.2)$$

Note that this integral only is valid when the kernel is not overlapping at the center of the area and by increasing a/σ the relative contribution of this error decreases. Integrating this equation over the entire area using $dA = 2\pi r dr$,

we can simplify β for every a to:

$$\beta = \frac{\sqrt{2}\sigma}{a\sqrt{\pi}}(e^{-\frac{a^2}{2\sigma^2}} - 1) + \operatorname{erf}\left(\frac{a}{\sqrt{2}\sigma}\right). \quad (5.2.3)$$

We can also computationally compute β on a grid by numerical convolution and integration. A comparison between this and Equation 5.2.3 is shown in Figure 5.1. From this we can see that Equation 5.2.3 starts to deviate from the actual blur loss when $a/\sigma < 1.5$, which is caused by the asymmetrical convolution. When computing β on a coarse grid, the partial volume effect can be modelled, however when taking into account the exact geometry of the vessel the difference between it and using a refined enough image grid is roughly less than 1%. This means that partial volume effect when intensity adjacent to the wall and exact geometries are known, can be neglected. For real CCTA images, partial volume effect is therefore an error introduced by estimating the position of the wall and by averaging out the contrast and objects adjacent to the wall. This means that correcting partial volume effect is case depended and therefore no general correction can be modelled.

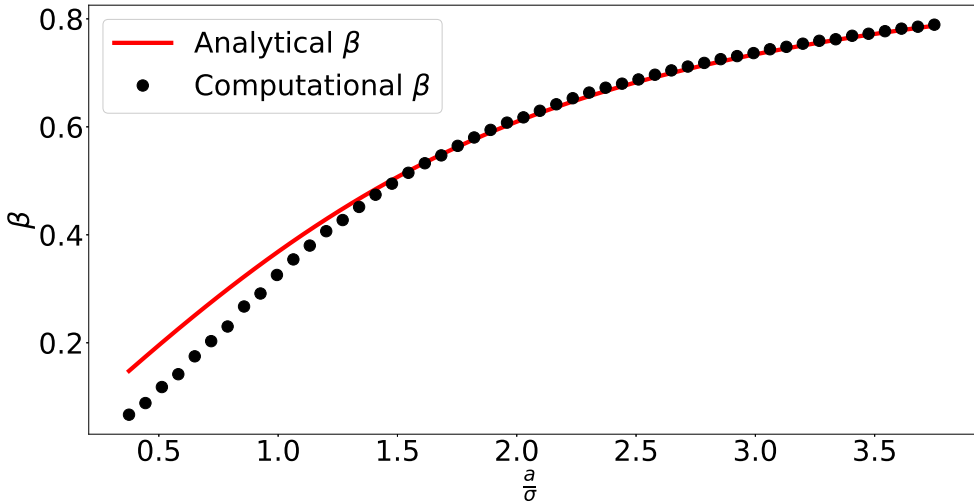


Figure 5.1: Comparison between analytical computed β using Equation 5.2.3 (red line) and computed on a grid (black dots). Note that the grid was refined enough for a converged solution.

For computing β for a radial varying contrast field, we utilize the semi-analytical solution from Chapter 3. This solution consist of a series of zeroth order Bessel function of which the first function is the cross-sectional averaged concentration \bar{C} . For the remaining functions the cross-sectional integral are

zero, however the convolution with the Gaussian kernel can cause this integral to be non-zero. This means that the blurred semi-analytical $\bar{C}_{a,b}$ is equal to:

$$\bar{C}_{a,b} = \beta \bar{C}_a + \sum_{i=1}^N C_i \int_A b_i * G(\sigma) dA, \quad (5.2.4)$$

with C_i , the i -th Bessel series coefficient and b_i the Bessel series function on A .

5.3 Results

5.3.1 CT correction straight vessel

For validating the vCT and CT correction function, we utilised straight tubular software phantoms on which the transport of contrast was simulated. A selection of three software phantoms with a radius of 0.5 mm, 1.0 mm and 2.0 mm were used in order to include all different sized vessels typically found in a coronary tree. For the vCT, blur described in Section 5.2.1 was added to each point of all three software phantoms. Afterwards $\bar{C}_{d,b}$ was calculated by the SEM solver. For comparison the semi-analytical $\bar{C}_{a,b}$, described by Equation 5.2.4, was also computed and compared in Figure 5.2. From this we can see a good agreement between $\bar{C}_{a,b}$ and $\bar{C}_{d,b}$. This means proper implementation was done on both blurring methods and the size of the Gaussian kernel in the vCT method was sufficient enough to accurately compute $\bar{C}_{d,b}$ for all typical radii found in a coronary tree.

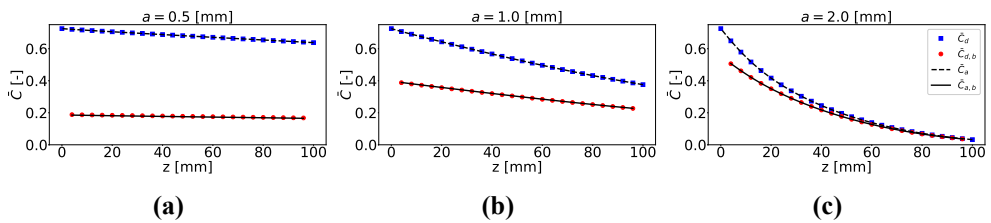


Figure 5.2: Comparisons between vCT and CT correction function for three straight vessels with different radii. The blue squares and red dots respectively represent \bar{C}_d and $\bar{C}_{d,b}$ computed by the SEM solver. The black lines represent the semi-analytical solution before (dashed line) and after blurring (solid line). Each column shows the results for $a = 0.5$ mm (a), $a = 1.0$ mm (b) and $a = 2.0$ mm (c). In all simulations $Q = 150$ mm³/s, $D = 0.01$ mm²/s and the AIF was set to case 1 of Chapter 4. Note that the first and last data point for the blurred numerical results were not included as these points have artificially loss concentration by blurring outside of the inlet or outlet.

5.3.2 CT correction vessel tree

In order for ADFE to accurately compute flow from CCTA images the measured intensity needs to be corrected for blur to linearly match the actual contrast concentration. For this the CT correction function to correct the semi analytical equation embedded in the ADFE method, shown in Equation 5.2.4, was verified in the above section for straight vessels. In chapter 4, a workflow for ADFE for tree-like geometries was derived and verified against patient specific software phantoms. On each vessel segment a L_2 -norm between the semi-analytical \bar{C}_a and \bar{C}_d extracted from the software phantom is minimized as function of Q . This means that the concentration profile is already calculated by the semi-analytical solution but not used in the ADFE workflow of Chapter 4. This ADFE workflow can therefore be used to compute flow from CCTA images by substituting \bar{C}_a with the blurred semi-analytical solution $\bar{C}_{a,b}$ and keeping all other steps the same. An example showing the ADFE fit on \bar{C}_d , $\bar{C}_{d,b}$ and for reference the actual measured CCTA intensity from the segmentation the numerical model was based on are shown in Figure 5.3. Verifying this

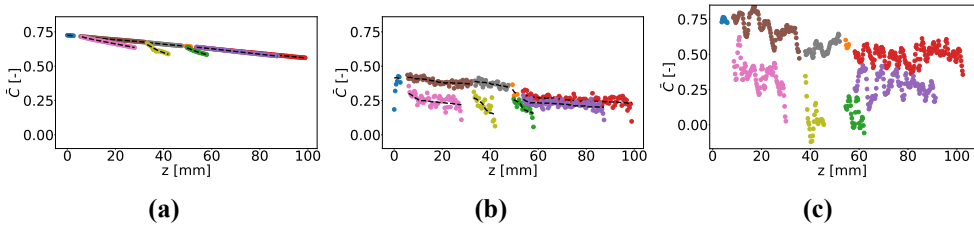


Figure 5.3: Figures show \bar{C} over the path length z examples based on the RCA of case 1 and extracted from the software phantom (a), the software phantom with the vCT added (b) and the original CCTA on which the software phantom is based on (c). Each color represents \bar{C}_d of a vessel segment and for Figures a and b the dashed black line represents the fitted semi-analytical solution \bar{C}_a after performing ADFE. Note that the original CCTA image is acquired later in time compared to the software phantom which explains the higher concentration at the inlet.

CCTA ADFE workflow was done on the same in-silico patient data sets from chapter 4. vCT, described in Section 5.2.1, was again used to add blur and noise to each point of each software phantom. Next, ADFE and TAFE flow was computed on the original concentration data, blurred concentration data and blurred concentration data with added noise. The comparison between the computed flow Q_m of either ADFE or TAFE and Q_d , the input flow used to simulate C are shown in Figures 5.4 and 5.5. From these results it can be seen that ADFE decreases in accuracy when applied to blurred concentration data and a small decrease in robustness with the additional noise added to the data. Overall ADFE starts to underestimate the amount of flow seen from the aver-

age error dropping from 1% to -16%. The confidence intervals of the relative error also significantly worsen for the vCT ADFE results with the increased standard deviation in relative error from 8% to 40% for the blurred concentration and further to 50% with the added noise. Although this is mostly due to the high relative error in vessel segments with a low amount of flow, which by examining Figure 3.4, can be seen that the absolute error is comparable with the higher flow vessel segments. The TAFE results on the blurred data also shows an overall reduced amount of flow being computed as the average relative error is reduced from -20% to -34%. The error distribution is less affected by blurring the signal with even a slight improvement in the tightness of the confidence interval which dropped from 66% to 62%. TAFE is also hardly affected by the added noise as it produced almost identical results. Finally, it can be concluded that although ADFE is relatively impacted more by the effects of blur and noise, it still offers a significant improvement over TAFE. This is demonstrated by the tighter confidence interval and the higher correlation coefficient of ADFE compared to TAFE, which was made possible with the CT correction function implemented in ADFE.

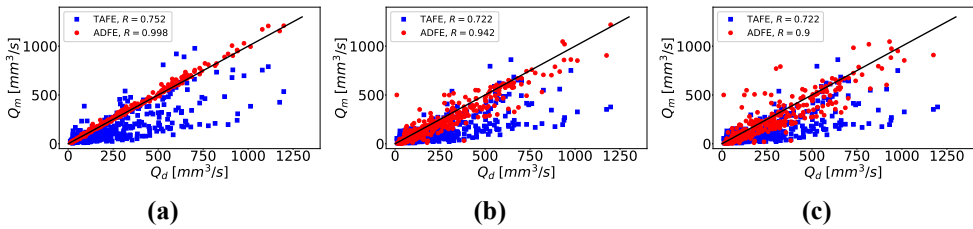


Figure 5.4: Comparison between ADFE and TAFE on software phantoms from Chapter 4 containing no effects (a), blur (b) and blur with additional noise (c) on the original simulated contrast data. Each figure shows a correlation plot between Q_d and Q_m for ADFE (red dots) and TAFE (blue squares). The correlation coefficient R for each method is shown in each respective plot.

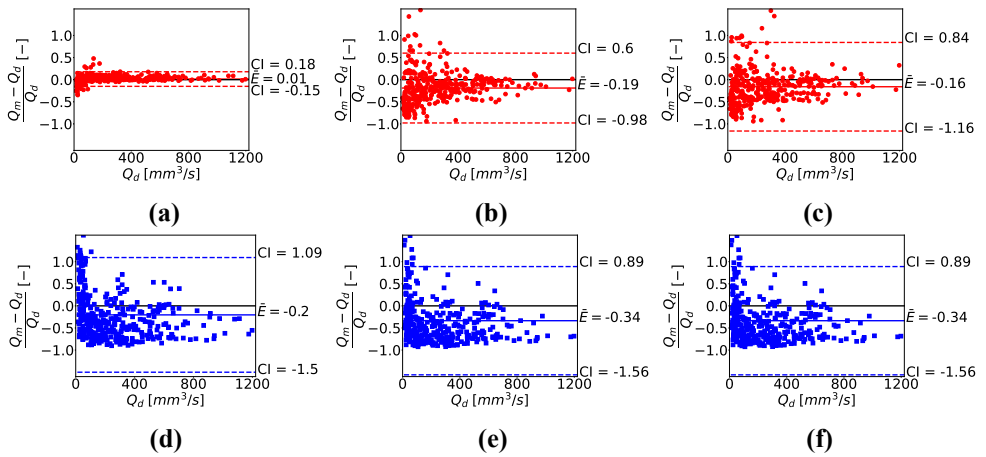


Figure 5.5: Relative difference plots for ADFE (red dots) on software phantoms from Chapter 4 containing no effects (a), blur (b) and blur with additional noise (v) and similar for TAFE (blue squares) with no effects (d), blur (e) and blur with additional noise (f). The relative error is calculated as $\frac{Q_d - Q_m}{Q_d}$ and for each figure the mean difference (black line) and 95% confidence interval (dotted lines) are shown.

5.4 Discussion

In this study, we developed and added a CT correction function to ADFE in order to make ADFE more suitable to be used on CCTA images. This function computes the relative intensity drop after the CCTA blur blooms intensity outside of the vessel. Adding this function enables the semi-analytical solution used in ADFE to better match the blurred concentration data during the optimization steps. The updated ADFE workflow was then verified on vCT software phantoms based on the patient specific software phantoms from Chapter 4. Overall the accuracy of ADFE became significant worse with relative error decreasing from 1% to -16%, however ADFE still showed a improvement compared to TAFE.

The vCT method transformed the patient specific software phantom data set of Chapter 4 to be more in agreement with actual CCTA data. This enabled us to verify ADFE on more CCTA-like data by doing the one to one comparison of ADFE flow with the ground truth flow, similar to the verification steps done in Chapters 3 and 4. This vCT method is therefore a useful tool as we can now more easily identify components inside the ADFE method that need improvement. However by comparing the vCT concentration with the intensity found in the actual CCTA image, it is clear that some aspects are missing during the computation of the virtual data. Firstly the CCTA image intensity appears to be more noisier compared to our virtual intensity. This could be caused by the possible higher noise reduction when averaging out the noise added to each mesh point during the cross-sectional averaged concentration computations from the SEM solver compared to doing the same from the CCTA image by averaging out the lesser amount of voxels. Additionally noise on the CCTA image could also be originated from other sources, such as errors in the segmentation of the coronary arteries or partial volume effect. Secondly, the simulations to mimic the transport of contrast are simplified compared to the actual situation. The pulsatility in the contrast transport caused by the beating heart adds oscillations to the measured signal but also adds more mixing of the contrast concentration. This mixing alters the concentration profile which impacts the blur loss computed by the vCT. Similarly, the assumed flat concentration profile at the inlet can also significantly differ from the actual CCTA concentration profile, which again impacts the concentration profile across the entire tree and thus the blur loss computed by the vCT.

Partial volume effect can also be significantly affecting ADFE but this is difficult to model as it is the general effect of being unable to determine

the composition within a voxel. This means that for vCT on synthetic data with a constant background the partial volume effect can easily be reversed as we know the exact composition of objects within each voxel. However, this is not the case for clinical data as there can be a wide range of different structures next to the coronary arteries. This means that the effects of partial volume effects are case depended and can not be modelled for a large patient population.

At the current state of the vCT, there is already an underestimation of the computed ADFE flow. Our hypothesis is that there is a significant error in the concentration profile, which is used in the CT correction function. During the optimization of ADFE the flow is then artificially lowered to still match $\bar{C}_{a,b}$ and $\bar{C}_{d,b}$. Currently, we suspect two phenomenon that are the main reason for this concentration profile error. Firstly, the semi-analytical solution embedded in ADFE uses the assumption that the velocity field has a parabolic shape. In Chapter 4 this assumption was verified to be valid, but for some vessel segments the flow was high enough that the velocity was not viscous dominated anymore or i.e. the velocity profile start to transition from a parabolic shaped profile to a flat profile. This resulted for some coronary trees in a small overestimation of the computed ADFE flow (see Chapter 4). However, when correcting for blur this error in the assumed velocity profile becomes more apparent as this also impacts the computed concentration profile, which is inputted to the CT correction function. Secondly, after each bifurcation the concentration profile of the input vessel is split between the two output vessel segments which alters the concentration profile when transitioning through a bifurcation. In ADFE the input concentration profile is currently copied to the two output vessel segments which neglects the effects of the bifurcations on the concentration profile. This approximation was good enough for achieving the excellent ADFE accuracy on the original data set, however again the error in the computed concentration profile adds to the error in the CT correction function. Overall, it is crucial to both research in correcting the velocity profile used in the semi-analytical solution and adding a transformation function for calculating the resulting concentration profile after a bifurcation. If done accurately, we foresee that it will reverse the current underestimation of computed flow.

5.5 Conclusion

Building on top of the accuracy of ADFE for coronary trees showed in Chapter 4, a first attempt towards making ADFE suitable for CCTA images was

taken. A simple vCT was used to transform patient specific software phantoms to more CCTA-like data. This enabled the investigation and first verification of ADFE with a new build-in CT correction of which the results are already promising. By improving the semi-analytical solution described above, ADFE has the potential to provide an accurate estimation of coronary blood flow based on the CCTA image. This reduces the possibility of needing additional correction on ADFE when transitioning from these software phantoms towards actual CCTA image.

References

- Abadi, E., Harrawood, B., Sharma, S., Kapadia, A., Segars, W. P., & Samei, E. (2018). Dukesim: A realistic, rapid, and scanner-specific simulation framework in computed tomography. *IEEE transactions on medical imaging*, *38*(6). <https://doi.org/10.1109/TMI.2018.2886530>
- Bakker, L. M. M. L., Xiao, N., Lynch, S., van de Ven, A. A. F., Updegrove, A., Schaap, M., Buls, N., de Mey, J., van de Vosse, F. N., & Taylor, C. A. (2022). Pre-clinical validation of the advection diffusion flow estimation method using computational patient specific coronary tree phantoms [Under review]. *International Journal for Numerical Methods in Biomedical Engineering*.
- Bakker, L. M. M. L., Xiao, N., van de Ven, A. A. F., Schaap, M., van de Vosse, F. N., & Taylor, C. A. (2021). Image-based blood flow estimation using a semi-analytical solution to the advection-diffusion equation in cylindrical domains. *Journal of Fluid Mechanics*, *924*, A18. <https://doi.org/10.1017/jfm.2021.596>
- Schwarzband, G., & Kiryati, N. (2005). The point spread function of spiral ct. *Physics in medicine and biology*, *50*, 5307–22. <https://doi.org/10.1088/0031-9155/50/22/007>
- Taylor, C. A., Fonte, T. A., & Min, J. K. (2013). Computational fluid dynamics applied to cardiac computed tomography for noninvasive quantification of fractional flow reserve: Scientific basis. *J Am Coll Cardiol.*, *61*(22), 2233–2241. <https://doi.org/10.1016/j.jacc.2012.11.083>
- Vegas-Sánchez-Ferrero, G., Ledesma-Carbayo, M. J., Washko, G. R., & San José Estépar, R. (2017). Statistical characterization of noise for spatial standardization of ct scans: Enabling comparison with multiple kernels and doses. *Medical Image Analysis*, *40*, 44–59. <https://doi.org/https://doi.org/10.1016/j.media.2017.06.001>
- Wang, G., Vannier, M., Skinner, M. W., Cavalcanti, M., & Harding, G. W. (1998). Spiral ct image deblurring for cochlear implantation. *IEEE transactions on medical imaging*, *17*, 251–62. <https://doi.org/10.1109/42.700737>

6.1 Current overview

Coronary computed tomography angiography (CCTA) is the leading imaging modality for assessing coronary artery disease (CAD). The injection of a contrast agent during the CCTA scan highlights the coronary lumen and the presence of CAD on the CCTA image. Assessing the severity of CAD is done by the fractional flow reserve (FFR), i.e. the ratio between the pressure distal to the stenosis and aortic pressure (Pijls et al., 2010; Tonino et al., 2009). FFR is measured using a pressure wire that is surgically positioned, whereas FFR_{CT} circumvents the use of a invasive procedure by calculating FFR using computational models. The accuracy of these models heavily rely on the correct segmentation of the coronary arteries and imposition of coronary blood flow (CBF) at the in- and outlets. Current methods for determining the boundary conditions consist on power laws which rely on anatomical information such as myocardial mass. Although these models result in a high diagnostic accuracy of FFR_{CT} (Taylor et al., 2013), an improvement could be achieved in inferring the flow information embedded inside the contrast distribution. A first clinical attempt in extracting diagnostic information from the contrast opacity is called transluminal attenuation gradient (TAG) and is defined as the linear contrast intensity gradient across the path length (Steigner et al., 2015). Transluminal attenuation flow encoding (TAFE) was later developed to compute CBF from TAG. This was done by linking the arterial input function (AIF) to TAG using the 1D advection equation (Eslami et al., 2015). This

addition of the AIF to TAG in TAFE resolves a significant disadvantage of TAG as it is dependent on the AIF gradient of time. After studying the accuracy of TAFE, the creators included two correction coefficients for linearly increasing the computed TAFE flow (Eslami et al., 2022). The first term involves solving the non-discrepancy between the measured intensity and actual contrast concentration. This is caused by imaging effects i.e. blur and partial volume, which are the result of the radiation and reconstruction protocols used in CCTA. The second term involves the invalid assumption that radial advection and diffusion can be neglected. For improving TAFE we included radial advection and diffusion in our new method called advection diffusion flow extraction (ADFE). For verifying ADFE and comparing against TAFE a controlled setting is necessary on which no imaging effects are present. This was done by utilizing software phantoms on which the transport of contrast was simulated by use of our in house build spectral element method (SEM) solver.

Our SEM solver, explained in Chapter 2, utilizes higher order elements together with optimal integration to solve conservation equations representing a physical system. For this it needs less points and elements to achieve a preset accuracy compared to traditional finite element method (FEM). The higher order polynomials used are also able to describe "sharp" boundaries that are often situations which require stabilization methods using FEM. These stabilization methods can significantly affect the solution in an unpredictable way which is not desirable for verification studies. The smaller number of points also reduces the computational power needed as all simulations used in this thesis were computed on a single laptop.

ADFE and often other inverse optimization problems rely on fitting a model on measured data of which the computed parameters serve a purpose. This means that not only a good fit needs to be found, i.e. good agreement between model and measured data, but the found parameters also should be the true values. Often the amount of parameters needed to be fitted offer a too high number of degrees of freedom. The result is then often a wide range of possible parameters yielding the same amount of agreement between model and measured data. Restricting the number of fitted parameters and the interaction between them, we find an increase of uniqueness of the found fit. In ADFE this was achieved by utilizing a semi-analytical solution of the 2D axi-symmetric advection diffusion equation that can describe the contrast transport for vessels with a slowly varying radius. This solution provides a clear relationship between advection and diffusion and requires low computational effort. A verification study, shown in Chapter 3, was done on simple 2D axi-symmetric vessels to demonstrate the accuracy of

the semi-analytical solution and benchmark ADFE against TAFE. Excellent agreement could be achieved between the semi-analytical solution and simulated 2D axi-symmetric data. This also ensured us that ADFE predicts the imposed flow and gains a great improvement in accuracy compared to TAFE. This study showed the importance of including radial velocity and diffusion when modeling contrast transport. Similar results could also be achieved when using the SEM solver instead of the semi-analytical solution. However, the computation time for computational models is still substantially larger compared to the semi-analytical solution. This difference becomes larger when scaling up to coronary trees as the computation time for one ADFE optimization iteration can take hours for large cases. This would make ADFE not practical for clinical usage.

For verifying ADFE for coronary trees a second verification study is necessary as coronary trees are, when compared to the 2D axi-symmetric vessels, curved, have a non constant radius and also contain bifurcations. In Chapter 4 we derived a new ADFE workflow that combines all vessel segments and computes CBF on each segment. The verification was again, to exclude imaging effects, performed on software phantoms. These software phantoms are patient specific geometries extracted from CCTA images on which contrast transport was simulated by our SEM solver. The results show excellent agreement between imposed and ADFE flow. The new two steps optimization process ensured a robust fitting of the semi-analytical solution and great accuracy. This updated workflow for coronary trees resulted in a negligible loss of accuracy when scaling up from 2D axi-symmetric vessels to complex coronary trees and again, compared to TAFE, ADFE showed great improvement in accuracy of computed flow.

The verification study for coronary trees shows that ADFE does not need corrections for wrongly simplifying our contrast transport model. However, the intensity measured from the CCTA contains imaging effects such as blur and noise. Especially blur lowers the measured cross-sectional averaged intensity of the contrast agent by blooming contrast intensity outside of the vessel. In Chapter 5 we showed that the amount of bloom not only depends on the size of the vessel compared to the point spread function (PSF) but also the radial variation of the concentration field. The embedded semi-analytical solution inside ADFE computes the concentration in both axial and radial direction. These results are used as input to a new CT correction function that computes the relative intensity drop caused by the blur for each cross-section. By substituting in this blurred semi-analytical concentration calculated by the CT correction function, ADFE is able to compute flow from blurred concen-

tration data. This blurred ADFE method was verified on the same software phantoms used in Chapter 4 whose contrast data has been transformed to add the CCTA image effects. This transformation was performed using a simple virtual CT (vCT) simulator that adds the effects of blur and noise to the simulated concentration data. The verification results, obtained in Chapter 5, show a decrease in accuracy of ADFE compared to the original data, despite the added CT correction function. TAFE was less impacted by the added CCTA imaging effects, however ADFE still showed a big improvement over TAFE.

6.2 Future work

Based on the insights at the end of Chapter 5, future ADFE related studies should investigate possible improvements of the concentration profile computed by the semi-analytical function. A high dependency was found between the accuracy of ADFE and the CT correction function which requires these concentration profiles as input.

Our first suggestion is improving the assumed parabolic velocity profile in the semi-analytical solution. At the start of the coronary circulation the flow could be too high to accept a parabolic velocity profile as the viscous forces are not dominated enough. This already resulted in an overestimation of ADFE flow in Chapter 4 but also affected the computed concentration profile which could explain the underestimation in ADFE flow found in Chapter 5. In Chapter 3 details on how to adapt this velocity profile are provided. The second suggestion is related to the oversimplified prediction of the concentration profile after a bifurcation. Currently, the profile at the end of the input vessel segment is copied to the two output vessel segments. In Chapter 4 this approach resulted in an imperceptible decrease in accuracy. However, this concentration profile error is propagated over the entire vessel segment which again can be a source of the observed underestimation in computed ADFE flow. Improvements to the assumed velocity profile could be achieved by utilizing a simplified solution of the Navier Stokes equation. These solutions are often reduced in order to speed up the computation at the expense of the extent how detailed the results are. As we are only interested in an approximation of the velocity profile over the axial length a highly reduced order model could be functional, which does not add much in the total computational time of ADFE.

Secondly, a transformation function for approximating the changes of the concentration profile being transported through a bifurcation, can improve the computed ADFE flow as this results in a better agreement between the blurred

semi-analytical solution and measured intensity. The bifurcation is a complex 3D geometry which splits the concentration profile that is rearranged in each output vessel segment. The resulting concentration profiles depend on many factors such as the angles between the three vessel segments, radii of the connecting vessel segments or the summed effect of multiple bifurcations in a row. This implies that modeling this transformation is difficult to do for highly reduced-order models and only possible using full 3D simulations. A hybrid model that connects the vessel segments based on the axi-symmetric solution with full 3D bifurcations calculated with the SEM solver would be good first starting point as this combines low computational effort in the vessel segments and accurate transformation of the concentration profiles between vessel segments.

Besides the proposed improvements described above, which will hopefully aid in improving the ADFE results of the in-silico data set used in Chapter 5, there are still some physical phenomenon not included in these software phantoms which are present in actual CCTA intensity data. First preliminary ADFE results on actual CCTA have shown a discrepancy in the intensity assumed by the ADFE method and measured at the inlet of the coronary circulation. This discrepancy can cause unpredictable outliers in the computed ADFE flow as during the ADFE optimization the flow will be adjusted to overcome it. We believe that the origin of this lies in the pulsatility of the contrast transport. Firstly the actual AIF contains pulsatile intensity variation which when smoothed follow the used description in this thesis. These variation are smoothed out by diffusion the further away from the aortic valve, however this could not be enough at the start of the coronary circulation. Secondly, in ADFE we only model the average velocity contrast transport, however the measured contrast intensity pulsates around this average caused by the time varying velocity field. Both effects could contribute to the observed discrepancy in the intensity between ADFE and measured intensity at the inlet of the coronary circulation and therefore more research is need to quantify and correct this.

Another not included phenomenon is verifying the ADFE method on coronary trees containing CAD. In Chapter 4 and 5 vessel segments were highlighted which deviated from the assumed parabolic velocity field. The narrowing of the vessel diameter due to a stenosis is an extreme situation where this also occurs. Additionally, the concentration profile is piled together inside of the stenosis and a reorganization occurs distal to the stenosis. With the current implementation of ADFE, we would advice to treat a significant stenosis similar to a bifurcation and fit the semi-analytical solution proximal and dis-

tal to the stenosis, excluding the diseased area from the ADFE optimization. More research is needed in when a stenosis becomes significant enough for excluding it and how to perform the ADFE fit distal to the stenosis.

Clinically validating ADFE could be done by measuring blood flow using intracoronary thermodilution (Candrea et al., 2021; Gallinoro et al., 2021). During thermodilution a cold saline solution is injected inside the coronary vessel together with monitoring the blood temperature. The cold solution lowers the blood temperature and when the injection is stopped the measured blood temperature will return to the starting temperature. The pump rate and relative temperature difference before and after injection are related to the blood flow through this vessel. Together with these blood flow measurements at multiple location inside of the coronary tree, a CCTA image together with AIF makes it possible to compare between the measured and ADFE derived flow. This comparison could be performed similarly to the comparisons performed in Chapters 4 and 5.

Finally, based on the software phantoms used in this thesis, a lot of insight has been gained in the contrast distribution generally found in the CCTA image. Specifically each vessel segment contains a concentration boundary layer in which the contrast concentration increases from almost zero at the wall up to an almost constant concentration at the center. The thickness of this boundary layer does not only depend on physical parameters such as the Peclet number but also on the timing of the AIF. This timing of the AIF is especially important as the thickness increases with increasing changes in intensity of the AIF over the time. It will reach a minimum on top of the AIF plateau just before the contrast concentration will start to decrease again. Current segmentation methods rely on a constant intensity over the cross section and thus do not correct for the underestimation of the radius caused by this boundary layer. This means that for segmenting the coronary tree it is important to track the AIF in order to ensure that the optimal condition at the AIF plateau is reached. For this, it is crucial to obtain the AIF data set to at least check this. An even better improvement can be reached when utilizing the concentration profile of the semi-analytical solution found in the ADFE method. This concentration profile will provide an improved approximation of the actual profile which will aid in properly segmenting the coronary tree.

References

Candrea, A., Gallinoro, E., van 't Veer, M., Sonck, J., Collet, C., Di Gioia, G., Kodeboina, M., Mizukami, T., Nagumo, S., Keulards, D., Fournier, S., Pijls, N. H.,

- & De Bruyne, B. (2021). Basics of coronary thermodilution. *JACC: Cardiovascular Interventions*, *14*(6), 595–605. <https://doi.org/https://doi.org/10.1016/j.jcin.2020.12.037>
- Eslami, P., Seo, J. H., Rahsepar, A. A., Richard, A. G., Lardo, A. C., & Mittal, R. (2015). Computational study of computed tomography contrast gradients in models of stenosed coronary arteries. *J Biomech Eng.*, *137*(9). <https://doi.org/10.1115/1.4030891>
- Eslami, P., Seo, J. H., Rahsepar, A. A., Shafique, A., Rollison, S. F., Lardo, A. C., Mittal, R., & Chen, M. Y. (2022). A noninvasive assessment of flow based on contrast dispersion in computed tomography angiography: A computational and experimental phantom study. *J Biomech Eng.*, *144*(9). <https://doi.org/10.1115/1.4053997>
- Gallinoro, E., Candreva, A., Colaiori, I., Kodeboina, M., Fournier, S., Nelis, O., Di Gioia, G., Sonck, J., van 't Veer, M., Pijls, N., Collet, C., & de Bruyne, B. (2021). Thermodilution-derived volumetric resting coronary blood flow measurement in humans. *EuroIntervention*, *17*(8), E672–E679. <https://doi.org/10.4244/EIJ-D-20-01092>
- Pijls, N. H., Fearon, W. F., Tonino, P. A., Siebert, U., Ikeno, F., Bornschein, B., van't Veer, M., Klauss, V., Manoharan, G., Engstrøm, T., Oldroyd, K. G., Ver Lee, P. N., MacCarthy, P. A., & De Bruyne, B. (2010). Fractional flow reserve versus angiography for guiding percutaneous coronary intervention in patients with multivessel coronary artery disease: 2-year follow-up of the fame (fractional flow reserve versus angiography for multivessel evaluation) study. *J Am Coll Cardiol.*, *56*(3), 177–184. <https://doi.org/10.1016/j.jacc.2010.04.012>
- Steigner, M. L., Mitsouras, D., Whitmore, A. G., Otero, H. J., Wang, C., Buckley, O., Levit, N. A., Hussain, A. Z., Cai, T., Mather, R. T., Smedby, O., DiCarli, M. F., & Rybicki, F. J. (2015). Iodinated contrast opacification gradients in normal coronary arteries imaged with prospectively ecg-gated single heart beat 320-detector row computed tomographys. *Circ Imaging*, *137*(9), 179–186. <https://doi.org/10.1161/CIRCIMAGING.109.854307>
- Taylor, C. A., Fonte, T. A., & Min, J. K. (2013). Computational fluid dynamics applied to cardiac computed tomography for noninvasive quantification of fractional flow reserve: Scientific basis. *J Am Coll Cardiol.*, *61*(22), 2233–2241. <https://doi.org/10.1016/j.jacc.2012.11.083>
- Tonino, P. A., De Bruyne, B., Pijls, N. H., Siebert, U., Ikeno, F., van' t Veer, M., Klauss, V., Manoharan, G., Engstrøm, T., Oldroyd, K. G., Ver Lee, P. N., MacCarthy, P. A., Fearon, W. F., & (2009), F. S. I. (2009). Fractional flow reserve versus angiography for guiding percutaneous coronary intervention.

The New England journal of medicine, 360(3), 213–224. <https://doi.org/10.1056/NEJMoa0807611>

Samenvatting

Bij coronaire computer tomografie angiografie (CCTA) wordt een intraveneus contrastmiddel op basis van jodium in de bloedbaan geïnjecteerd om de grenzen van de kransslagaders zichtbaar te maken. Hiermee kunnen de geometrische kenmerken van obstructieve atherosclerotische plaques, d.w.z. stenosen, anatomisch worden beoordeeld. Dit kan worden gebruikt om de ernst van een stenose vast te stellen en helpt bij het nemen van beslissingen over klinische interventie. Deze beoordeling geeft echter geen informatie over hemodynamische kenmerken zoals bloedstroom of bloeddruk verlies over de stenose, die betere variabelen zijn om beslissingen op te baseren.

De afgelopen jaren is de fractional flow reserve (FFR) gebruikt bij de klinische besluitvorming over de behandeling van coronaire hartziekten. FFR wordt gedefinieerd als de verhouding tussen de druk distaal van de stenose en de referentie druk van de aorta. Voor het meten van de FFR is een door fluoroscopie geleide invasieve katheterisatie en vervolgens het verder inbrengen van een drukdraad op een plaats in het bloedvat distaal van de stenose nodig. Dezelfde metriek kan echter ook worden verkregen met Computational Fluid Dynamics (CFD) modellen. Deze niet-invasieve CFD modellen worden gecreëerd door een numerieke mesh van de coronaire circulatie uit de CCTA te segmenteren en samen met randvoorwaarden, gebaseerd op schalingswetten die gebruik maken van patiënt specifieke geometrische eigenschappen. Hoewel gebleken is dat deze CFD-modellen een goede diagnostische waarde bieden, zou een verbetering kunnen worden bereikt door de hemodynamische en geometrische informatie af te leiden die verweven ligt in de contrast intensiteit van het CCTA beeld.

Bij de ingang van de coronaire circulatie (aorta) kan een stijging en daling

van de intraveneuze contrast concentratie in de tijd indirect worden gemeten via periodieke beeldvorming. Deze stijging en daling beschrijven de arteriële input functie (AIF). Het contrastmiddel wordt vervolgens door de coronaire bloedstroom (CBS) door de coronairen getransporteerd. De combinatie van AIF, CBS en coronaire geometrie resulteert in een contrastmiddel verdeling die zichtbaar is op het CCTA beeld. Deze verdeling wordt beschreven door de advection diffusie vergelijking. Door deze vergelijking op te lossen wordt een direct verband tussen al deze parameters verkregen. Hierdoor kan het inverse probleem van het extraheren van CBS op basis van de gemeten contrast intensiteit worden opgelost. Bestaande methoden hebben wisselend succes, wat wordt veroorzaakt door een te eenvoudige oplossing van de advection diffusie vergelijking en het feit dat de intensiteit die wordt gemeten op het CCTA beeld niet altijd goed gecorreleerd is met de werkelijke concentratie. In dit proefschrift stellen wij een verbeterde methode voor om CBS te bepalen, genaamd advection diffusion flow estimation (ADFE), door de oplossing van de advection diffusie vergelijking te verbeteren.

Om deze nieuwe oplossingsmethode te verifiëren hebben wij echter gegevens nodig die geen beeldvormende effecten bevatten. Klinische CCTA data sets zijn daarom niet geschikt voor verificatie, omdat de fout die wordt veroorzaakt door de gebruikte oplossing en de fouten die worden veroorzaakt door beeldvormende effecten onmogelijk te scheiden zijn. Daarom maken wij software fantomen die bestaan uit geometrieën waarop het transport van contrast wordt gesimuleerd. De berekeningen en het maken van deze simulaties worden uitgevoerd door onze spectrale elementen methode (SEM) oplosser die in Hoofdstuk 2 wordt beschreven. SEM gebruikt elementen van een hogere orde in combinatie met optimale integratie, waardoor situaties kunnen worden berekend zonder gebruik te maken van stabilisatie methoden die door de traditionele eindige elementen methode (EEM) wordt gebruikt. In de resultaten sectie tonen we de hogere convergentie snelheid van SEM in vergelijking met EEM en bespreken we de mogelijkheid om moeilijk te simuleren convectie gedomineerde situaties te berekenen. Alle genoemde software fantomen in dit proefschrift zijn berekend met deze SEM oplosser.

In Hoofdstuk 3 wordt de verbeterde oplossing van de advection diffusie vergelijking afgeleid en gevalideerd. Dit is een semi-analytische oplossing van de 2D axi-symmetrische advection diffusie vergelijking. Vervolgens is een verificatie uitgevoerd op 2D axi-symmetrische software fantomen door de overeenstemming tussen onze semi-analytische oplossing en de gesimuleerde concentratie te vergelijken. Deze oplossing vormt dan de basis voor onze nieuwe ADFE methode. ADFE is ook geverifieerd op de 2D

axi-symmetrische software fantoom dataset door de berekende volumestroom te vergelijken met de verwachte volumestroom. Ten slotte hebben wij ADFE getoetst aan de huidige gouden standaard, de transluminal attenuation flow encoding (TAFE), en aangetoond dat de voorspelde volumestroom van ADFE aanzienlijk beter is dan die van TAFE.

In Hoofdstuk 4 breiden wij ADFE uit om CBS te kunnen berekenen uit patiënt specifieke coronaire bomen. In vergelijking met eenvoudige axi-symmetrische geometrieën is een tweede optimalisatie stap in ADFE nodig om een robuuste en nauwkeurige berekening van CBS te waarborgen. De verificatie is opnieuw uitgevoerd op software fantomen die wij uit klinische CCTA data sets hebben gehaald en de resultaten tonen een uitstekende overeenkomst tussen de berekende en de verwachte volumestroom. Een belangrijke bijdrage hieraan is de extra optimalisatie stap in ADFE. Om er zeker van te zijn dat de verbetering van ADFE ten opzichte van TAFE ook geldt voor complexe boom geometrieën, vergelijken wij de twee methoden opnieuw en tonen aan dat deze nog steeds evident is.

Ten slotte wordt in Hoofdstuk 5 een CT correctie functie afgeleid om de effecten van onscherpte toe te voegen aan de in ADFE gebouwde semi-analytische oplossing. Hierdoor kan ADFE de bloedstroom berekenen op basis van de wazige contrast intensiteit in het CCTA beeld. Om ADFE met deze CT correctie functie te verifiëren is een eenvoudige virtuele CT methode gebruikt om de contrast data van de software fantomen van Hoofdstuk 4 te vervagen en vervolgens ruis er aan toe te voegen. Hoewel de nauwkeurigheid van ADFE op deze virtuele CT data set minder was dan die van de oorspronkelijke in Hoofdstuk 4 gebruikte data set, is het nog steeds een aanzienlijke verbetering ten opzichte van TAFE en bruikbaar voor klinische toepassingen. Samenvattend toont ADFE een groot potentieel om een nauwkeurige methode te worden voor het schatten van CBS uit CCTA beelden.

Curriculum Vitae

Luc Bakker was born on 22-10-1992 in Maastricht, the Netherlands. After finishing VWO in 2011 at Sint-Maartenscollege in Maastricht, he started his Bachelor in Biomedical engineering at Eindhoven University of Technology, where he obtained his degree in 2014. Afterwards, he started his Master degree in Biomedical engineering within the Cardiovascular Biomechanics group of prof. Frans van de Vosse. He graduated in 2016 with his thesis title: "Towards the development of a continuum perfusion model of the myocardium". His final assignment for graduating was an internship at HeartFlow in Redwood City, California, United States. The project contained the very start of the work presented in this dissertation and was also the reason it was extended into a PhD. His PhD therefor started right after returning from his internship in April of 2017 and the results are presented in this dissertation. Since 2022 he is employed at Bright-Society as a design engineer.